Developing Analytical Nonlinear Microscopy Techniques to Study Biomedical Systems

Andrew Thomas Francis

A dissertation

submitted in partial fulfillment of the

requirements for the degree of

Doctor of Philosophy

University of Washington

2020

Reading Committee:

Dan Fu, Chair

Joshua Vaughan

Jesse Zalatan

Program Authorized to Offer Degree:

Department of Chemistry

University of Washington

Abstract

Developing Analytical Nonlinear Microscopy Techniques to Study Biomedical Systems

Andrew Thomas Francis

Chair of the Supervisory Committee:
Dan Fu
Department of Chemistry

Analytical nonlinear microscopy (ANM) is an indispensable tool for quantitative imaging. Specifically, ANM has found significant utility for characterization of dynamic biomedical systems due to its high spatial and temporal resolution and intrinsic optical sectioning. Broadly defined as the interaction of more than one photon with a system of interest (e.g., molecular vibration), ANM describes numerous photophysical processes including, but not limited to, stimulated Raman scattering (SRS), transient absorption (TA), and two-photon excited fluorescence (TPEF). This dissertation describes the novel development and implementation of various ANM techniques to study both fundamental and clinical biomedical systems including red blood cell oxygen saturation and hemoglobin concentration, label-free pathology, and *in vivo* cerebral hemodynamics and cell architecture.

TABLE OF CONTENTS

LIST OF FIGURES

LIST OF TABLES

ACKNOWLEDGEMENTS

My studies and Ph.D. were made possible through the love and support of my parents, Tim and Amy, my brother, Zac, my aunt and uncle, Dorothy and Brett, my family, and my friends. I am grateful to have so many wonderful people in my life. I love you all deeply.

I would like to acknowledge the many teachers and professors who helped me discover a passion for science and inspired me to pursue a degree in chemistry. I would not have made it this far without dedicated, caring educators. I would like to express my deep gratitude to my Ph.D. advisor, Dr. Dan Fu, who has been a role model and inspiration during my time as a graduate student. His advice, guidance, and leadership have made me the scientist that I am today.

I owe a tremendous amount of gratitude to my peers and group mates who have braved the Ph.D. route alongside me and to the post-docs who put it all in perspective. From the laboratory to the brewery, I have gotten to know some exceptional scientists, and I greatly value the time we have spent together. I have no doubt that they all have promising careers ahead of them, and I am excited to see where they go.

I would like to acknowledge the collaborators who have taught me the value of interdisciplinary science. No one can know everything, and the best science comes from surrounding yourself with experts in their own fields. Specifically, I would like to thank Drs. Andy Shih, Melanie Shears, Shaun Murphy, Yongchao Su, and Gordana Juric-Sekur. I have learned volumes from being in the same room as these great scientists and doctors.

My research was made possible by the dedicated personnel at the Office of Animal Welfare. I would specifically like to thank Erika French and Kathy Andrich for their time and compassion. I would like to thank the University of Washington and the chemistry department for the opportunity and privilege to study at such an amazing institution. Here, I am surrounding by some of the most brilliant and friendly people I have ever known. If I had to choose again, I would not go anywhere else.

And finally, I would like to thank my friends. I am truly lucky to have made and kept so many kind and loving friends over the years. It is these friendships that have brought the most joy and meaning to my life. Short of writing another thesis, I cannot put into words what they all have done for me. I am and will always be grateful.

DEDICATION

To my parents, my brother, my family, and my friends

Chapter 1. INTRODUCTION

In the mid-1800s, Robert Bunsen and Gustav Kirchhoff reported the discovery of rubidium and cesium using flame emission spectroscopy, the earliest demonstration of spectroscopy in the field of analytical chemistry. Their simple instrument consisted of a Bunsen burner, a prism, and a pair of telescope lenses. Today, over 150 years after Bunsen and Kirchhoff's experiments, analytical spectroscopy has become an invaluable method for biology, chemistry, and medical science researchers. And while advancements in laser design have entirely revolutionized analytical spectroscopy since its inception, the same core questions still guide researchers today. What are the atomic or molecular constituents of a sample? How much of each constituent is present? Providing more precise answers to these questions is the impetus for designing increasingly sophisticated instrumentation. Analytical spectroscopy is refined and reshaped on a nearly daily basis as reflected in the vast number of annual publications. One avenue of intense research development is the translation of analytical spectroscopy to microscopy. In addition to identifying or quantifying the constituents of a sample, microscopy provides mapping of spatial distribution of those constituents. This capability has allowed researchers to investigate localized processes within heterogenous samples, such as electron transport in photovoltaic cells[1,2] or metabolism in cancer cells.[3–5] The latter example represents the application of analytical microscopy to the interdisciplinary field of biomedical microscopy.

The core goal of biomedical research is to understand disease states and pathologies in humans. As such, biomedical research can be broadly divided into two subfields: fundamental and clinical. The former seeks to understand the causes and mechanisms of disease states and pathology, while the latter primarily focuses on improving diagnosis and improving patient outcome. While fundamental biomedical research and clinical biomedical research have different

objectives, both find tremendous utility in microscopy. Fundamental biomedical research looks to understand more about life processes in both healthy and disease states. In fundamental biomedical research, many researchers employ model systems, such as cells grown in a Petri dish[6] or a tumor grown in a mouse,[7–9] to investigate specific aspects of a disease or pathology. These models serve a crucial role in helping researchers to control the vast variable space that would otherwise significantly convolute data interpretation and analysis. Here, microscopy provides a means to study the fine spatial dynamics of how a disease or pathology progresses and what intervention is necessary to fight it. Clinical biomedical research seeks to employ analytical spectroscopy and microscopy to improve diagnosis and help guide medical intervention. Here, researchers typically work with human tissues and must overcome the associated heterogeneity of such tissues. Clinical biomedical research is invaluable in developing cutting edge technologies for guiding medical intervention and ultimately improving prognosis and outcome.

This chapter will discuss 1. the principles of analytical spectroscopy and microscopy, 2. the applications, limitations, and challenges of biomedical microscopy, and 3. the future of biomedical microscopy.

1.1 Principles of Analytical Spectroscopy and Microscopy

Analytical spectroscopy, the quantitative interaction of light and matter, is a vastly diverse field that is typically defined by the region of the electromagnetic (EM) region employed. The imaging techniques described in Chapters 2-6 all employ near-IR wavelengths due to reasons discussed in Sections 1.1.2 and 1.2. Thus, only the visible and near-IR regions of the EM spectrum (~400-1200 nm) will be discussed in this dissertation. In this region, the interaction of light and matter largely falls into one of three categories: absorption, inelastic scattering (i.e., Raman scattering), or elastic scattering. The energy diagrams of these processes are provided in Figure 1.1. Both absorption

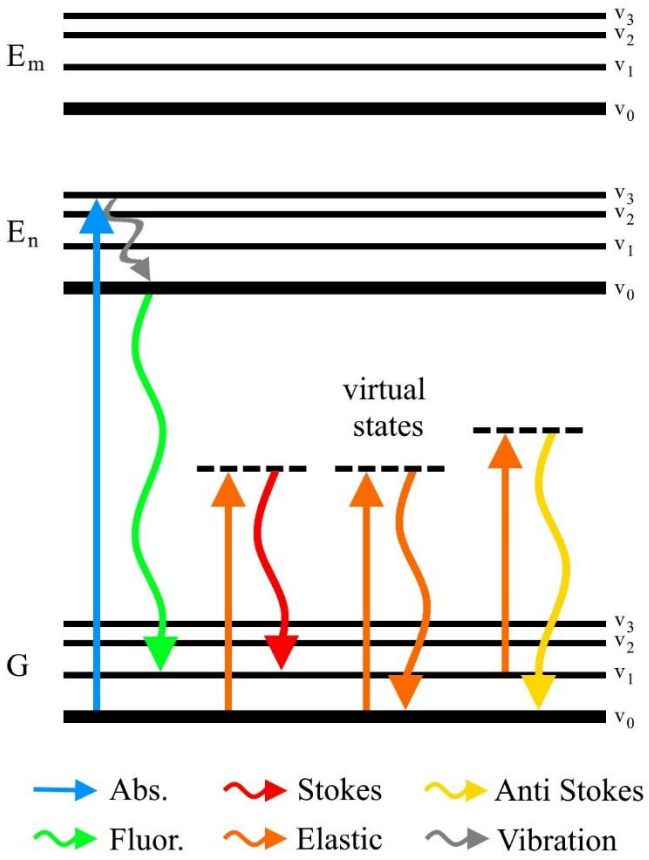

Figure 1.1 Energy level diagram for four analytical spectroscopy techniques: absorption, fluorescence, Raman scattering (Stokes and anti-Stokes), and elastic scattering.

spectroscopy and Raman scattering spectroscopy involve an energy transfer from a photon to a molecule.[10] During an absorption event a photon is completely absorbed by a molecule relating to the excitation of either an electronic excitation or vibrational excitation. In the case of an electronic excitation, the electron can proceed through various pathways to energetically relax back to ground states. The two processes shown in Figure 1.1 are nonradiative decay through vibration and radiative decay through fluorescence. In contrast, a Raman scattering event involves the partial transfer of energy between photon and molecule. Largely, the interaction involves a photon transferring a portion of its energy to vibrationally exciting a molecular bond. This interaction results in the emission of a lower energy photon relative to the incident photon. Both processes – absorption and Raman scattering – provide rich information regarding the energy levels of the molecule. Elastic scattering does not probe a molecule's energy levels. Rather, elastic scattering is sensitive to particle size, shape, and refractive index.

The absorption based and inelastic scattering based spectroscopy techniques mentioned above can be conducted as either linear or nonlinear spectroscopy. The difference between the

categories is the number of photons that interact with the molecule. In linear spectroscopy a single photon interacts with the sample. In nonlinear spectroscopy, multiple (2+) photons interact with the sample which presents numerous photophysical processes not achievable with linear spectroscopy. Nonlinear spectroscopy is also referred to as multiphoton spectroscopy. These concepts are discussed in the following sections.

1.1.1 *Linear Analytical Spectroscopy and Microscopy*

Three common linear spectroscopy techniques are UV/Vis spectroscopy, IR spectroscopy, and spontaneous Raman spectroscopy. Both UV/Vis spectroscopy and IR spectroscopy interrogate a molecule's energy levels with a broadband light source (e.g., a tungsten lamp or halogen lamp) and directly measure wavelength specific attenuation. The key difference between UV/Vis spectroscopy and IR spectroscopy is the energy transition being excited. Between 400-750 nm (the visible region), the absorption event is an electronic transition, whereas the near-IR region primarily excites vibrational transitions. In UV/Vis spectroscopy, the absorbance at each wavelength, A, is related to concentration through Beer's Law:

$$A = bc\varepsilon$$

where b is path length, c is concentration, and ε is the molar extinction coefficient, a constant representing the absorption cross section of a molecule at a particular wavelength. For a typical UV/Vis experiment, the path length is fixed, and the molar extinction coefficient is determined via calibration allowing for straightforward quantification of concentration. Based on the simplicity of UV/Vis spectroscopy, it is a widely employed quantitative technique. In contrast, IR spectroscopy is primarily used for molecular identification. The intrinsic, unique vibrational modes of a molecule act as a fingerprint which provides high precision molecular analysis. The sensitivity

of IR spectroscopy to detecting various functional groups has made it a widely employed spectroscopy technique as well.

Unfortunately, both techniques suffer from issues when extended to microscopy. UV/Vis spectroscopy begins to break down when a sample is turbid and light is attenuated by competing sources (e.g., elastic scattering). When applied to microscopy, scattering affects path length and hinders quantification. In addition to these issues, IR spectroscopy also suffers from strong water absorbance. Recent efforts have worked to mitigate the contribution of the water background and regain the analytical capability of IR spectroscopy.[11]

Fluorescence microscopy also relies on the absorption of light. Here, instead of measuring the attenuation of light transmitting through a sample, spontaneously emitted photons are collected from fluorescent molecules, known as fluorophores. Importantly, the emitted photons are lower energy, or red-shifted, from the absorbed photon which allows for simple chromatic separation of elastically scattered photons and fluorescence photons. For this reason, fluorescence microscopy is one of the most widely used analytical spectroscopy techniques. A typical linear fluorescence microscope employs a narrowband light source (e.g., laser or LED) chosen to excite a particular electronic transition within the sample (e.g., a known fluorescent stain) and an aperture, or pinhole, for optical sectioning. The pinhole is crucial as it rejects out of focus light which would otherwise convolute data interpretation and analysis. Other techniques for achieving optical sectioning have been demonstrated, notably the off-axis configuration common in light sheet fluorescence microscopy (LSFM).[12] The collected light is then filtered to remove the elastically scattered photons and the remaining photons are detected using a high-gain detector or camera, such as a PMT or CCD.

Fluorescence microscopy can be extended to quantify excited state dynamics of fluorophores. This technique is referred to as fluorescence lifetime microscopy (FLIM).[13,14] In FLIM, a fluorophore is excited and the number of fluorescent photons emitted as a function of time is measured. The resulting decay curve describes the stability of the electron in the excited state, known as the fluorescence lifetime. More stable excited electronic states will have longer lifetimes. Among other demonstrations, FLIM has been used to characterize metabolism within cells based on the intrinsic lifetime changes of NAD/NADH and FAD/FADH.[15–17]

Separate from the absorption based analytical spectroscopy techniques are the scattering-based techniques. Linear inelastic scattering, or spontaneous Raman scattering, is a widely used analytical spectroscopy technique used to identify molecular constituents of a sample. Spontaneous Raman scattering spectroscopy achieves molecular identification based on intrinsic, unique vibrational modes. In spontaneous Raman scattering, a monochromatic light source, typically a laser, is used to excite a molecule to a virtual state where the photon will be scattered elastically (no energy transfer) or inelastically (energy transfer). Energy flow from inelastic scattering can proceed in either direction: photon to molecule (Stokes) or molecule to photon (anti-Stokes). Stokes photons result from promoting a ground state molecule to vibrationally excited state, whereas anti-Stokes photons result from a vibrationally excited state molecule transferring its energy to the photon and relaxing back to ground state. Thus, Stokes photons are lower energy than elastically scattered photons and anti-Stokes photons are higher energy than elastically scattered photons. Under standard laboratory conditions, the majority of inelastically scattered photons are Stokes photons. In either case, the scattered photons are collected, and the elastically scattered photons are filtered out using a notch filter. The collected photons are then chromatically dispersed, collected using an array of detectors, and a Raman spectrum is achieved. Similar to

linear fluorescence microscopy, spontaneous Raman scattering microscopy requires the use of a pinhole to achieve optical sectioning. While spontaneous Raman scattering spectroscopy and microscopy are powerful techniques, spontaneous Raman scattering is inherently limited by weak signal and plagued by autofluorescence. To improve performance of Raman scattering spectroscopy, researchers have developed more sophisticated methods, including, but not limited to, resonance Raman spectroscopy and surface-enhanced Raman scattering (SERS) to dramatically increase signal sizes.

In resonance Raman spectroscopy, the excitation wavelength is tuned to approach the electronic transition of the molecule. As the virtual state approaches, or equals, the electronic transition, the Raman process is greatly enhanced.[18] In SERS, Raman signals are enhanced when the molecule of interest interacts with metal surfaces or nanostructures.[19] While the exact mechanism of enhancement is still under debate, SERS has demonstrated large enhancements up to 10^{11} enabling single molecule detection.[20] However, SERS enhancement can be unpredictable and challenging to reproduce.

Lastly, while elastic scattering is parasitic to the previously discussed analytical spectroscopy techniques, it forms the basis for other methods. For instance, Mie scattering is a theory used to calculate particle size and density in a turbid sample based on elastic scattering.[21] Mie scattering has been used for numerous applications including measuring red blood cell (RBC) size and the detection of malaria parasites.[22,23] Another important implementation of elastic scattering is optical coherence tomography (OCT). OCT is an interferometric imaging method that relies on the elastic scattering of photons from high refractive index structures to gain contrast. OCT has found tremendous utility in clinical biomedical imaging, most notably ophthalmology.[24,25]

In general, linear spectroscopy dominates analytical spectroscopy and microscopy due to advantages in instrument cost and access.

1.1.2 *Nonlinear Analytical Spectroscopy and Microscopy*

Two-photon excitation was first described theoretically by Maria Goeppert-Mayer in 1931 in her doctoral dissertation. Dr. Goeppert-Mayer predicted that given a high enough flux of photons, a molecule could simultaneously absorb two photons to reach an electronic excited state unreachable under linear absorption of one photon. This phenomenon, known as two-photon absorption (TPA), was demonstrated thirty years later in 1961. Importantly, the invention of the laser a year prior in 1960 enabled the first experimental observation of TPA.[26] Since then many other two-photon excited photophysical processes have been discovered. One subset of these processes is known as transient absorption spectroscopy (TAS) which is a nonlinear analytical spectroscopy used to characterize the excited state lifetime and dynamics of a molecule. In addition to TPA, three other main photophysical processes constitute TAS: ground-state bleaching (GSB), stimulated emission (SE), and excited state absorption (ESA).[27,28] Each process contributes to the overall TAS signal based on the electronic and vibrational structure of the molecule. All four processes are illustrated in Figure 1.2.

In a typical TAS experiment, two laser pulses – termed ‘pump’ pulse and ‘probe’ pulse – are employed. First an ensemble of molecules is excited, or pumped, to an intermediate state. Then the ensemble of molecules is probed at some time delay, τ, later. In TPA, the intermediate state is virtual (i.e., the molecule is not pumped to an electronic excited state) which means that TPA only occurs when the two pulses are temporally overlapped. In contrast, GSB, SE, and ESA proceed through a real intermediate state (i.e., the molecule is pumped to an allowed electronic state). Thus, the molecule remains in the excited state as dictated by the stability of that excited state. This is

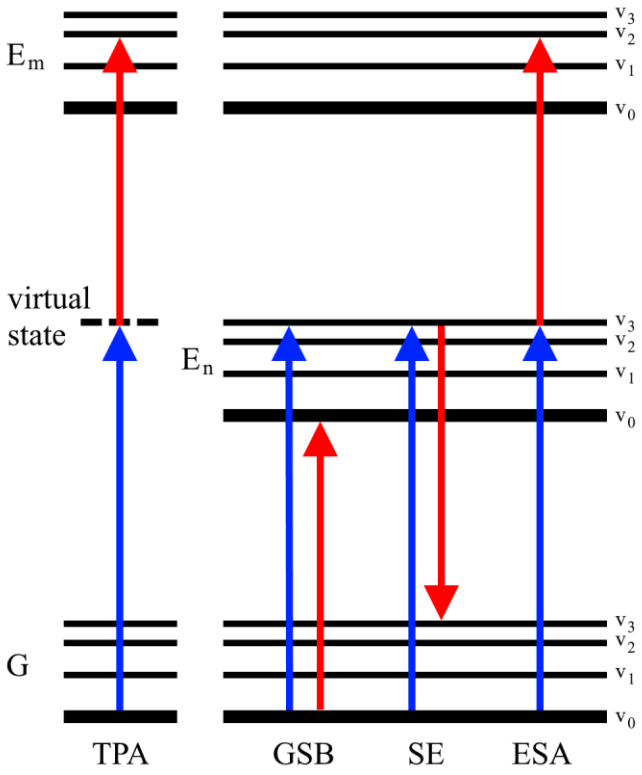

Figure 1.2. Energy level diagrams for four transient absorption spectroscopy process: two-photon absorption (TPA), ground-state bleaching (GSB), stimulated emission (SE), and excited state absorption (ESA).

typically referred to as the excited state lifetime or transient lifetime. In GSB, the ground state electrons are pumped to an excited state and the remaining ground state electrons are probed via a second ground state to excited state excitation. In SE, the probe pulse induces radiative decay of excited state electrons to relax back to the ground state. Here, the electron emits a photon of equal energy as the probe beam. In ESA, the probe pulse further excites the excited state electrons to an even higher energy state. All four processes – TPA, GSB, SE, and ESA – provide rich information about the electronic structure of a molecule. TAS has found immense popularity as an analytical microscopy technique. Transient absorption microscopy (TAM) has been employed to study both inorganic[29,30] and biomedical[31,32] samples.

In addition to TAM, two-photon excited fluorescence (2PEF) also makes use of nonlinear absorption to populate electronic excited states. In 2PEF the emitted photon is red-shifted relative to the sum of the excitation photons. In other words, if an electron absorbs photons of energy, E_1 and E_2, and emits a photon of energy, E_{em}, then $E_{em} < E_1 + E_2$. 2PEF can be performed with one laser pulse where two photons of the same energy are absorbed (degenerate 2PEF) or with two

laser pulses where two photons of different energy are absorbed (nondegenerate). In order to multiplex (i.e., collect multiple fluorescent contrasts simultaneously), many researchers turn to nondegenerate 2PEF.[33,34] Here, fluorophores can be excited simultaneously from three unique photon combinations: the degenerate 2PEF of each laser pulse and nondegenerate 2PEF from the combination. 2PEF is the most used nonlinear microscopy technique largely due to strong signal sizes, straightforward detection, and ease of instrumentation. As a result, a diverse and wide reaching palatte of fluorescent dye molecules have been synthesized to allow 2PEF microscopy of non-fluorescent structures.

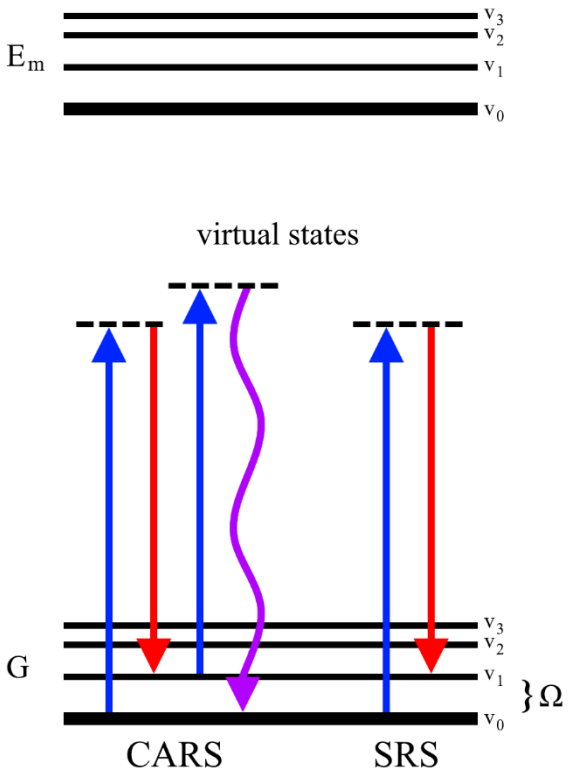

Figure 1.3. Energy level diagrams for two coherent Raman scattering (CRS) processes: coherent anti-Stokes Raman scattering (CARS) and stimulated Raman scattering (SRS).

Another nonlinear analytical spectroscopy that has gained popularity over the past few decades is coherent Raman scattering (CRS) spectroscopy.[35] CRS is the nonlinear analog to spontaneous Raman scattering, and thus, probes vibrational modes of a molecule. CRS was development to improve low signal size which severely limits the translation of spontaneous Raman scattering to microscopy. The improvement is achieved by stimulating the release of an inelastically scattered photon. CRS is a third order process that employs two laser pulses – termed 'pump' pulse and 'Stokes' pulse – with frequencies of ω_{pump} and ω_{Stokes}, respectively. One photon of each energy is combined to generate a beat

frequency ($\omega_v = \omega_{pump} - \omega_{Stokes}$). When the beat frequency matches a vibrational frequency (Ω) within the molecule it induces a vibrational coherence that modulates the refractive index of the material. Due to this requirement, CRS is typically performed with *a priori* knowledge of the system being interrogated so that appropriate laser pulses can be employed. However, CRS is also routinely performed by scanning different vibrational frequencies to determine the vibrational modes of molecule.[36,37] When the vibrational coherence is probed with a third photon (ω_3; either ω_{pump} or ω_{Stokes}), it is modulated by the beat frequency resulting in scattered frequencies of $\omega_3 + \omega_v$ and $\omega_3 - \omega_v$. These scattered frequencies give rise to the two main CRS techniques: coherent anti-Stokes scattering (CARS) and stimulated Raman scattering (SRS). Both are illustrated in Figure 1.3. In the case of CARS, a new higher frequency photon is generated at $\omega_{CARS} = 2\omega_{pump} - \omega_{Stokes}$. Thus, CARS photons can be separated chromatically and detected using a PMT or avalanche photodiode (APD). CARS microscopy has been employed in many fields such as pharmacokinetics[38,39], cancer biology[40], and label-free pathology[41].

While CARS is a powerful technique, two factors limit its capabilities. CARS signal is quadratic with concentration and it suffers from a non-resonant background.[42,43] Combined, these issues complicate quantification. As a result, many researchers have switched to using SRS, which does not suffer from these same limitations.[44–47] In the case of SRS, the signal photons have the same frequency as ω_{pump} and ω_{Stokes}. More specifically, a ω_{pump} photon is annihilated and a ω_{Stokes} is generated during an SRS event. As a result, the two types of SRS are known as stimulated Raman loss (SRL) and stimulated Raman gain (SRG). Both SRL and SRG are detected using a photodiode. SRS microscopy has been used to study neurotransmitter release[48], drug uptake[49], and metabolism[50,51] with high spatial and temporal resolution. To push the capabilities of SRS further, many research groups seek to improve the detection limit of SRS.

Recently, electronic pre-resonance SRS (epr-SRS) was developed as a nonlinear analog to linear resonance Raman spectroscopy. Under a similar working principle, as the pumped virtual state of a molecule approaches an electronic transition, epr-SRS has demonstrated enhancement factors of up to 10^5 allow for highly sensitive quantitative imaging of low abundance biomolecules.[52,53]

All nonlinear events require a high flux of photons given the low probability of such events. To meet this requirement ultrafast lasers (10^{-12} – 10^{-15} s) with high peak power are employed. Here, peak power refers to the amount of energy (or number of photons) in an interval of time. Thus, for the same number of photons, a temporally long pulse (10^{-12} s) will have a lower peak power than a temporally short pulse (10^{-15} s). For TAS and 2PEF, femtosecond (fs; 10^{-15} s) pulses are typically employed to provide the highest temporal resolution measurements and strongest nonlinear signals. For CRS, pulse duration and peak power present a unique trade off. Femtosecond pulses provide the highest signal, but the poorest spectral resolution. This relationship is discussed in detail in Chapter 4.

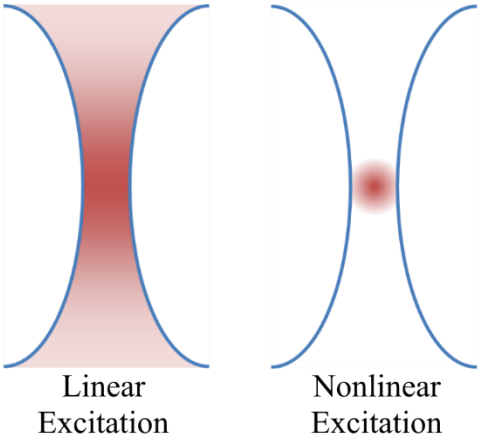

Figure 1.4. Excitation volumes for a linear process and a nonlinear process.

In contrast to linear microscopy, nonlinear microscopy benefits from intrinsic optical sectioning.[54,55] Due to the requirement of high photon density, nonlinear processes only occur at the focus of the laser beams. Thus, no pinhole or off axis detection scheme is required since out of focus excitation is negligible. This principle is illustrated in Figure 1.4 where the excitation volume is depicted in the shaded region.

1.1.3 *Pulse Modulation and Lock-in Detection*

Experimentally, nonlinear analytical spectroscopy and microscopy require intense ultrafast lasers to provide the required high flux of photons at the focus. Even still, many of the processes described in the previous section are weak. Moreover, in the case of TAS and SRS, the signal is carried by one of the excitation pulses. Extracting weak signals from an intense laser pulse is nearly impossible and thus prevents direct measurement of these processes. Rather, both processes require the use of pulse train modulation and de-modulation with a lock-in amplifier. This technique, illustrated in Figure 1.5, involves imparting a known modulation frequency onto the pump pulse train and detecting the transfer of the modulation frequency to the probe pulse train.

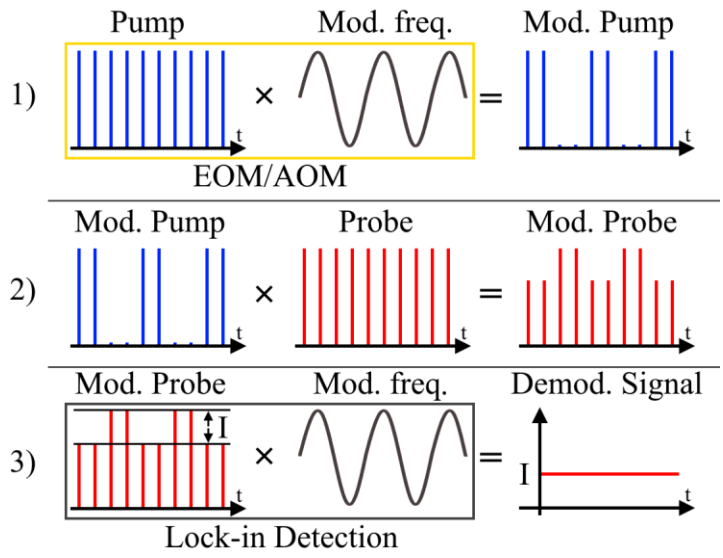

Figure 1.5. Pump train modulation and lock-in detection. 1) Pump pulse is intensity modulated a set modulation frequency using an electro-optic modulator (EOM) or acoustic-optic modulator (AOM). 2) Modulated pump and unmodulated probe interact at the sample to transfer the modulation frequency to the probe train. 3) Modulated probe train is demodulated at the modulation frequency by the lock-in amplifier.

This modulation is performed using an acousto-optic modulator (AOM) or and electro-optic modulator (EOM). An AOM achieves intensity modulation by propagating a sound wave at the desired modulation frequency through a crystalline material, such as glass or quartz. When a pulse train traverses the crystal, the pulse's frequency is shifted by the frequency of the sound wave, based on the Doppler effect. In contrast, an EOM achieves intensity modulation by first modulating the

pulse train's phase or polarization using an electro-optic material, such as lithium niobite ($LiNbO_3$). Here a DC current is applied to one axis of the crystal at the desired modulation frequency inducing a change in refractive index. When a pulse train traverses the crystal, its phase and polarization are modulated at the desired modulation frequency. The modulated pulse train is then separated into two amplitude modulated pulse trains using a polarizer or polarizing beam splitter.

As an example, assume a TAS experiment employs two ultrafast lasers – pump and probe – that have an 80 MHz (f_0) repetition rate. Every 12.5 ns (1/80 MHz) the laser will emit a laser pulse generating a constant train of pulses equally spaced in time. The pump pulse train will be modulated at a known frequency, for instance at 20 MHz ($f_0/4$) using an EOM, and incident upon the sample creating excited state populations at a frequency of 20 MHz. The probe beam will then interact with the modulated excited states, and in the event of a nonlinear process, the modulation frequency will be transferred to the probe beam. To extract the nonlinear signal, the probe beam will be detected, band pass filtered at the modulation frequency, and demodulated using the lock-in amplifier. Lock-in amplification multiplies the known modulation frequency (or reference reference) and the signal to extract the in-phase (X) and quadrature (Y) signals based on the phase difference between the reference frequency and the signal frequency.[56]

1.2 Analytical Biomedical Spectroscopy and Microscopy

Clinical and fundamental biomedical microscopy is performed on a wide range of systems including, but not limited to, *in vivo* and *ex vivo* tissue analysis and *in vitro* cell and tissue culture. One powerful qualitative clinical biomedical microscopy is histopathological staining of excised human tissues (*ex vivo*). Pathologists rely on a variety of stains and simple brightfield microscopy to enable precise pathological analysis and diagnosis. For instance, H&E staining is commonly

used to visualize tissue architecture and nuclear feature to provide intraoperative consultation.[57–59] H&E staining and its limitations are discussed in detail in Chapters 4 and 5.

Several techniques dominate *in vivo* clinical biomedical imaging, such as MRI, CT, and ultrasonography. While these techniques are not likely to be replaced soon, there is an unmet need for analytical microscopy techniques that can provide higher spatial and temporal resolution than clinically available. For instance, MRI is a powerful tool for studying the brain structure and function in patients based on blood oxygenation; however, the limited spatial resolution (~1 mm) is insufficient to resolve the interplay between blood and tissue at the capillary level. Recent reports suggest that red blood cell (RBC) oxygen saturation (sO_2) can vary dramatically between neighboring capillaries[60] demonstrating the need for higher spatial resolution imaging. Improving *in vivo* imaging capabilities for both clinical and fundamental biomedical imaging has become the focus of many research groups both in the clinic and in the laboratory.

When applying analytical spectroscopy and microscopy techniques to *in vivo* biomedical research, there are several important considerations. One key factor is imaging depth which is strongly affected by light absorption and scattering in tissue. Both absorption and scattering are wavelength dependent and can be mitigated with appropriate wavelength selection. As such, it is informative to study the absorption coefficients of intrinsic chemicals as a function of wavelength. Figure 1.6 provides the absorption coefficients (i.e., length a photon can travel through tissue before being absorbed) of water[61], hemoglobin, melanin[62], and fat[63]. Protein absorption was neglected as it predominately absorbs in the UV region. From Figure 1.6, the region from 650 nm to 1300 nm has the lowest absorption from intrinsic biomolecules and is referred to as the therapeutic window.[64,65] The benefit of using a longer wavelength can be understood through comparison of linear and nonlinear fluorescence. Consider the excitation of rhodamine B, a

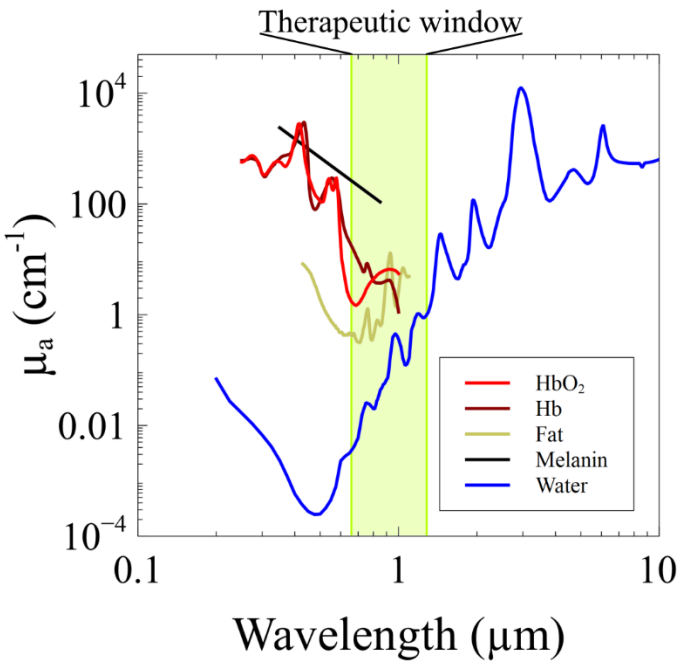

Figure 1.6. Absorption coefficients (μ_a) of various tissue constituents: oxyhemoglobin (HbO_2), deoxyhemoglobin (Hb), fat, melanin, and water. The shaded region illustrates the "therapeutic window" where light is less absorbed.

commonly used fluorescent dye. In linear fluorescence rhodamine B has peak absorption at 480 nm, while in degenerate 2PEF it has peak absorption around 850 nm.[66] In a direct comparison of peak excitation wavelength, rhodamine B likely has greater penetration depth at equal powers when excited with 2PEF than linear fluorescence due to less absorption and wavelength-dependent scattering from intrinsic biomolecules and structures. In practice, this direct comparison is insufficient and subject to other key differences in experimental setup such as excitation source, optical sectioning, and detection.

The consideration of imaging depth leads to the issue of phototoxicity. That is, increasing excitation power to compensate for tissue absorption and scattering can affect and even damage the tissue. In the example above, the optical power for linear fluorescence could be increased to compensate for the difference in power at the focus compared to 2PEF. However, increasing the optical power will increase the unwanted absorption by the tissue and can lead to severe tissue damage. Another key consideration when designing an analytical biomedical microscopy experiment is choosing to use a technique that typically requires labels, such as fluorescence, or a technique that is label-free, such as TAM and SRS. While fluorescence labels have completely

revolutionized biomedical imaging, they can perturb the natural physiology of the system. This concept will be discussed in Section 1.2.2 and in Chapter 6.

In the following sections, various applications, and demonstrations of biomedical microscopy to study hemodynamics and neurophotonics are discussed.

1.2.1 *Hemodynamics*

Hemodynamics, the dynamics of blood, play a crucial role in maintaining homeostasis throughout the body. Among other purposes, blood serves to ferry gases (e.g., oxygen (O_2) and carbon dioxide (CO_2)) and nutrients (e.g., glucose) throughout the body. As such, blood oxygen saturation (sO_2) is an important clinical metric for patient well-being. Typical sO_2 values in a healthy adult range from 95-100%, meaning that the majority of hemoglobin, the protein responsible for oxygen transport, is oxygenated. In the clinic, sO_2 is measured using a pulse oximeter which performs linear absorption of the hemoglobin in the arterial blood in the finger capillaries using two LEDs.[67,68] Here, the intrinsic absorption differences between oxyhemoglobin (HbO_2) and deoxyhemoglobin (Hb) are leveraged to ratiometrically quantify sO_2. By repeatedly collecting the absorption at each wavelength, pulse oximetry suppresses the background scattering from the tissue and quantifies the average sO_2 of pulsing arterial blood. As such, pulse oximetry is a powerful spectroscopy technique, however it cannot provide spatial information.

One key clinical biomedical microscopy technique for visualizing hemodynamics is optical coherence tomography angiography (OCTA) which is commonly used to image capillary networks in human retinas and skin. As mentioned in Section 1.1.1, OCT is an interferometric technique that measures elastically scattered photons at depths up to 3 mm.[69] OCTA leverages this technique to visualize flowing RBCs within capillaries. By collecting sequential images, the static tissue and moving tissue can be separated.

The primary targets of analytical biomedical spectroscopy for hemodynamics are typically blood flow and oxygen saturation (sO_2) or oxygen partial pressure (pO_2). Several linear and nonlinear absorption techniques have been developed to make use of the intrinsic absorption of hemoglobin and its variants. Photoacoustic microscopy (PAM) is one linear analytical microscopy technique that leverages the strong linear absorption of hemoglobin in the visible region. In PAM, a molecule absorbs light and dissipates energy non-radiatively. The energy absorbed by the molecule is released via vibrations and rotations causing a localized temperature spike. This temperature gradient induces a pressure wave that propagates through the tissue and can be measured using an ultrasound transducer. PAM has found great utility for *in vitro* and *in vivo* studies.[70,71] Notably, PAM has been used to monitor sO_2 *in vivo* by sequentially exciting RBCs with two LEDs and measuring the ratio of photoacoustic signal. Like pulse oximetry, a ratiometric approach leverages the intrinsic differences between HbO_2 and Hb to quantify sO_2.[72] Extending this principle further, PAM has been used to monitor metabolism in cancer cells *in vitro* by quantifying oxygen concentrations in the surrounding media.[3] While PAM is powerful, it is limited by the requirement of sequential excitation. Light scattering in tissue is wavelength dependent which must be considered when calculating sO_2 from a PAM measurement.[73] Additionally, acoustic waves heavily attenuate at changes in refractive index. Thus, water or other index matched media is required to detect acoustic signals which can significantly complicate experimental setup.

Nonlinear absorption spectroscopy has also explored the intrinsic absorption of hemoglobin. Fu et al. demonstrated that the intrinsic linear absorption differences between HbO_2 and Hb translates into different transient lifetimes with TAS.[31,32] Importantly, the TAS spectra of HbO_2 and Hb are wavelength dependent which provides tuneability in transient lifetime. TAM was further extended to measure blood flow in live zebrafish.[74] By collecting two parallel line

scans perpendicular to a capillary, the flow rate and flux of RBCs was quantified *in vivo*. Recently, TAM was employed to quantify the concentration of glycated hemoglobin (HbA1c) in human blood samples *ex vivo*.[75] Once again, researchers leveraged the differences in transient lifetime between HbO_2 and HbA1c to extract the concentration of HbA1c. In Chapters 2 and 3, TAM is employed to quantify hemoglobin concentration and oxygen saturation[76], respectively.

Another nonlinear analytical technique that has gained popularity for oxygen imaging in recent years is two-photon phosphorescence lifetime microscopy (2PLIM). Here, an exogenous probe is used to measure the partial pressure of oxygen, pO_2, based on the quenching of phosphorescence lifetime.[77–80] 2PLIM has been used to map out pO_2 in blood and tissue in the brain. However, phosphorescence lifetime is long lived (0.01 – 0.1 s) which limits the use 2PLIM in dynamic experiments where oxygenation can change rapidly.

1.2.2 *Neurophotonics*

Neurophotonics is another active field of biomedical research, both clinically and fundamentally. On the clinical side, the translation of SRS microscopy from bench to bedside is underway. SRS microscopy has been used to map the spatial distribution of proteins and lipids in variety of human and animal tissues, most notably human brain tumors.[81–85] In 2017, the Orringer group demonstrated rapid label-free histology of unprocessed surgical specimens. Importantly, the SRS microscopy was performed in the operating room with a 92% accuracy in predictive diagnosis as compared to traditional histopathological staining.[84] This work marks a crucial step in translating SRS microscopy into a clinical standard for intraoperative consultation. Further advancements to SRS microscopy for tissue imaging are demonstrated in Chapters 4 and 5.

Fundamental neurophotonics is also experiencing tremendous growth as a field. The brain consumes nearly 20% of bodily energy at rest.[86] To meet this large metabolic demand, the brain

relies on a dense network of blood vessels and capillaries.[87] One topic that has gained a lot of interest is neurovascular coupling (NVC), the interaction between hemodynamics and neuronal activity.[88–90] It is believed that NVC constitutes the basis of blood oxygen level dependence, or BOLD, functional magnetic resonance imaging (fMRI) where brain activity is measured by local changes in hemoglobin oxygenation.[91,92] However, as mentioned previously, MRI has poor spatial resolution so the mechanism behind NVC remains elusive. To provide the necessary spatial resolution for studying localized hemodynamics, many of the analytical microscopy techniques discussed in Section 1.2.1 are employed in neurophotonics to study oxygenation and the dense capillary network that supports the brain. Beyond those techniques discussed in Section 1.2.1, 2PEF is also used to visualize the vasculature of live mouse brains. Here, a dye molecule (e.g., fluorescein or Texas red) is conjugated with a high molecular weight dextran and intravenously injected into the mouse's blood compartment. Typically, a cranial window model is used to image the brain vasculature. In this model, a small craniotomy is performed (~ 3 mm in diameter) and a glass coverslip is installed. This model allows for both acute and longitudinal studies as the window can remain viable for over six months.[93] When efficiently excited, 2PEF has reach vasculature imaging depths of up to 2 mm.[94]

In addition to vasculature imaging, 2PEF is the leading technique for studying neuronal activity and intercellular interactions. Many techniques involve the application of a fluorescent dye either topically to the exposed cortex or intravenously. Unfortunately, application of dye through either route of administration can lead to animal complications. For example, sulforhodamine 101 (SR101) is a commonly used topical dye that stains astroctyes in the cortex. Recent reports have concluded that overexposure of SR101 to the exposed cortex can induce seizures.[95] As a result, there are countless transgenic mouse models that express fluorescent

proteins and alleviate the need for invasive dye application. For instance, genetically encoded calcium indicators, or GECIs, have allow researchers to study neuronal calcium dynamics without the need to invasive dye injections.[96]

1.3 Objective: Developing New Biomedical Spectroscopy and Microscopy Techniques

Nonlinear fluorescence has dominated *in vivo* nonlinear spectroscopy and microscopy in neurophotonics to date. Yet, the recent demonstrations of TAM for quantifying various hemodynamic properties suggest that TAM could provide crucial unmet insight. However, the lack of rigorous technical development and validation has thus far prevented TAM from being widely adopted into neurophotonic research. In Chapters 2 and 3, I demonstrate pivotal advancements in developing a TAM technique for quantifying hemoglobin concentration *ex vivo* and another technique for quantifying sO_2 *in vitro*[76], respectively. In Chapter 4, I optimize SRS microscopy for use in label-free pathology[97], and in Chapter 5, I apply the optimized system to identify and distinguish between various skull-based human tumors.[98] Lastly, in Chapter 6, I combine nonlinear absorption, Raman, and fluorescence to image cortical structures of mouse brains *in vivo.*

1.4 References

(1) Zhu, T.; Snaider, J. M.; Yuan, L.; Huang, L. Ultrafast Dynamic Microscopy of Carrier and Exciton Transport. *Annual Review of Physical Chemistry* **2019**, *70* (1), 219–244. https://doi.org/10.1146/annurev-physchem-042018-052605.
(2) Lami, V.; Weu, A.; Zhang, J.; Chen, Y.; Fei, Z.; Heeney, M.; Friend, R. H.; Vaynzof, Y. Visualizing the Vertical Energetic Landscape in Organic Photovoltaics. *Joule* **2019**, *3* (10), 2513–2534. https://doi.org/10.1016/j.joule.2019.06.018.
(3) Hai, P.; Imai, T.; Xu, S.; Zhang, R.; Aft, R. L.; Zou, J.; Wang, L. V. High-Throughput, Label-Free, Single-Cell Photoacoustic Microscopy of Intratumoral Metabolic Heterogeneity. *Nature Biomedical Engineering* **2019**, *3* (5), 381–391. https://doi.org/10.1038/s41551-019-0376-5.

(4) Ortmayr, K.; Dubuis, S.; Zampieri, M. Metabolic Profiling of Cancer Cells Reveals Genome-Wide Crosstalk between Transcriptional Regulators and Metabolism. *Nature Communications* **2019**, *10* (1), 1841. https://doi.org/10.1038/s41467-019-09695-9.
(5) Huang, K.-C.; Li, J.; Zhang, C.; Tan, Y.; Cheng, J.-X. Multiplex Stimulated Raman Scattering Imaging Cytometry Reveals Lipid-Rich Protrusions in Cancer Cells under Stress Condition. *iScience* **2020**, *23* (3), 100953. https://doi.org/10.1016/j.isci.2020.100953.
(6) van Staveren, W. C. G.; Solís, D. Y. W.; Hébrant, A.; Detours, V.; Dumont, J. E.; Maenhaut, C. Human Cancer Cell Lines: Experimental Models for Cancer Cells in Situ? For Cancer Stem Cells? *Biochimica et Biophysica Acta (BBA) - Reviews on Cancer* **2009**, *1795* (2), 92–103. https://doi.org/10.1016/j.bbcan.2008.12.004.
(7) Zitvogel, L.; Pitt, J. M.; Daillère, R.; Smyth, M. J.; Kroemer, G. Mouse Models in Oncoimmunology. *Nature Reviews Cancer* **2016**, *16* (12), 759–773. https://doi.org/10.1038/nrc.2016.91.
(8) Gengenbacher, N.; Singhal, M.; Augustin, H. G. Preclinical Mouse Solid Tumour Models: Status Quo, Challenges and Perspectives. *Nature Reviews Cancer* **2017**, *17* (12), 751–765. https://doi.org/10.1038/nrc.2017.92.
(9) Lampreht Tratar, U.; Horvat, S.; Cemazar, M. Transgenic Mouse Models in Cancer Research. *Front. Oncol.* **2018**, *8*. https://doi.org/10.3389/fonc.2018.00268.
(10) Skoog, D. A.; Holler, F. J.; Crouch, S. R. *Principles of Instrumental Analysis*; Thomson Brooks/Cole, 2007.
(11) Baker, M. J.; Trevisan, J.; Bassan, P.; Bhargava, R.; Butler, H. J.; Dorling, K. M.; Fielden, P. R.; Fogarty, S. W.; Fullwood, N. J.; Heys, K. A.; Hughes, C.; Lasch, P.; Martin-Hirsch, P. L.; Obinaju, B.; Sockalingum, G. D.; Sulé-Suso, J.; Strong, R. J.; Walsh, M. J.; Wood, B. R.; Gardner, P.; Martin, F. L. Using Fourier Transform IR Spectroscopy to Analyze Biological Materials. *Nat Protoc* **2014**, *9* (8), 1771–1791. https://doi.org/10.1038/nprot.2014.110.
(12) Power, R. M.; Huisken, J. A Guide to Light-Sheet Fluorescence Microscopy for Multiscale Imaging. *Nature Methods* **2017**, *14* (4), 360–373. https://doi.org/10.1038/nmeth.4224.
(13) Bastiaens, P. I. H.; Squire, A.; Bastiaens, P. I. H.; Squire, A.; Bastiaens, P. I. H.; Squire, A. Fluorescence Lifetime Imaging Microscopy: Spatial Resolution of Biochemical Processes in the Cell. *Trends in Cell Biology* **1999**, *9* (2), 48–52. https://doi.org/10.1016/S0962-8924(98)01410-X.
(14) Datta, R.; Heaster, T. M.; Sharick, J. T.; Gillette, A. A.; Skala, M. C. Fluorescence Lifetime Imaging Microscopy: Fundamentals and Advances in Instrumentation, Analysis, and Applications. *JBO* **2020**, *25* (7), 071203. https://doi.org/10.1117/1.JBO.25.7.071203.
(15) Skala, M. C.; Riching, K. M.; Bird, D. K.; Gendron-Fitzpatrick, A.; Eickhoff, J.; Eliceiri, K. W.; Keely, P. J.; Ramanujam, N. In Vivo Multiphoton Fluorescence Lifetime Imaging of Protein-Bound and Free NADH in Normal and Pre-Cancerous Epithelia. *J Biomed Opt* **2007**, *12* (2), 024014. https://doi.org/10.1117/1.2717503.
(16) Blacker, T. S.; Mann, Z. F.; Gale, J. E.; Ziegler, M.; Bain, A. J.; Szabadkai, G.; Duchen, M. R. Separating NADH and NADPH Fluorescence in Live Cells and Tissues Using FLIM. *Nature Communications* **2014**, *5* (1), 3936. https://doi.org/10.1038/ncomms4936.
(17) Schaefer, P. M.; Kalinina, S.; Rueck, A.; Arnim, C. A. F. von; Einem, B. von. NADH Autofluorescence—A Marker on Its Way to Boost Bioenergetic Research. *Cytometry Part A* **2019**, *95* (1), 34–46. https://doi.org/10.1002/cyto.a.23597.

(18) Efremov, E. V.; Ariese, F.; Gooijer, C. Achievements in Resonance Raman Spectroscopy: Review of a Technique with a Distinct Analytical Chemistry Potential. *Analytica Chimica Acta* **2008**, *606* (2), 119–134. https://doi.org/10.1016/j.aca.2007.11.006.
(19) Schlücker, S. Surface-Enhanced Raman Spectroscopy: Concepts and Chemical Applications. *Angewandte Chemie International Edition* **2014**, *53* (19), 4756–4795. https://doi.org/10.1002/anie.201205748.
(20) Blackie, E. J.; Le Ru, E. C.; Etchegoin, P. G. Single-Molecule Surface-Enhanced Raman Spectroscopy of Nonresonant Molecules. *J. Am. Chem. Soc.* **2009**, *131* (40), 14466–14472. https://doi.org/10.1021/ja905319w.
(21) Wriedt, T. Mie Theory: A Review. In *The Mie Theory: Basics and Applications*; Hergert, W., Wriedt, T., Eds.; Springer Series in Optical Sciences; Springer: Berlin, Heidelberg, 2012; pp 53–71. https://doi.org/10.1007/978-3-642-28738-1_2.
(22) Steinke, J. M.; Shepherd, A. P. Comparison of Mie Theory and the Light Scattering of Red Blood Cells. *Appl Opt* **1988**, *27* (19), 4027–4033. https://doi.org/10.1364/AO.27.004027.
(23) Serebrennikova, Y. M.; Patel, J.; Garcia-Rubio, L. H. Interpretation of the Ultraviolet-Visible Spectra of Malaria Parasite *Plasmodium Falciparum*. *Appl. Opt., AO* **2010**, *49* (2), 180–188. https://doi.org/10.1364/AO.49.000180.
(24) Zysk, A. M.; Nguyen, F. T.; Oldenburg, A. L.; Marks, D. L.; Boppart, S. A. Optical Coherence Tomography: A Review of Clinical Development from Bench to Bedside. *J Biomed Opt* **2007**, *12* (5), 051403. https://doi.org/10.1117/1.2793736.
(25) Adhi, M.; Duker, J. S. Optical Coherence Tomography – Current and Future Applications. *Curr Opin Ophthalmol* **2013**, *24* (3), 213–221. https://doi.org/10.1097/ICU.0b013e32835f8bf8.
(26) Kaiser, W.; Garrett, C. G. B. Two-Photon Excitation in Ca${\mathrm{F}}_{2}$: ${\mathrm{Eu}}^{2+}$. *Phys. Rev. Lett.* **1961**, *7* (6), 229–231. https://doi.org/10.1103/PhysRevLett.7.229.
(27) Berera, R.; van Grondelle, R.; Kennis, J. T. M. Ultrafast Transient Absorption Spectroscopy: Principles and Application to Photosynthetic Systems. *Photosynth Res* **2009**, *101* (2–3), 105–118. https://doi.org/10.1007/s11120-009-9454-y.
(28) Ruckebusch, C.; Sliwa, M.; Pernot, P.; de Juan, A.; Tauler, R. Comprehensive Data Analysis of Femtosecond Transient Absorption Spectra: A Review. *Journal of Photochemistry and Photobiology C: Photochemistry Reviews* **2012**, *13* (1), 1–27. https://doi.org/10.1016/j.jphotochemrev.2011.10.002.
(29) Hill, A. H.; Smyser, K. E.; Kennedy, C. L.; Massaro, E. S.; Grumstrup, E. M. Screened Charge Carrier Transport in Methylammonium Lead Iodide Perovskite Thin Films. *J. Phys. Chem. Lett.* **2017**, *8* (5), 948–953. https://doi.org/10.1021/acs.jpclett.7b00046.
(30) Hill, A. H.; Kennedy, C. L.; Massaro, E. S.; Grumstrup, E. M. Perovskite Carrier Transport: Disentangling the Impacts of Effective Mass and Scattering Time Through Microscopic Optical Detection. *J. Phys. Chem. Lett.* **2018**, *9* (11), 2808–2813. https://doi.org/10.1021/acs.jpclett.8b00652.
(31) Fu, D.; Ye, T.; Matthews, T. E.; Chen, B. J.; Yurtserver, G.; Warren, W. S. High-Resolution *in Vivo* Imaging of Blood Vessels without Labeling. *Opt. Lett., OL* **2007**, *32* (18), 2641–2643. https://doi.org/10.1364/OL.32.002641.
(32) Fu, D.; Matthews, T. E.; Ye, T.; Piletic, I. R.; Warren, W. S. Label-Free in Vivo Optical Imaging of Microvasculature and Oxygenation Level. *J Biomed Opt* **2008**, *13* (4), 040503. https://doi.org/10.1117/1.2968260.

(33) Mahou, P.; Zimmerley, M.; Loulier, K.; Matho, K. S.; Labroille, G.; Morin, X.; Supatto, W.; Livet, J.; Débarre, D.; Beaurepaire, E. Multicolor Two-Photon Tissue Imaging by Wavelength Mixing. *Nature Methods* **2012**, *9* (8), 815–818. https://doi.org/10.1038/nmeth.2098.
(34) Perillo, E. P.; Jarrett, J. W.; Liu, Y.-L.; Hassan, A.; Fernée, D. C.; Goldak, J. R.; Bonteanu, A.; Spence, D. J.; Yeh, H.-C.; Dunn, A. K. Two-Color Multiphoton in Vivo Imaging with a Femtosecond Diamond Raman Laser. *Light: Science & Applications* **2017**, *6* (11), e17095–e17095. https://doi.org/10.1038/lsa.2017.95.
(35) Cheng, J.-X.; Xie, X. S. *Coherent Raman Scattering Microscopy*; CRC Press, 2012.
(36) Fu, D.; Holtom, G.; Freudiger, C.; Zhang, X.; Xie, X. S. Fast Hyperspectral Imaging with Stimulated Raman Scattering by Chirped Femtosecond Lasers. *J Phys Chem B* **2013**, *117* (16), 4634–4640. https://doi.org/10.1021/jp308938t.
(37) Fu, D.; Holtom, G.; Freudiger, C.; Zhang, X.; Xie, X. S. Hyperspectral Imaging with Stimulated Raman Scattering by Chirped Femtosecond Lasers. *J. Phys. Chem. B* **2013**, *117* (16), 4634–4640. https://doi.org/10.1021/jp308938t.
(38) Kang, E.; Wang, H.; Kwon, I. K.; Robinson, J.; Park, K.; Cheng, J.-X. In Situ Visualization of Paclitaxel Distribution and Release by Coherent Anti-Stokes Raman Scattering Microscopy. *Anal. Chem.* **2006**, *78* (23), 8036–8043. https://doi.org/10.1021/ac061218s.
(39) Kang, E.; Robinson, J.; Park, K.; Cheng, J.-X. Paclitaxel Distribution in Poly(Ethylene Glycol) / Poly(Lactide-Co-Glycolic Acid) Blends and Its Release Visualized by Coherent Anti-Stokes Raman Scattering Microscopy. *J Control Release* **2007**, *122* (3), 261–268. https://doi.org/10.1016/j.jconrel.2007.05.007.
(40) Hou, J.; Williams, J.; Botvinick, E. L.; Potma, E. O.; Tromberg, B. J. Visualization of Breast Cancer Metabolism Using Multimodal Nonlinear Optical Microscopy of Cellular Lipids and Redox State. *Cancer Res* **2018**, *78* (10), 2503–2512. https://doi.org/10.1158/0008-5472.CAN-17-2618.
(41) Niedieker, D.; GrosserÜschkamp, F.; Schreiner, A.; Barkovits, K.; Kötting, C.; Marcus, K.; Gerwert, K.; Vorgerd, M. Label-Free Identification of Myopathological Features with Coherent Anti-Stokes Raman Scattering. *Muscle Nerve* **2018**, *58* (3), 456–459. https://doi.org/10.1002/mus.26140.
(42) Min, W.; Freudiger, C. W.; Lu, S.; Xie, X. S. Coherent Nonlinear Optical Imaging: Beyond Fluorescence Microscopy. *Annu Rev Phys Chem* **2011**, *62*, 507–530. https://doi.org/10.1146/annurev.physchem.012809.103512.
(43) Cheng, J.-X.; Xie, X. S. Vibrational Spectroscopic Imaging of Living Systems: An Emerging Platform for Biology and Medicine. *Science* **2015**, *350* (6264). https://doi.org/10.1126/science.aaa8870.
(44) Freudiger, C. W.; Min, W.; Saar, B. G.; Lu, S.; Holtom, G. R.; He, C.; Tsai, J. C.; Kang, J. X.; Xie, X. S. Label-Free Biomedical Imaging with High Sensitivity by Stimulated Raman Scattering Microscopy. *Science* **2008**, *322* (5909), 1857–1861. https://doi.org/10.1126/science.1165758.
(45) Fu, D. Quantitative Chemical Imaging with Stimulated Raman Scattering Microscopy. *Curr Opin Chem Biol* **2017**, *39*, 24–31. https://doi.org/10.1016/j.cbpa.2017.05.002.
(46) Hill, A. H.; Fu, D. Cellular Imaging Using Stimulated Raman Scattering Microscopy. *Anal. Chem.* **2019**, *91* (15), 9333–9342. https://doi.org/10.1021/acs.analchem.9b02095.
(47) Yue, S.; Cheng, J.-X. Deciphering Single Cell Metabolism by Coherent Raman Scattering Microscopy. *Curr Opin Chem Biol* **2016**, *33*, 46–57. https://doi.org/10.1016/j.cbpa.2016.05.016.

(48) Fu, D.; Yang, W.; Xie, X. S. Label-Free Imaging of Neurotransmitter Acetylcholine at Neuromuscular Junctions with Stimulated Raman Scattering. *J. Am. Chem. Soc.* **2017**, *139* (2), 583–586. https://doi.org/10.1021/jacs.6b10727.
(49) Fu, D.; Zhou, J.; Zhu, W. S.; Manley, P. W.; Wang, Y. K.; Hood, T.; Wylie, A.; Xie, X. S. Imaging the Intracellular Distribution of Tyrosine Kinase Inhibitors in Living Cells with Quantitative Hyperspectral Stimulated Raman Scattering. *Nat Chem* **2014**, *6* (7), 614–622. https://doi.org/10.1038/nchem.1961.
(50) Wei, L.; Yu, Y.; Shen, Y.; Wang, M. C.; Min, W. Vibrational Imaging of Newly Synthesized Proteins in Live Cells by Stimulated Raman Scattering Microscopy. *PNAS* **2013**, *110* (28), 11226–11231. https://doi.org/10.1073/pnas.1303768110.
(51) Shi, L.; Zheng, C.; Shen, Y.; Chen, Z.; Silveira, E. S.; Zhang, L.; Wei, M.; Liu, C.; de Sena-Tomas, C.; Targoff, K.; Min, W. Optical Imaging of Metabolic Dynamics in Animals. *Nat Commun* **2018**, *9*. https://doi.org/10.1038/s41467-018-05401-3.
(52) Wei, L.; Chen, Z.; Shi, L.; Long, R.; Anzalone, A. V.; Zhang, L.; Hu, F.; Yuste, R.; Cornish, V. W.; Min, W. Super-Multiplex Vibrational Imaging. *Nature* **2017**, *544* (7651), 465–470. https://doi.org/10.1038/nature22051.
(53) Wei, L.; Min, W. Electronic Preresonance Stimulated Raman Scattering Microscopy. *J Phys Chem Lett* **2018**, *9* (15), 4294–4301. https://doi.org/10.1021/acs.jpclett.8b00204.
(54) Cy, D.; K, K.; P, S. Characterizing Point Spread Functions of Two-Photon Fluorescence Microscopy in Turbid Medium. *J Biomed Opt* **2003**, *8* (3), 450–459. https://doi.org/10.1117/1.1578644.
(55) Doi, A.; Oketani, R.; Nawa, Y.; Fujita, K. High-Resolution Imaging in Two-Photon Excitation Microscopy Using in Situ Estimations of the Point Spread Function. *Biomed Opt Express* **2017**, *9* (1), 202–213. https://doi.org/10.1364/BOE.9.000202.
(56) He, R.; Xu, Y.; Zhang, L.; Ma, S.; Wang, X.; Ye, D.; Ji, M. Dual-Phase Stimulated Raman Scattering Microscopy for Real-Time Two-Color Imaging. *Optica, OPTICA* **2017**, *4* (1), 44–47. https://doi.org/10.1364/OPTICA.4.000044.
(57) King, D. F.; King, L. A. C. A Brief Historical Note on Staining by Hematoxylin and Eosin. *The American Journal of Dermatopathology* **1986**, *8* (2), 168.
(58) Chan, J. K. C. The Wonderful Colors of the Hematoxylin–Eosin Stain in Diagnostic Surgical Pathology. *Int J Surg Pathol* **2014**, *22* (1), 12–32. https://doi.org/10.1177/1066896913517939.
(59) Schneider, J. P.; Schulz, T.; Schmidt, F.; Dietrich, J.; Lieberenz, S.; Trantakis, C.; Seifert, V.; Kellermann, S.; Schober, R.; Schaffranietz, L.; Laufer, M.; Kahn, T. Gross-Total Surgery of Supratentorial Low-Grade Gliomas under Intraoperative MR Guidance. *American Journal of Neuroradiology* **2001**, *22* (1), 89–98.
(60) Gagnon, L.; Smith, A. F.; Boas, D. A.; Devor, A.; Secomb, T. W.; Sakadžić, S. Modeling of Cerebral Oxygen Transport Based on In Vivo Microscopic Imaging of Microvascular Network Structure, Blood Flow, and Oxygenation. *Front. Comput. Neurosci.* **2016**, *10*. https://doi.org/10.3389/fncom.2016.00082.
(61) Hale, G. M.; Querry, M. R. Optical Constants of Water in the 200-Nm to 200-Mm Wavelength Region. *Appl. Opt., AO* **1973**, *12* (3), 555–563. https://doi.org/10.1364/AO.12.000555.
(62) Jacques, S. L.; McAuliffe, D. J. The Melanosome: Threshold Temperature for Explosive Vaporization and Internal Absorption Coefficient During Pulsed Laser Irradiation.

Photochemistry and Photobiology **1991**, *53* (6), 769–775. https://doi.org/10.1111/j.1751-1097.1991.tb09891.x.
(63) Veen, R. L. P. van; Sterenborg, H. J. C. M.; Pifferi, A.; Torricelli, A.; Cubeddu, R. Determination of VIS- NIR Absorption Coefficients of Mammalian Fat, with Time- and Spatially Resolved Diffuse Reflectance and Transmission Spectroscopy. In *Biomedical Topical Meeting (2004), paper SF4*; Optical Society of America, 2004; p SF4. https://doi.org/10.1364/BIO.2004.SF4.
(64) Vogel, A.; Venugopalan, V. Mechanisms of Pulsed Laser Ablation of Biological Tissues. *Chem. Rev.* **2003**, *103* (2), 577–644. https://doi.org/10.1021/cr010379n.
(65) Jacques, S. L. Optical Properties of Biological Tissues: A Review. *Phys. Med. Biol.* **2013**, *58* (11), R37–R61. https://doi.org/10.1088/0031-9155/58/11/R37.
(66) Makarov, N. S.; Drobizhev, M.; Rebane, A. Two-Photon Absorption Standards in the 550-1600 Nm Excitation Wavelength Range. *Opt. Express* **2008**, *16* (6), 4029. https://doi.org/10.1364/OE.16.004029.
(67) Chan, E. D.; Chan, M. M.; Chan, M. M. Pulse Oximetry: Understanding Its Basic Principles Facilitates Appreciation of Its Limitations. *Respiratory Medicine* **2013**, *107* (6), 789–799. https://doi.org/10.1016/j.rmed.2013.02.004.
(68) Khan, Y.; Han, D.; Pierre, A.; Ting, J.; Wang, X.; Lochner, C. M.; Bovo, G.; Yaacobi-Gross, N.; Newsome, C.; Wilson, R.; Arias, A. C. A Flexible Organic Reflectance Oximeter Array. *PNAS* **2018**, *115* (47), E11015–E11024. https://doi.org/10.1073/pnas.1813053115.
(69) Sharma, U.; Chang, E. W.; Yun, S. H. Long-Wavelength Optical Coherence Tomography at 1.7 Mm for Enhanced Imaging Depth. *Opt Express* **2008**, *16* (24), 19712–19723.
(70) Xu, M.; Wang, L. V. Photoacoustic Imaging in Biomedicine. *Review of Scientific Instruments* **2006**, *77* (4), 041101. https://doi.org/10.1063/1.2195024.
(71) Attia, A. B. E.; Balasundaram, G.; Moothanchery, M.; Dinish, U. S.; Bi, R.; Ntziachristos, V.; Olivo, M. A Review of Clinical Photoacoustic Imaging: Current and Future Trends. *Photoacoustics* **2019**, *16*, 100144. https://doi.org/10.1016/j.pacs.2019.100144.
(72) Wang, L.; Maslov, K.; Wang, L. V. Single-Cell Label-Free Photoacoustic Flowoxigraphy in Vivo. *PNAS* **2013**, *110* (15), 5759–5764. https://doi.org/10.1073/pnas.1215578110.
(73) Rajian, J. R.; Carson, P. L.; Wang, X. Quantitative Photoacoustic Measurement of Tissue Optical Absorption Spectrum Aided by an Optical Contrast Agent. *Opt Express* **2009**, *17* (6), 4879–4889.
(74) Chen, T.; Huang, Y. Label-Free Transient Absorption Microscopy for Red Blood Cell Flow Velocity Measurement in Vivo. *Anal. Chem.* **2017**, *89* (19), 10120–10123. https://doi.org/10.1021/acs.analchem.7b01952.
(75) Dong, P.-T.; Lin, H.; Huang, K.-C.; Cheng, J.-X. Label-Free Quantitation of Glycated Hemoglobin in Single Red Blood Cells by Transient Absorption Microscopy and Phasor Analysis. *Science Advances* **2019**, *5* (5), eaav0561. https://doi.org/10.1126/sciadv.aav0561.
(76) Francis, A. T.; Berry, K.; Thomas, E. C.; Hill, A. H.; Fu, D. In Vitro Quantification of Single Red Blood Cell Oxygen Saturation by Femtosecond Transient Absorption Microscopy. *J. Phys. Chem. Lett.* **2019**, 3312–3317. https://doi.org/10.1021/acs.jpclett.9b01116.
(77) Sakadžić, S.; Roussakis, E.; Yaseen, M. A.; Mandeville, E. T.; Srinivasan, V. J.; Arai, K.; Ruvinskaya, S.; Devor, A.; Lo, E. H.; Vinogradov, S. A.; Boas, D. A. Two-Photon High-Resolution Measurement of Partial Pressure of Oxygen in Cerebral Vasculature and Tissue. *Nat Methods* **2010**, *7* (9), 755–759. https://doi.org/10.1038/nmeth.1490.

(78) Finikova, O. S.; Lebedev, A. Y.; Aprelev, A.; Troxler, T.; Gao, F.; Garnacho, C.; Muro, S.; Hochstrasser, R. M.; Vinogradov, S. A. Oxygen Microscopy by Two-Photon-Excited Phosphorescence. *Chemphyschem* **2008**, *9* (12), 1673–1679. https://doi.org/10.1002/cphc.200800296.
(79) Lecoq, J.; Parpaleix, A.; Roussakis, E.; Ducros, M.; Houssen, Y. G.; Vinogradov, S. A.; Charpak, S. Simultaneous Two-Photon Imaging of Oxygen and Blood Flow in Deep Cerebral Vessels. *Nat Med* **2011**, *17* (7), 893–898. https://doi.org/10.1038/nm.2394.
(80) Xu, K.; Boas, D. A.; Sakadžić, S.; LaManna, J. C. Brain Tissue PO2 Measurement During Normoxia and Hypoxia Using Two-Photon Phosphorescence Lifetime Microscopy. *Adv Exp Med Biol* **2017**, *977*, 149–153. https://doi.org/10.1007/978-3-319-55231-6_20.
(81) Ji, M.; Orringer, D. A.; Freudiger, C. W.; Ramkissoon, S.; Liu, X.; Lau, D.; Golby, A. J.; Norton, I.; Hayashi, M.; Agar, N. Y. R.; Young, G. S.; Spino, C.; Santagata, S.; Camelo-Piragua, S.; Ligon, K. L.; Sagher, O.; Xie, X. S. Rapid, Label-Free Detection of Brain Tumors with Stimulated Raman Scattering Microscopy. *Science Translational Medicine* **2013**, *5* (201), 201ra119-201ra119. https://doi.org/10.1126/scitranslmed.3005954.
(82) Ji, M.; Lewis, S.; Camelo-Piragua, S.; Ramkissoon, S. H.; Snuderl, M.; Venneti, S.; Fisher-Hubbard, A.; Garrard, M.; Fu, D.; Wang, A. C.; Heth, J. A.; Maher, C. O.; Sanai, N.; Johnson, T. D.; Freudiger, C. W.; Sagher, O.; Xie, X. S.; Orringer, D. A. Detection of Human Brain Tumor Infiltration with Quantitative Stimulated Raman Scattering Microscopy. *Science Translational Medicine* **2015**, *7* (309), 309ra163-309ra163. https://doi.org/10.1126/scitranslmed.aab0195.
(83) Lu, F.-K.; Calligaris, D.; Olubiyi, O. I.; Norton, I.; Yang, W.; Santagata, S.; Xie, X. S.; Golby, A. J.; Agar, N. Y. R. Label-Free Neurosurgical Pathology with Stimulated Raman Imaging. *Cancer Res.* **2016**, *76* (12), 3451–3462. https://doi.org/10.1158/0008-5472.CAN-16-0270.
(84) Orringer, D. A.; Pandian, B.; Niknafs, Y. S.; Hollon, T. C.; Boyle, J.; Lewis, S.; Garrard, M.; Hervey-Jumper, S. L.; Garton, H. J. L.; Maher, C. O.; Heth, J. A.; Sagher, O.; Wilkinson, D. A.; Snuderl, M.; Venneti, S.; Ramkissoon, S. H.; McFadden, K. A.; Fisher-Hubbard, A.; Lieberman, A. P.; Johnson, T. D.; Xie, X. S.; Trautman, J. K.; Freudiger, C. W.; Camelo-Piragua, S. Rapid Intraoperative Histology of Unprocessed Surgical Specimens via Fibre-Laser-Based Stimulated Raman Scattering Microscopy. *Nature Biomedical Engineering* **2017**, *1* (2), 1–13. https://doi.org/10.1038/s41551-016-0027.
(85) Hollon, T. C.; Lewis, S.; Pandian, B.; Niknafs, Y. S.; Garrard, M. R.; Garton, H.; Maher, C. O.; McFadden, K.; Snuderl, M.; Lieberman, A. P.; Muraszko, K.; Camelo-Piragua, S.; Orringer, D. A. Rapid Intraoperative Diagnosis of Pediatric Brain Tumors Using Stimulated Raman Histology. *Cancer Res.* **2018**, *78* (1), 278–289. https://doi.org/10.1158/0008-5472.CAN-17-1974.
(86) Raichle, M. E.; Gusnard, D. A. Appraising the Brain's Energy Budget. *PNAS* **2002**, *99* (16), 10237–10239. https://doi.org/10.1073/pnas.172399499.
(87) Blinder, P.; Tsai, P. S.; Kaufhold, J. P.; Knutsen, P. M.; Suhl, H.; Kleinfeld, D. The Cortical Angiome: An Interconnected Vascular Network with Noncolumnar Patterns of Blood Flow. *Nat. Neurosci.* **2013**, *16* (7), 889–897. https://doi.org/10.1038/nn.3426.
(88) Muoio, V.; Persson, P. B.; Sendeski, M. M. The Neurovascular Unit - Concept Review. *Acta Physiol (Oxf)* **2014**, *210* (4), 790–798. https://doi.org/10.1111/apha.12250.

(89) Huneau, C.; Benali, H.; Chabriat, H. Investigating Human Neurovascular Coupling Using Functional Neuroimaging: A Critical Review of Dynamic Models. *Front Neurosci* **2015**, *9*. https://doi.org/10.3389/fnins.2015.00467.
(90) Iadecola, C. The Neurovascular Unit Coming of Age: A Journey through Neurovascular Coupling in Health and Disease. *Neuron* **2017**, *96* (1), 17–42. https://doi.org/10.1016/j.neuron.2017.07.030.
(91) Logothetis, N. K. The Underpinnings of the BOLD Functional Magnetic Resonance Imaging Signal. *J. Neurosci.* **2003**, *23* (10), 3963–3971. https://doi.org/10.1523/JNEUROSCI.23-10-03963.2003.
(92) Ekstrom, A. How and When the FMRI BOLD Signal Relates to Underlying Neural Activity: The Danger in Dissociation. *Brain Res Rev* **2010**, *62* (2), 233–244. https://doi.org/10.1016/j.brainresrev.2009.12.004.
(93) Holtmaat, A.; Bonhoeffer, T.; Chow, D. K.; Chuckowree, J.; De Paola, V.; Hofer, S. B.; Hübener, M.; Keck, T.; Knott, G.; Lee, W.-C. A.; Mostany, R.; Mrsic-Flogel, T. D.; Nedivi, E.; Portera-Cailliau, C.; Svoboda, K.; Trachtenberg, J. T.; Wilbrecht, L. Long-Term, High-Resolution Imaging in the Mouse Neocortex through a Chronic Cranial Window. *Nature Protocols* **2009**, *4* (8), 1128–1144. https://doi.org/10.1038/nprot.2009.89.
(94) Cheng, H.; Tong, S.; Deng, X.; Liu, H.; Du, Y.; He, C.; Qiu, P.; Wang, K. Deep-Brain 2-Photon Fluorescence Microscopy in Vivo Excited at the 1700 Nm Window. *Opt. Lett., OL* **2019**, *44* (17), 4432–4435. https://doi.org/10.1364/OL.44.004432.
(95) Rasmussen, R.; Nedergaard, M.; Petersen, N. C. Sulforhodamine 101, a Widely Used Astrocyte Marker, Can Induce Cortical Seizure-like Activity at Concentrations Commonly Used. *Scientific Reports* **2016**, *6* (1), 30433. https://doi.org/10.1038/srep30433.
(96) Lin, M. Z.; Schnitzer, M. J. Genetically Encoded Indicators of Neuronal Activity. *Nat Neurosci* **2016**, *19* (9), 1142–1153. https://doi.org/10.1038/nn.4359.
(97) Francis, A.; Berry, K.; Chen, Y.; Figueroa, B.; Fu, D. Label-Free Pathology by Spectrally Sliced Femtosecond Stimulated Raman Scattering (SRS) Microscopy. *PLOS ONE* **2017**, *12* (5), e0178750. https://doi.org/10.1371/journal.pone.0178750.
(98) Shin, K. S.; Francis, A. T.; Hill, A. H.; Laohajaratsang, M.; Cimino, P. J.; Latimer, C. S.; Gonzalez-Cuyar, L. F.; Sekhar, L. N.; Juric-Sekhar, G.; Fu, D. Intraoperative Assessment of Skull Base Tumors Using Stimulated Raman Scattering Microscopy. *Sci Rep* **2019**, *9* (1), 20392. https://doi.org/10.1038/s41598-019-56932-8.

Chapter 2. DIRECT QUANTIFICATION OF SINGLE RED BLOOD CELL HEMOGLOBIN CONCENTRATION WITH MULTIPHOTON MICROSCOPY

2.1 INTRODUCTION

Blood disorders and diseases, such as sickle cell anemia and thalassemia, and blood-borne infections, such as malaria, affect millions of people annually. These pathologies often affect the shape, number, and contents of red blood cells (RBCs) dramatically. For instance, the concentration of hemoglobin in a RBC is drastically reduced in both thalassemia and malaria which can impact the amount of oxygen a RBC can ferry throughout the body. This and other impacts on the blood compartment, in turn, can result in organ damage and death.[1,2] Thus, metrics like hematocrit (the volume fraction of RBCs in whole blood), mean corpuscular hemoglobin concentration (MCHC), red blood cell distribution width (RDW), and mean cell volume (MCV) are useful pathological metrics for identification and monitoring of blood disorders, diseases, and infections. Typically, these measurements are performed using an automated cell counter of freshly collected blood, which requires ~20-30 μL of whole blood. While this process is suitable for larger animals (e.g., humans), serial blood collection can be prohibitory for rodent disease model and drug discovery experiments. Most institutional limits for blood collection from a mouse are ~1% of total body weight, equivalent to 250 μL of blood from a 25 g mouse every two weeks.[3] Dilution can be used to mitigate sample size restraints, but the accuracy and precision of diluted blood measurements vary.[4] Moreover, MCHC measurements via cell counting are an ensemble measurement which may fail to fully characterize the pathology. Single RBC analysis could

provide necessary insight into the heterogeneity of MCHC and enable comprehensive monitoring of disease process and therapeutic response.

Microscopy-based methods offer an attractive route for single RBC quantification of these metrics and they require smaller sample volumes than cell counting techniques. One such technique is spectroscopic phase microscopy (SPM) which can quantify cell dry mass, MCV, RDW, and MCHC.[5,6] In SPM experiments, the intrinsic absorption characteristics of hemoglobin are exploited to determine the hemoglobin mass and concentration. While SPM is robust, it is intrinsically limited to *ex vivo* quantification and offers only phase contrast. *In vivo* quantification is appealing as it requires no blood collection and could thus offer more dynamic monitoring. Nonlinear microscopy, such as stimulated Raman scattering (SRS) microscopy and transient absorption microscopy (TAM), provides an attractive route to achieving *in vivo* quantification. In SRS microscopy, the energy difference between two collinear laser pulses coherently excites an intrinsic vibrational mode of the molecule of interest in the sample. This capability has allowed researchers to study a host of biological processes *in vivo* including axon development[7,8] and lipid dynamics[9,10], among others. TAM is a multiphoton microscopy technique that is sensitive to numerous photophysical processes involving electronic excited states including, but not limited to two-photon absorption (TPA), excited state absorption (ESA), and ground state bleaching (GSB).[11] Similar to SPM, TAM makes use of the absorption characteristics of hemoglobin to gain intrinsic contrast, but with a significant advantage in that TAM is a three-dimensional imaging technique that allows imaging through scattering medium such as tissue.[12–19] Recently, we utilized the intrinsic differences between oxyhemoglobin and deoxyhemoglobin to achieve real-time quantification of oxygen saturation in RBCs.[18]

In this study, we quantify hemoglobin concentration at single RBC resolution by employing a multimodal multiphoton imaging approach and leveraging water as an internal standard. For most confocal and nonlinear optical microscopy techniques, quantification can be a challenge because of light scattering or aberration. Currently ratiometric fluorescence/Raman and fluorescence lifetime imaging are the only methods that can provide absolute quantification. Here we demonstrate a novel method of achieving hemoglobin quantification by using water as an internal standard to compensate for scattering and aberration induced intensity loss. Our method uses a novel orthogonal modulation scheme to simultaneously measure the vibrational signature of water with SRS microscopy and the transient absorption of hemoglobin with TAM. We posit that excitation volume and laser intensity is identical for water and hemoglobin in a RBC, which enables quantitative ratiometric imaging of hemoglobin. We test this hypothesis by calibrating our system to known concentrations of hemoglobin, quantifying RDW, MCV, and MCHC in freshly harvested mouse blood, and validating our measurements with traditional MCV and MCHC measurements. We further apply our calibrated microscope to observe the digestion of hemoglobin by *Plasmodium yoelii* (*P. yoelii*), a commonly used rodent malaria parasite, with single RBC resolution. We clearly see the dramatic decrease in hemoglobin concentration between infected RBCs and healthy RBCs. This work represents a major advancement for *in vitro* single RBC MCHC quantification and demonstrates a necessary step towards *in vivo* measurements.

2.2 METHODOLOGY

2.2.1 *Multimodal Multiphoton Microscope for Simultaneous SRS and TAM Imaging*

TAM and SRS experiments are both conducted using a pump-probe excitation scheme. Detection is based on the intensity change of the unmodulated beam using lock-in amplification and detection. It is important to note the difference in terminology between SRS and TAM. In SRS,

the pulses are termed: pump and Stokes; whereas TAM uses the terms: pump and probe. In this report, we use TAM terminology for simplicity. For SRS, the labelled “pump” and “probe” pulses are the Stokes and pump pulses, respectively. In SRS, a molecule is first pumped to an excited virtual state using a pump beam. Then the emission of a Stokes-shifted photon is stimulated using a Stokes beam of the same energy. For the wavelength pair used in these experiments, the predominate TAM processes were two-photon absorption (TPA) and excited state absorption (ESA). In these TAM processes, an electron is promoted to an excited state using a pump beam and excited to a higher excited state some delay later using a probe beam. The key difference between the two processes is that TPA proceeds through a virtual state, whereas ESA proceeds through a real electronic state. These concepts are illustrated in Figures 1.2 and 1.3 in Section 1.1.2 where the energy diagrams of SRS, TPA, and ESA are provided.

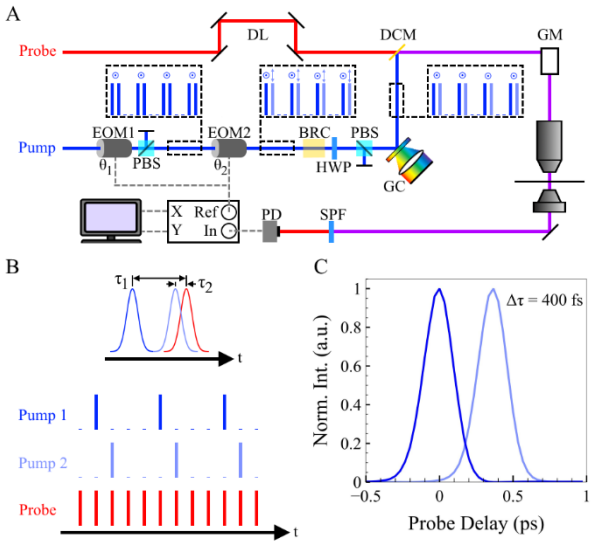

Figure 2.1. Experimental setup and principle. A) Diagram of the multiphoton microscope. DL: delay line. EOM: electro-optical modulator. PBS: polarizing beam splitter. BRC: birefringent crystal. HWP: half-wave plate. GC: grating based pulse stretcher/compressor. DCM: dichroic mirror. GM: scanning galvanomirrors. SPF: short-pass filter. PD: photodiode. B) Excitation scheme showing two orthogonal phase pump pulses and the probe pulse. C) SRS spectra of phosphate buffered saline showing temporal delay between orthogonal phase pump pulses. asdf

We take advantage of the difference in temporal profile between SRS, TPA, and ESA to measure both with a single detector. ESA involves electronic excited state with a long intermediate

lifetime (ps) which results in a long-lived temporal profile. In contrast, SRS and TPA are instantaneous with pulse overlap. Thus, we can selectively excite these processes simultaneously by acquiring two signals at two different interpulse delays (i.e., time delay between pump and probe) with a single detector and a lock-in amplifier. This is possible with an orthogonal modulation scheme that uses the X and Y output of the lock-in amplifier to detect two signals simultaneously.[20] We have previously demonstrated a similar approach for quantification of RBC oxygen saturation by using two temporally delayed pump pulse trains.[18] Here we developed a new modulation scheme that removes the needs for spatial separation and recombination of the two pump pulse trains (Figure 2.1A).

The experimental multimodal multiphoton microcopy system, shown in Figure 2.1A, is based upon a previously built transient absorption microscope.[18] Briefly, the laser system starts with a broadband femtosecond dual beam laser (Insight DeepSee+, Spectra-Physics) outputting two beams at 80 MHz (f_0) repetition rate. The pump beam (fixed at 1040 nm) was amplitude modulated at 20 MHz ($f_0/4$) by an electro-optical modulator (EOM1, θ_1) and a polarizing beam splitter (PBS). In our new modulation scheme, the amplitude modulated pulse train was followed by another polarization modulation at 20 MHz with a second EOM (EOM2, θ_2). The second EOM is operated 90 degrees phase shifted from the first EOM (i.e., $\theta_2 - \theta_1 = 90°$), resulting in two orthogonal phase pulse trains (s and p polarization). The resulting pulse trains are illustrated in Figures 2.1A and 2.1B. From here, the beam was passed through a 12 mm of birefringent quartz crystal (BRC) (Union Optic, BIF-Quartz). The difference in refractive index between the fast and slow axes of the crystal induced a temporal delay between the two polarizations. This temporal delay allows for simultaneous interrogation of two different pump-pulse delays. Next, the beam was sent through a half waveplate and polarizing beam splitter to combine both beams into a single

polarization. This collinear geometry not only simplifies the setup significantly, but also provides critical improvement in stability and quantification accuracy. The previously reported geometry[18,20] – the split path geometry – required very precise matching of size, divergence, dispersion, and spatial alignment between the two pump beams. This resulted in tedious alignment and a potential mismatch of beam foci. The collinear geometry does not suffer from these same optical hurtles.

To compensate for the dispersion caused by the EOMs, the pulses were compressed using a grating-based pulse compressor (GC).[21] The tunable probe beam, set to 765 nm for most of these experiments, was sent through a delay arm (DL) to temporally overlap with the orthogonal phase pump beams before all beams were spatially overlapped using a dichroic mirror (DCM) and directed through a scanning microscope and 40X objective (N40XLWD-NIR). The pump-probe excitation scheme is shown in Figure 2.1B. The two signals were detected by a dual-phase lock-in amplifier (Zurich Instrument) with orthogonal outputs after filtering out the two pump beams using a short pass filter (SPF). Two images were acquired simultaneously at a frame rate of 1 frame/sec for an image size of 512×512 pixels. We calculate the lateral PSF of our system to be ~300 nm and the axial PSF to be ~850 nm based on mathematical modeling of a high NA objective.[22] We measured the temporal delay between the two pump pulse trains to be 400 fs using the difference in peak SRS signal of phosphate buffered saline (Figure 2.1C).

2.2.2 *Whole Blood Collection and Hemoglobin Extraction*

Mouse blood was collected via cardiac puncture and treated with sodium heparin in compliance with University of Washington Institutional Animal Care and Use Committee (IACUC) standards. Complete blood count measurements of whole blood were conducted using a Hemavet 950 FS (Drew Scientific Group). For hemoglobin extraction, the blood was centrifuged at 1,000-g for 30

minutes. The supernatant and buffy coat were removed. The RBC pellet was rinsed with PBS, centrifuged at 1,000-g for 10 min, and the supernatant was removed. The rinsing process was repeated three times. Rinsed RBCs were mixed with methylene chloride at a ratio of 5:1 RBCs:CH_2Cl_2 to isolate high concentration hemoglobin.[23] The solution was centrifuged at 1,000-g for 10 minutes. The hemoglobin-rich supernatant was removed and filtered through 0.45 μm centrifuge filter to remove any residual cell debris. Hemoglobin concentration was measured using the cyanomethemoglobin method and an Agilent 8453A spectrophotometer. [24,25] For TAM/SRS imaging of RBCs, whole blood samples are used directly without any processing.

2.2.3 *Rodent Malaria Model Experiments*

All animal procedures were approved by the University of Washington IACUC. Briefly, BALB/cj mice were infected wild-type *P. yoelii* 17XNL parasites by intravenous retro-orbital injection of sporozoites. Blood stage parasitemia was monitored from three days post-infection by daily Giemsa-stained thin blood smears. Mice were euthanized using the CO_2 method, and *P. yoelii*-infected blood was collected via cardiac puncture. To prevent blood clotting, blood was treated with sodium heparin. Samples were diluted in complete medium comprised of RPMI HEPES (Gibco #22400) with 10% heat-inactivated fetal calf serum (Sigma #4135), supplemented with penicillin / streptomycin / L-glutamine (Gibco #10378-016). To preserve parasite viability, samples were maintained in a warm environment near 37°C until analysis.

2.3 Results and Discussion

The two main constituents of a RBC are water and hemoglobin.[26] By carefully tuning our laser system, we can simultaneously excite water with SRS and hemoglobin with TAM. This requires appropriate selection of the wavelength pair and optimization of the pulse duration for efficient excitation of both species. To start, we optimized the wavelength pair for SRS excitation of the OH stretching band. Several wavelengths were tested, and the spectra are shown in Figure 2.2. For reference, the spontaneous Raman spectrum is shown in Figure 2.3A. After examining multiple wavelengths, we targeted the center of the O-H stretching band (~3455 cm^{-1}) by using a pump/Stokes pair of 765 nm/1040 nm. Here, we employ transform limited femtosecond pulses to

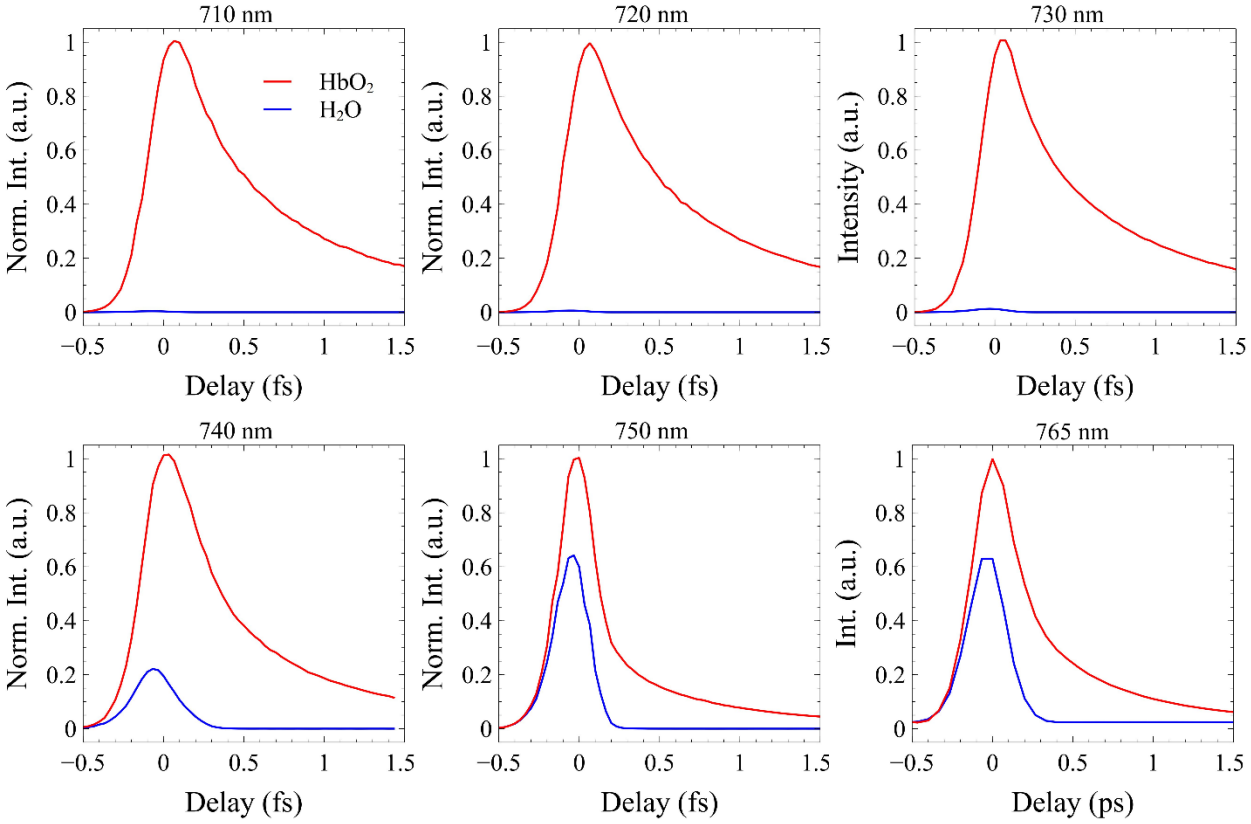

Figure 2.2. Wavelength survey for simultaneous excitation of hemoglobin (HbO_2) with TAM and water (H_2O) with SRS. Pump wavelength was 1040 nm for all traces shown.

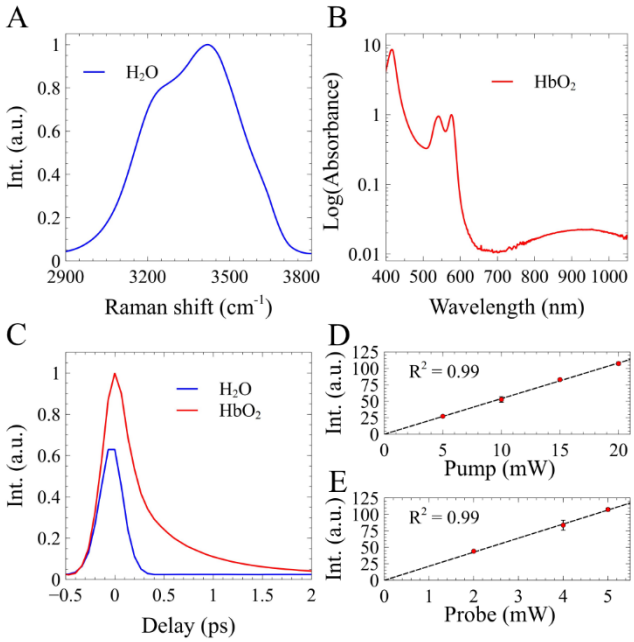

Figure 2.3. TAM/SRS optimization. A) Spontaneous Raman spectrum of water. B) UV/Vis spectrum of oxygenated hemoglobin (HbO_2). C) SRS spectrum of water (blue) and TAM spectrum of hemoglobin (red). D) Hemoglobin pump power dependence. E) Hemoglobin probe power dependence.

increase the SRS signal size as previously demonstrated.[27,28] Additionally, utilizing femtosecond pulses provides us with high temporal resolution for TAM. After confirming successful extraction of hemoglobin from blood (UV/Vis spectrum shown in Figure 2.3B), we measure the femtosecond SRS spectrum of water and the TAM spectrum hemoglobin (Figure 2.3C). It is important to note that we only consider the fully oxygenated form of hemoglobin, HbO_2. Hemoglobin is known to fully oxygenate under ambient lab conditions.[29] It is well documented that SRS signal scales linearly with excitation power, but TAM is more susceptible to higher order processes. To determine the excitation power dependence of hemoglobin, we measured the peak intensity of hemoglobin as a function of pump power (Figure 2.3D) and probe power (Figure 2.3E) at constant probe power of 20 mW and pump power of 5 mW, respectively. Here we see that hemoglobin scales linearly with pump and probe powers up to 20 mW pump power and 5 mW probe power. These powers were used for all measurements.

Next, we quantified the red blood cell distribution width (RDW) and mean cell volume (MCV) of mouse RBCs in whole blood. About 3 µL of freshly harvested mouse whole blood was placed on a glass microscope slide. A glass coverslip was gently laid on top of the blood droplet

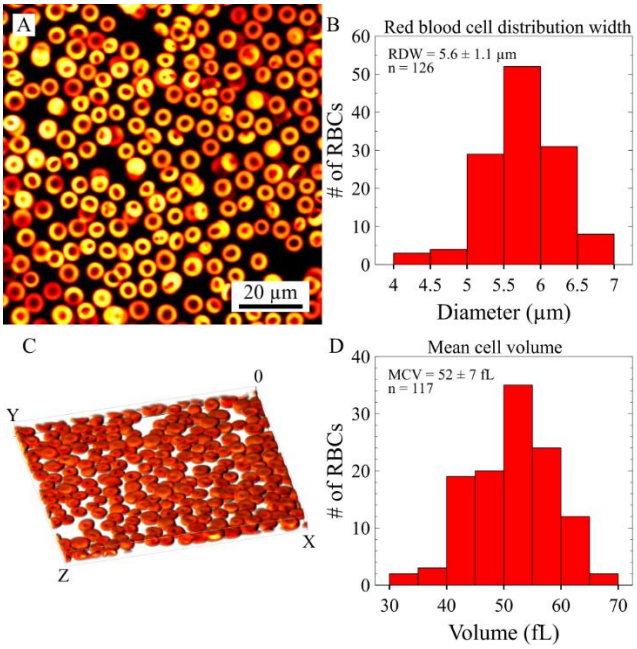

Figure 2.4. Quantification of red blood cell width and volume. A) Intensity image of freshly collected mouse blood. B) Histogram of red blood cell distribution width. C) Volume rendering of freshly collected mouse blood. D) Histogram of mean cell volume.

to disperse the RBCs into a monolayer. Figure 2.4A shows the resulting field of view (~100 × 100 µm) of RBCs. Mouse RBCs are anucleate discs with an average diameter of 4 to 7 µm.[4] Here the characteristic shape of the RBCs can be observed by the dimple in the center of the disc. The image is then segmented to locate individual RBCs. Segmenting involves removing low intensity pixels via intensity threshold and applying a watershed transform to separate closely spaced RBCs. The area of each was quantified, and the diameter was calculated by approximating each RBC as a circle (area = $\pi (d/2)^2$). The resulting histogram is shown in Figure 2.4B. We measured the RDW to be 5.6 ± 1.1 µm (n = 126 RBCs) which agrees well with literature.[4,30] Next, we quantified RBC MCV on a similar field of view. Figure 2.4C provides a volume rendering of the imaged RBCs. To quantify MCV, we apply a pixel intensity threshold to each RBC image stack between maximum intensity and half maximum intensity. The lower limit was set to capture pixels that lay on the outer surface of the RBC where the middle of the focal volume is centered on the RBC outer membrane. At this focal point the intensity will be roughly half of the maximum. With these threshold limits, we measured the MCV to be 52 ± 7 fL (n = 117 RBCs, reported in Figure 2.4D). To validate our

measurements, we performed a complete blood count of the same blood sample and measured the MCV to be 56.8 fL, which agrees well with our single cell measurements.

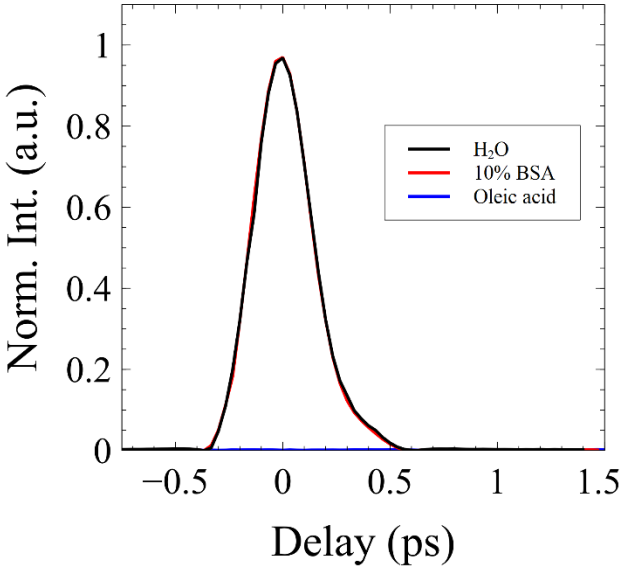

Figure 2.5. SRS spectra of water, 10% BSA and oleic acid excited at 765 nm/ 1040 nm.

Next, we measured the relationship between hemoglobin concentration and SRS/TAM signal. First, we confirm that the observed SRS signal is only dependent on water and not other cellular constituents. Figure 2.5 provides the SRS spectra of water, 10% BSA, and oleic acid. From these spectra, we see that the 10% BSA does not change the spectra. Oleic acid – a model lipid representing cell membrane – has no SRS signal at the employed wavelengths. Because typical non-hemoglobin protein concentration in RBC is less than 5% w/v and the concentration of other species such as saccharides are even lower (<1% w/v), we conclude that their contributions to SRS signal.[26,31] A series of hemoglobin solutions were made at varying concentrations and quantified using the cyanomethemoglobin method.[24,25] The same samples were then interrogated at two probe delays, τ = 0 fs and τ = 400 fs. These delays were chosen as they provide the highest intensity without causing interference between the two pump beams. Figure 2.6A shows the relationship between hemoglobin concentration and signal intensity at each pump-probe delay. As expected, signal intensity scales linearly with hemoglobin (Hb) concentration according to Equations 1 and 2:

$$S_1 = [H_2O] \times \sigma_{H_2O} + [Hb] \times \sigma_{1,Hb}$$

$$S_2 = [Hb] \times \sigma_{2,Hb}$$

where S_1 and S_2 are the intensities at each probe delay, $\tau = 0$ fs and $\tau = 400$ fs, respectively, $[H_2O]$ is the concentration of water, σ_{H2O} is the SRS signal from water, and $\sigma_{1,Hb}$ and $\sigma_{2,Hb}$ are the TAM signals of hemoglobin from each pump-probe delay. The ratio of the intensities is dependent on hemoglobin concentration, as expressed by Equation 3:

$$\frac{S_2}{S_1} = A + \frac{1}{B \times [Hb] + C}$$

Here, A, B, and C are fitting parameters determined based on least squares fitting shown in Figure 2.6B. With our system calibrated, we investigated MCHC in healthy RBCs. Figures 2.6C and 2.6D show a representative field of view of RBCs (~100 × 100 μm) at the two pump-probe delays, $\tau = 0$ fs and $\tau = 400$ fs, respectively. Figure 2.6E provides the MCHC map after applying

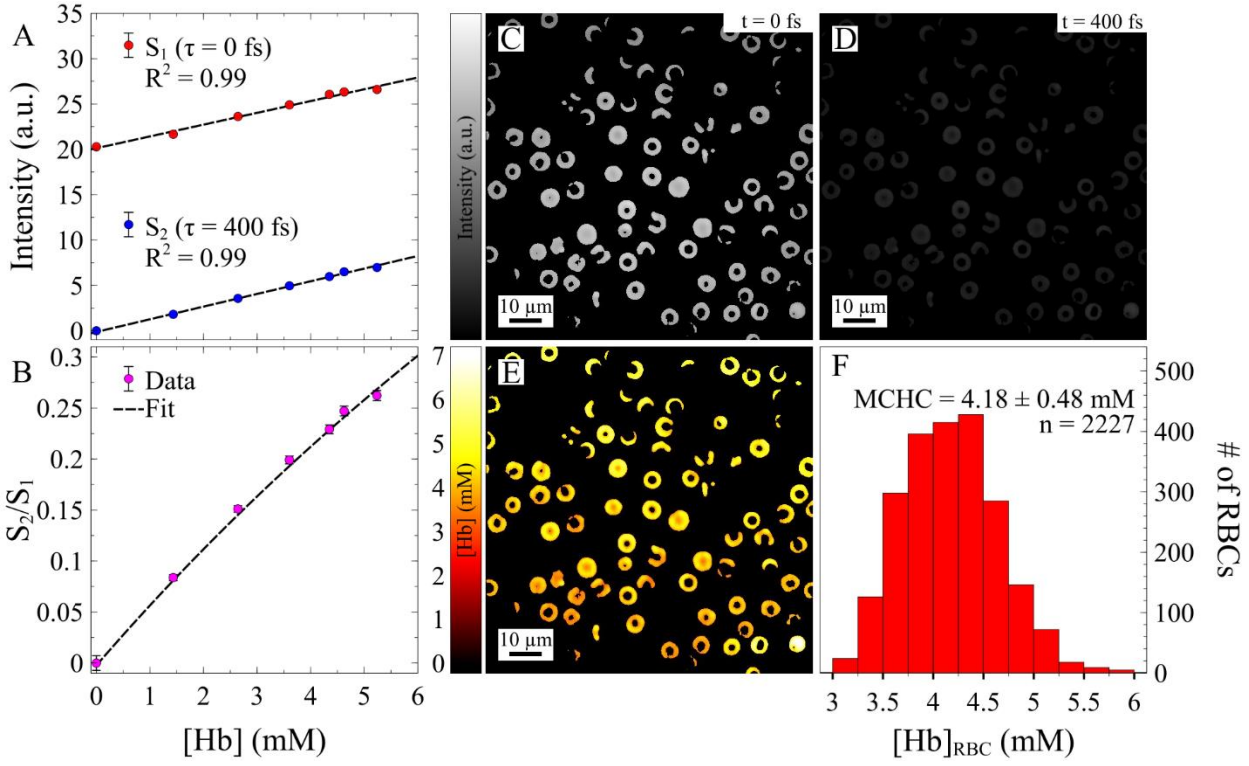

Figure 2.6. Quantification of hemoglobin concentration in healthy RBCs. A) Signal intensity increases with hemoglobin concentration. B) Ratiometric calibration of hemoglobin concentration. C, D) Intensity images of freshly collected mouse blood at two pump-probe delays. E) Hb concentration map of RBCs. F) Histogram of MCHC across 27 fields of view.

Eq. 3 to the ratio of Figures 2.6C and 2.6D. The MCHC, shown in Figure 2.6F, is 4.18 ± 0.48 mM (n = 2227) which agrees well with the MCHC quantified using CBC of the same blood sample (MCHC = 4.25 mM). These results substantiate our hypothesis that water can be used as an internal standard for hemoglobin concentration measurements. Additionally, with almost 100 RBCs in a field of view our method can image over 2000 RBCs in less than 30 seconds.

Finally, we applied our calibrated microscope to observe the digestion of hemoglobin by the rodent malaria parasite *P. yoelii*. We confirmed parasitemia via Giemsa-stained thin blood smears, see Figure 2.7. Figure 2.8A provides a representative field of view (~65 × 65 μm) of blood collected from an infected mouse. In this rodent malaria model, parasite infections are nonsynchronous; thus, there is a mixture of blood (intraerythrocytic) life stages present. The intraerythrocytic life stages can be broadly described as follows: first, a parasite in the merozoite stage invades a RBC and begins intraerythrocytic asexual reproduction, forming a so-called ring stage. Next, the parasite develops into the trophozoite stage, which is marked by the consumption of hemoglobin (Hb) by the parasite and subsequent deposition of hemozoin (Hzn), a residual crystalline heme byproduct.[32–35] Due to its crystalline structure, hemozoin has strong Raman intensity.[36,37] Finally, the parasite becomes a schizont, dividing to form merozoites that subsequently burst from the RBC to initiate the next round of infection. Because Hzn is such a prominent

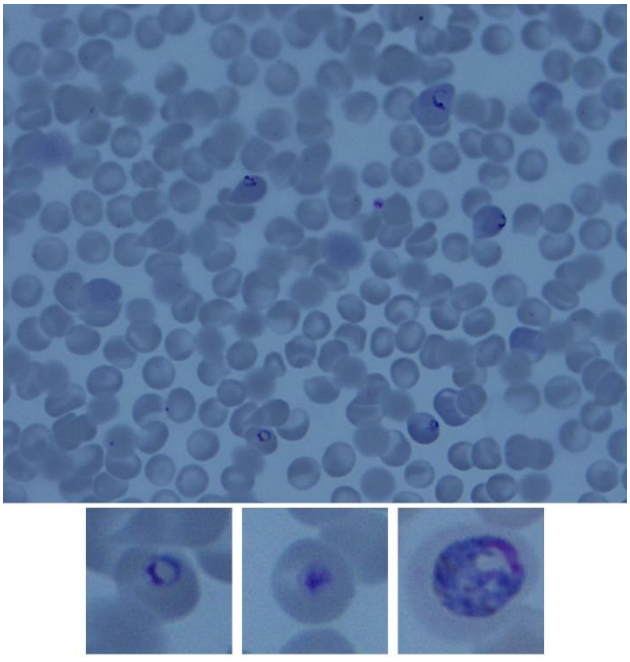

Figure 2.7. Giemsa-stained thin blood smears.

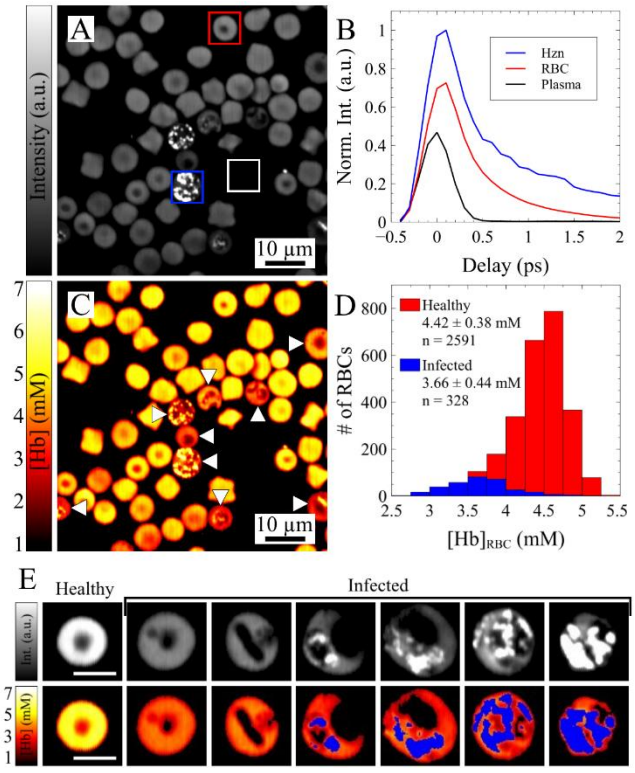

Figure 2.8. Quantification of hemoglobin concentration in whole mouse blood infected with Plasmodium yoelii. A) Intensity image of freshly collected infected mouse blood. B) Transient absorption spectra of hemoglobin (Hb) and hemozoin (Hzn). C) Hb concentration map with arrows denoting infected RBCs. D) Histogram of MCHC of healthy (red) and infected (blue) RBCs. E) Single cell comparison of healthy and infected RBCs. Hzn is separated based on intensity and color-coded blue. Scale bar is 5 µm.

feature of intraerythrocytic stages, it has become a simple metric for identifying parasite stage and maturation. Recently, it has been shown that transient absorption can distinguish between Hb and Hzn based on subtle differences in transient absorption lifetime.[38] We confirmed that the same differences between Hb and Hzn are present for the much longer wavelength pair used in our study. Figure 2.8B reports the SRS spectrum of blood plasma (white box) and the transient absorption lifetime of a healthy RBC (red box) and an infected RBC (blue box).

While monitoring the presence and production of Hzn can help identify parasite maturation, direct quantification of Hb concentration may offer a more meaningful measurement of intraerythrocytic parasite development. To determine MCHC, we first separated Hb and Hzn signals. As observed in Figure 2.8B, the signal of Hzn at $\tau = 0$ fs is about 30% higher than RBC signal which allows for intensity thresholding. After removing Hzn, the Hb concentration of the remaining cell was quantified. Figure 8C provides the Hb concentration map of Figure 2.8A. It is important to note

that Hzn signal was not removed in Figure 2.8C. Here, nine infected RBCs within the field of view are identified and denoted with an arrowhead. Differentiation between healthy and infected RBCs was achieved based on previously reported changes in morphology (i.e., ring shape, hemozoin production, etc.) in malaria parasite models.[32–34,39] The MCHC of healthy and infected RBCs (n = 2919) were quantified to be 4.42 ± 0.38 mM (n = 2591) and 3.66 ± 0.44 mM (n = 328), respectively (see Figure 2.8D). We believe that the increased standard deviation in infected RBCs is due to asynchronous parasite maturation in this model. This claim is substantiated by the clear difference in MCHC and morphology between healthy and infected RBCs shown in Figure 2.8E. Since many antimalarial agents target the hemoglobin digestion pathway of parasite maturation,[40,41] our technique offers a previously unmet need of dynamic MCHC quantification at single RBC resolution.

2.4 CONCLUSION

Current methods for quantifying MCHC rely on bulk analysis which may not fully characterize a blood sample. Instead, single RBC analysis would provide the necessary insight into cell-to-cell heterogeneity that exists in blood disorder and disease pathologies and allow for screening of minor population cells. Moreover, understanding oxygen transport as affected by MCHC would provide crucial insight into whole body homeostasis during pathologies that impact the blood compartment. We have demonstrated the development of a novel multimodal multiphoton imaging platform that leverages water as an internal standard for quantification of hemoglobin concentration at single RBC resolution. By collecting two images simultaneously, we were able to vibrationally excite water with SRS and electronically excite hemoglobin with TAM. A simple ratiometric analysis with two different molecular contrasts enables direct quantification of hemoglobin concentration inside RBC. We note that this internal calibration approach is not only

applicable to hemoglobin measurements, but also can be generalized to other nonlinear optical signals including SRS and two-photon fluorescence. It addresses a major unmet need in absolute concentration quantification due to scattering and aberration induced intensity loss.

Our multimodal imaging approach provides a range of measurements that allow comprehensive characterization of RBC related parameters at single RBC resolution. We used this approach to quantify RDW, MCV, and MCHC in healthy RBCs. We further demonstrated the utility and sensitivity of our technique by quantifying the difference in MCHC between healthy RBCs and *P. yoelii* infected RBCs. Moreover, we present infected RBCs at a variety of states throughout the parasite's asexual reproduction. This work is well suited for *in vitro* monitoring of hemoglobin digestion which will allow for dynamic monitoring of parasite maturation. Only minute amount of blood (<1 μL) is needed for characterization due to the sensitivity of single RBC analysis. To this end, we believe that this technique will offer great utility to antimalarial drug discovery and development. Additionally, this advancement is crucial towards developing an *in vivo* methodology of monitoring MCHC. A major hurdle for *in vivo* translation will be the dynamic oxygen saturation of hemoglobin which is known to alter the transient absorption kinetics. Thus, a more elaborate calibration that accounts for the oxygen saturation level of hemoglobin is needed. To apply such a calibration to *in vivo* measurements, it is also necessary to measure the oxygenation state of the blood vessel with another techniques, such as ratiometric TAM or intrinsic optical imaging.[42] Until then, this work demonstrates the ability to quantify important pathological metrics (i.e., RDW, MCV, and MCHC) with 10-100-fold less volume than traditional cell counting methods. This benefit will allow for more dynamic monitoring of animal wellbeing and health during disease model studies.

2.5 REFERENCES

(1) Barlas Raphae S.; Honney Katie; Loke Yoon K.; McCall Stephen J.; Bettencourt-Silva Joao H.; Clark Allan B.; Bowles Kristian M.; Metcalf Anthony K.; Mamas Mamas A.; Potter John F.; Myint Phyo K. Impact of Hemoglobin Levels and Anemia on Mortality in Acute Stroke: Analysis of UK Regional Registry Data, Systematic Review, and Meta-Analysis. *Journal of the American Heart Association 5* (8), e003019. https://doi.org/10.1161/JAHA.115.003019.
(2) Milner, D. A. Malaria Pathogenesis. *Cold Spring Harb Perspect Med* **2018**, *8* (1). https://doi.org/10.1101/cshperspect.a025569.
(3) Parasuraman, S.; Raveendran, R.; Kesavan, R. Blood Sample Collection in Small Laboratory Animals. *J Pharmacol Pharmacother* **2010**, *1* (2), 87–93. https://doi.org/10.4103/0976-500X.72350.
(4) O'Connell, K. E.; Mikkola, A. M.; Stepanek, A. M.; Vernet, A.; Hall, C. D.; Sun, C. C.; Yildirim, E.; Staropoli, J. F.; Lee, J. T.; Brown, D. E. Practical Murine Hematopathology: A Comparative Review and Implications for Research. *Comp Med* **2015**, *65* (2), 96–113.
(5) Park, Y.; Yamauchi, T.; Choi, W.; Dasari, R.; Feld, M. S. Spectroscopic Phase Microscopy for Quantifying Hemoglobin Concentrations in Intact Red Blood Cells. *Opt. Lett., OL* **2009**, *34* (23), 3668–3670. https://doi.org/10.1364/OL.34.003668.
(6) Jang, Y.; Jang, J.; Park, Y. Dynamic Spectroscopic Phase Microscopy for Quantifying Hemoglobin Concentration and Dynamic Membrane Fluctuation in Red Blood Cells. *Opt. Express, OE* **2012**, *20* (9), 9673–9681. https://doi.org/10.1364/OE.20.009673.
(7) Hu, C.-R.; Zhang, D.; Slipchenko, M. N.; Cheng, J.-X.; Hu, B. Label-Free Real-Time Imaging of Myelination in the Xenopus Laevis Tadpole by in Vivo Stimulated Raman Scattering Microscopy. *J Biomed Opt* **2014**, *19* (8). https://doi.org/10.1117/1.JBO.19.8.086005.
(8) Tian, F.; Yang, W.; Mordes, D. A.; Wang, J.-Y.; Salameh, J. S.; Mok, J.; Chew, J.; Sharma, A.; Leno-Duran, E.; Suzuki-Uematsu, S.; Suzuki, N.; Han, S. S.; Lu, F.-K.; Ji, M.; Zhang, R.; Liu, Y.; Strominger, J.; Shneider, N. A.; Petrucelli, L.; Xie, X. S.; Eggan, K. Monitoring Peripheral Nerve Degeneration in ALS by Label-Free Stimulated Raman Scattering Imaging. *Nat Commun* **2016**, *7* (1), 13283. https://doi.org/10.1038/ncomms13283.
(9) Shi, L.; Zheng, C.; Shen, Y.; Chen, Z.; Silveira, E. S.; Zhang, L.; Wei, M.; Liu, C.; de Sena-Tomas, C.; Targoff, K.; Min, W. Optical Imaging of Metabolic Dynamics in Animals. *Nat Commun* **2018**, *9*. https://doi.org/10.1038/s41467-018-05401-3.
(10) Li, X.; Li, Y.; Jiang, M.; Wu, W.; He, S.; Chen, C.; Qin, Z.; Tang, B. Z.; Mak, H. Y.; Qu, J. Y. Quantitative Imaging of Lipid Synthesis and Lipolysis Dynamics in Caenorhabditis Elegans by Stimulated Raman Scattering Microscopy. *Anal. Chem.* **2019**, *91* (3), 2279–2287. https://doi.org/10.1021/acs.analchem.8b04875.
(11) Ye, T.; Fu, D.; Warren, W. S. Nonlinear Absorption Microscopy†. *Photochemistry and Photobiology* **2009**, *85* (3), 631–645. https://doi.org/10.1111/j.1751-1097.2008.00514.x.
(12) Chen, A. J.; Yuan, X.; Li, J.; Dong, P.; Hamza, I.; Cheng, J.-X. Label-Free Imaging of Heme Dynamics in Living Organisms by Transient Absorption Microscopy. *Anal. Chem.* **2018**, *90* (5), 3395–3401. https://doi.org/10.1021/acs.analchem.7b05046.
(13) Chen, T.; Huang, Y. Label-Free Transient Absorption Microscopy for Red Blood Cell Flow Velocity Measurement in Vivo. *Anal. Chem.* **2017**, *89* (19), 10120–10123. https://doi.org/10.1021/acs.analchem.7b01952.
(14) Zhang, L.; Zou, X.; Zhang, B.; Cui, L.; Zhang, J.; Mao, Y.; Chen, L.; Ji, M. Label-Free Imaging of Hemoglobin Degradation and Hemosiderin Formation in Brain Tissues with Femtosecond Pump-Probe Microscopy. *Theranostics* **2018**, *8* (15), 4129–4140. https://doi.org/10.7150/thno.26946.

(15) Fu, D.; Ye, T.; Matthews, T. E.; Chen, B. J.; Yurtserver, G.; Warren, W. S. High-Resolution *in Vivo* Imaging of Blood Vessels without Labeling. *Opt. Lett., OL* **2007**, *32* (18), 2641–2643. https://doi.org/10.1364/OL.32.002641.
(16) Fu, D.; Matthews, T. E.; Ye, T.; Piletic, I. R.; Warren, W. S. Label-Free in Vivo Optical Imaging of Microvasculature and Oxygenation Level. *J Biomed Opt* **2008**, *13* (4), 040503. https://doi.org/10.1117/1.2968260.
(17) Fu, D. *Developing Novel Nonlinear Optical Contrast for Biomedical Imaging*; Princeton University, Series Ed.; 2009, 2009.
(18) Francis, A. T.; Berry, K.; Thomas, E. C.; Hill, A. H.; Fu, D. In Vitro Quantification of Single Red Blood Cell Oxygen Saturation by Femtosecond Transient Absorption Microscopy. *J. Phys. Chem. Lett.* **2019**, 3312–3317. https://doi.org/10.1021/acs.jpclett.9b01116.
(19) Dong, P.-T.; Lin, H.; Huang, K.-C.; Cheng, J.-X. Label-Free Quantitation of Glycated Hemoglobin in Single Red Blood Cells by Transient Absorption Microscopy and Phasor Analysis. *Science Advances* **2019**, *5* (5), eaav0561. https://doi.org/10.1126/sciadv.aav0561.
(20) He, R.; Xu, Y.; Zhang, L.; Ma, S.; Wang, X.; Ye, D.; Ji, M. Dual-Phase Stimulated Raman Scattering Microscopy for Real-Time Two-Color Imaging. *Optica, OPTICA* **2017**, *4* (1), 44–47. https://doi.org/10.1364/OPTICA.4.000044.
(21) Lai, M.; Lai, S. T.; Swinger, C. Single-Grating Laser Pulse Stretcher and Compressor. *Appl. Opt., AO* **1994**, *33* (30), 6985–6987. https://doi.org/10.1364/AO.33.006985.
(22) Richards, B.; Wolf, E.; Gabor, D. Electromagnetic Diffraction in Optical Systems, II. Structure of the Image Field in an Aplanatic System. *Proceedings of the Royal Society of London. Series A. Mathematical and Physical Sciences* **1959**, *253* (1274), 358–379. https://doi.org/10.1098/rspa.1959.0200.
(23) Sakai, H.; Takeoka, S.; Yokohama, H.; Seino, Y.; Nishide, H.; Tsuchida, E. Purification of Concentrated Hemoglobin Using Organic Solvent and Heat Treatment. *Protein Expression and Purification* **1993**, *4* (6), 563–569. https://doi.org/10.1006/prep.1993.1074.
(24) Zijlstra, W. G. Standardisation of Haemoglobinometry: History and New Challenges. *Comparative Haematology International* **1997**, *7* (3), 125–132. https://doi.org/10.1007/BF02652590.
(25) Meng, F.; Alayash, A. I. Determination of Extinction Coefficients of Human Hemoglobin in Various Redox States. *Anal Biochem* **2017**, *521*, 11–19. https://doi.org/10.1016/j.ab.2017.01.002.
(26) Weed, R. I.; Reed, C. F.; Berg, G. IS HEMOGLOBIN AN ESSENTIAL STRUCTURAL COMPONENT OF HUMAN ERYTHROCYTE MEMBRANES?*. *J Clin Invest* **1963**, *42* (4), 581–588.
(27) Zhang, D.; Slipchenko, M. N.; Cheng, J.-X. Highly Sensitive Vibrational Imaging by Femtosecond Pulse Stimulated Raman Loss. *J. Phys. Chem. Lett.* **2011**, *2* (11), 1248–1253. https://doi.org/10.1021/jz200516n.
(28) Francis, A.; Berry, K.; Chen, Y.; Figueroa, B.; Fu, D. Label-Free Pathology by Spectrally Sliced Femtosecond Stimulated Raman Scattering (SRS) Microscopy. *PLOS ONE* **2017**, *12* (5), e0178750. https://doi.org/10.1371/journal.pone.0178750.
(29) Liu, P.; Zhu, Z.; Zeng, C.; Nie, G. Specific Absorption Spectra of Hemoglobin at Different PO2 Levels: Potential Noninvasive Method to Detect PO2 in Tissues. *J Biomed Opt* **2012**, *17* (12), 125002. https://doi.org/10.1117/1.JBO.17.12.125002.

(30) FUKUDA, T.; ASOU, E.; NOGI, K.; GOTO, K. Evaluation of Mouse Red Blood Cell and Platelet Counting with an Automated Hematology Analyzer. *J Vet Med Sci* **2017**, *79* (10), 1707–1711. https://doi.org/10.1292/jvms.17-0387.
(31) Togashi, Y.; Shirakawa, J.; Okuyama, T.; Yamazaki, S.; Kyohara, M.; Miyazawa, A.; Suzuki, T.; Hamada, M.; Terauchi, Y. Evaluation of the Appropriateness of Using Glucometers for Measuring the Blood Glucose Levels in Mice. *Sci Rep* **2016**, *6*. https://doi.org/10.1038/srep25465.
(32) Yahata, K.; Treeck, M.; Culleton, R.; Gilberger, T.-W.; Kaneko, O. Time-Lapse Imaging of Red Blood Cell Invasion by the Rodent Malaria Parasite Plasmodium Yoelii. *PLOS ONE* **2012**, *7* (12), e50780. https://doi.org/10.1371/journal.pone.0050780.
(33) Rinehart, M. T.; Park, H. S.; Walzer, K. A.; Chi, J.-T. A.; Wax, A. Hemoglobin Consumption by P. Falciparum in Individual Erythrocytes Imaged via Quantitative Phase Spectroscopy. *Sci Rep* **2016**, *6*. https://doi.org/10.1038/srep24461.
(34) Grüring, C.; Spielmann, T. Chapter Five - Imaging of Live Malaria Blood Stage Parasites. In *Methods in Enzymology*; Conn, P. M., Ed.; Imaging and Spectroscopic Analysis of Living Cells; Academic Press, 2012; Vol. 506, pp 81–92. https://doi.org/10.1016/B978-0-12-391856-7.00029-9.
(35) Burnett, J. L.; Carns, J. L.; Richards-Kortum, R. In Vivo Microscopy of Hemozoin: Towards a Needle Free Diagnostic for Malaria. *Biomed Opt Express* **2015**, *6* (9), 3462–3474. https://doi.org/10.1364/BOE.6.003462.
(36) Wood, B. R.; Langford, S. J.; Cooke, B. M.; Glenister, F. K.; Lim, J.; McNaughton, D. Raman Imaging of Hemozoin within the Food Vacuole of Plasmodium Falciparum Trophozoites. *FEBS Letters* **2003**, *554* (3), 247–252. https://doi.org/10.1016/S0014-5793(03)00975-X.
(37) Frosch, T.; Koncarevic, S.; Zedler, L.; Schmitt, M.; Schenzel, K.; Becker, K.; Popp, J. In Situ Localization and Structural Analysis of the Malaria Pigment Hemozoin. *J. Phys. Chem. B* **2007**, *111* (37), 11047–11056. https://doi.org/10.1021/jp071788b.
(38) Chen, A. J.; Huang, K.-C.; Bopp, S.; Summers, R.; Dong, P.; Huang, Y.; Zong, C.; Wirth, D.; Cheng, J.-X. Quantitative Imaging of Intraerythrocytic Hemozoin by Transient Absorption Microscopy. *JBO* **2019**, *25* (1), 014507. https://doi.org/10.1117/1.JBO.25.1.014507.
(39) Lee, A. H.; Symington, L. S.; Fidock, D. A. DNA Repair Mechanisms and Their Biological Roles in the Malaria Parasite Plasmodium Falciparum. *Microbiol. Mol. Biol. Rev.* **2014**, *78* (3), 469–486. https://doi.org/10.1128/MMBR.00059-13.
(40) Klonis, N.; Crespo-Ortiz, M. P.; Bottova, I.; Abu-Bakar, N.; Kenny, S.; Rosenthal, P. J.; Tilley, L. Artemisinin Activity against Plasmodium Falciparum Requires Hemoglobin Uptake and Digestion. *PNAS* **2011**, *108* (28), 11405–11410. https://doi.org/10.1073/pnas.1104063108.
(41) Herraiz, T.; Guillén, H.; González-Peña, D.; Arán, V. J. Antimalarial Quinoline Drugs Inhibit β-Hematin and Increase Free Hemin Catalyzing Peroxidative Reactions and Inhibition of Cysteine Proteases. *Sci Rep* **2019**, *9* (1), 1–16. https://doi.org/10.1038/s41598-019-51604-z.
(42) Bouchard, M. B.; Chen, B. R.; Burgess, S. A.; Hillman, E. M. C. Ultra-Fast Multispectral Optical Imaging of Cortical Oxygenation, Blood Flow, and Intracellular Calcium Dynamics. *Opt Express* **2009**, *17* (18), 15670–15678.

Chapter 3. *IN VITRO* QUANTIFICATION OF SINGLE RED BLOOD CELL OXYGEN SATURATION BY FEMTOSECOND TRANSIENT ABSORPTION MICROSCOPY

3.1 INTRODUCTION

Hemodynamics (the dynamics of blood flow) play a vital role in maintaining energy homeostasis throughout the body. Among many functions, circulating blood provides the basic building blocks – such as glucose and oxygen – needed for cells to survive. Hemoglobin, a major cytoplasmic constituent of red blood cells (RBCs), is responsible for nearly all oxygen transport in the body via reversible oxygen binding. The protein structure is made up of four subunits, each containing a heme group and a globular protein. This structure enables each hemoglobin molecule to bind up to four oxygen molecules.[1] Oxygen saturation (sO_2), the ratio of oxygenated hemoglobin (HbO_2) to total hemoglobin (comprised of HbO_2 and deoxygenated hemoglobin, Hb), is tightly regulated by the body and often changes quickly in response to bodily events. Monitoring changes in sO_2 is critically important in understanding such regulation and consequences in dysregulation in diseases such as anemia or sepsis. [2] One such tool is functional magnetic resonance imaging (fMRI), wherein changes in blood flow and oxygenation are determined based on the unique paramagnetic property of deoxyhemoglobin. fMRI is widely used for functional imaging of the brain.[3,4] While monitoring millimeter scale changes in sO_2 is insightful and allows for global imaging of brain activity, understanding hemodynamics at high spatial resolution (single-RBC level) is crucial for studying local oxygen transport and consumption in heterogeneous tissue.

Intense research efforts have focused on imaging blood and tissue oxygenation at finer spatial resolution.[5,6] Largely, these efforts have been directed towards tumor and neuroscience studies where high resolution sO_2 measurements provide invaluable information on tissue function, growth, and metabolism.[7–9] However, most current technologies rely on wavelength-dependent linear absorption of hemoglobin, which has inherent limitations in tissue imaging due to scattering. Tissue scattering not only decreases spatial resolution but also complicates sO_2 quantification because scattering is also wavelength dependent.[7,10–14] Two-photon phosphorescence lifetime microscopy (2PLM) is an imaging technique that circumvents these limitations by quantifying partial pressure of O_2, or pO_2, via the quenching of phosphorescence of an exogenous agent in the presence of molecular oxygen in either RBCs or tissue.[15–18] Due to the two-photon confinement effect, it offers submicron spatial resolution. While the performance of 2PLM probes has been optimized in recent years to allow for faster measurement and higher signal-to-noise ratio (SNR), 2PLM remains intrinsically limited by long phosphorescence lifetimes to discrete point measurements (typical pixel dwell time > 10 ms) instead of full field high resolution imaging. Additionally, it has the disadvantage of requiring repeated invasive injections of expensive reagents due to fast circulation clearance time.[19]

Transient absorption microscopy (TAM) is a promising label-free alternative to 2PLM for hemoglobin imaging.[20–25] TAM is a multiphoton imaging technique that is sensitive to numerous photophysical processes; these processes constitute the transient lifetime kinetics of a molecule or system. Recent demonstrations have identified that the transient lifetime kinetics of hemoglobin at near-IR wavelengths are largely based on three main processes: two-photon absorption (TPA), excited state absorption (ESA), and ground state bleaching (GSB).[20,21,24] In one such demonstration, Fu et al. distinguished between HbO_2 and Hb by identifying key differences

between the their transient absorption spectral differences.[20,21] However, real-time quantification of sO_2 was not possible due to the need to perform sequential measurements. In this work, we present the first demonstration of real-time *in vitro* TAM for quantification of sO_2 in whole blood. We achieve this via simultaneous collection of two points along the transient decay curve that exploit differences in the transient lifetime kinetics between HbO_2 and Hb. In doing so, we avoid the wavelength dependent light scattering problem of other absorption based sO_2 measurement techniques. This advancement is pivotal in developing a label-free, real-time sO_2 imaging modality suitable for *in vitro* and *in vivo* applications.

3.2 METHODOLOGY

3.2.1 *Experimental Set Up*

The experimental pump-probe TAM system used for ratiometric imaging is shown in Figure 3.1A. Briefly, the pump beam (fixed at 1040 nm) was modulated at 20 MHz by an electro-optical modulator and separated into two amplitude modulated pulse trains (P1 and P2) that are 180° out of phase using a polarizing beam splitter. P2 is delayed by one pulse, or 12.5 ns (1/80 MHz), to shift the two pulse trains to 90° out of phase before being recombined using a 50:50 beam splitter. The pulses are temporally compressed using a grating-based pulse compressor.[26] Rhodamine 6G was used to optimize each wavelength for shortest pulse duration (Figure 3.2). This resulting pulse trains are illustrated in Figure 3.1B. To avoid interference between the two pump arms, precise temporal control over P2 is achieved using a delay line. Empirically, a separation between the two

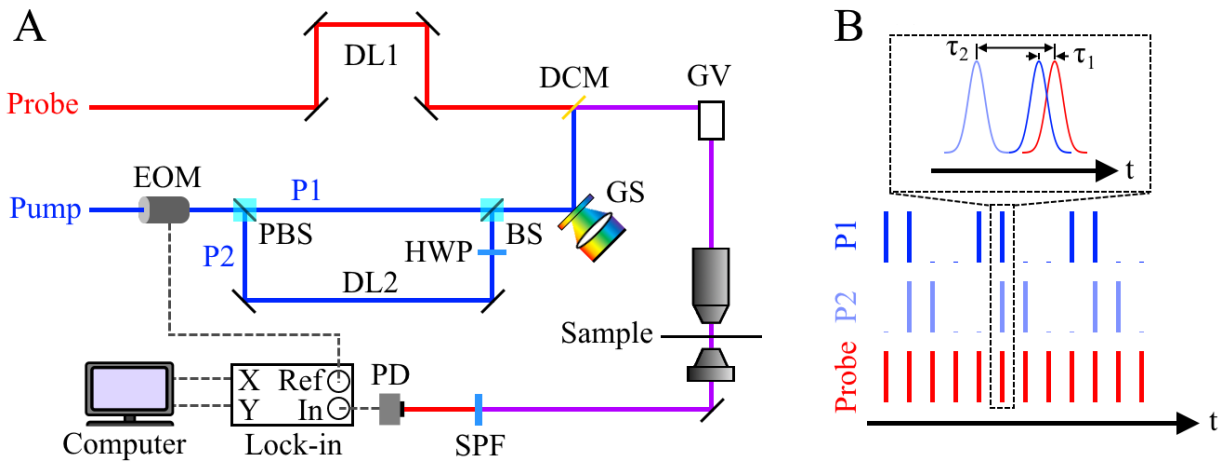

Figure 3.1. Experimental design for dual channel TAM. A) Diagram of TAM microscope. EOM: electro-optical modulator, P1 and P2: pump pulse train 1 and 2, PBS: polarizing beam splitter, BS: beam splitter, DL: delay line, GS: grating based pulse stretcher, DCM: dichroic mirror, GV: scanning galvanomirrors, SPF: short-pass filter, PD: photodiode. B) Pulse trains at the sample. P1 and P2 are 90° out of phase with each other; precise control of pump/probe delay, τ, is achieved with delay lines (DL1 and DL2).

pump beams of ~700 fs showed no interference. The probe beam (tunable from 680 nm – 1300 nm) was sent through a delay arm to temporally overlap with the two pump beams before all beams are spatially overlapped using a dichroic mirror and directed through a scanning microscope. The two TAM signals were detected by a dual-phase lock-in amplifier (Zurich Instrument) with orthogonal outputs after filtering out the two pump beams using a short pass filter. Two images at two different pump-probe delays are acquired simultaneously at a frame rate of 1 frame/sec for an image size of 512×512 pixels. A related two-channel detection scheme has been used for stimulated Raman scattering (SRS) imaging of tissue.[27,28]

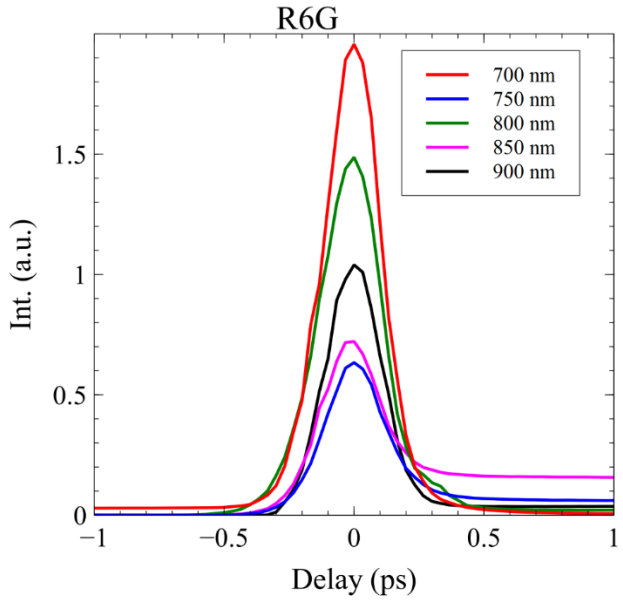

Figure 3.2. Rhodamine 6G spectra at the various probe wavelengths.

3.2.2 *Hemoglobin Extraction*

Hemoglobin was extracted from freshly harvested bovine blood (purchased from Lampire). Whole blood aliquots were centrifuged at 1000-g for 10 min at 22 °C. The supernatant and buffy coat were removed, leaving only red blood cells (RBCs).[29] The RBCs were then suspended in DI water and frozen for storage at -20 °C. After freezing, the solution was thawed and diluted by a factor of 2 with DI water. The resulting solution was then vortexed and centrifuged at 1,200-g for 20 min at 22 °C to lyse the remaining RBCs and remove cellular debris, respectively. The hemoglobin solution was then filtered using a 0.45 µm syringe filter to remove any remaining cellular debris.

3.2.3 *Oxygen Saturation Calibration*

The extracted hemoglobin was fully deoxygenated through exposure to 1.7 mL/min N_2 for ~2 hour. The solution was slowly oxygenated from exposure to ambient air under constant stirring for 10 minutes. Samples were taken periodically and sealed in custom made airtight cuvettes to prevent further oxygenation. The cuvettes were made by sandwiching solution between a glass slide and cover glass with double sided tape as a spacer. Commercial nail polish was used to seal the cuvette. The exact hemoglobin oxygenation of each sample was determined by non-negative least squared fitting of collected UV/Vis spectra with standard UV/Vis spectra of HbO_2 and Hb.

3.3 Results and Discussion

The three main processes present in hemoglobin TAM are two-photon absorption (TPA), excited state absorption (ESA), and ground state bleaching (GSB).[20,21,24] The contributions of each to the overall transient state kinetics are largely dependent on the pump and probe wavelengths. Accurate differentiation of HbO_2 and Hb requires both high signal intensity as well as appreciable difference between the transient dynamics of HbO_2 and Hb at the chosen pump-probe wavelengths. Hemoglobin was extracted from fresh bovine blood; Hb was prepared through exposure of extracted hemoglobin to a pure N_2 environment for ~1 hour under constant stirring. The UV/Vis spectra of HbO_2 and Hb, as shown in Figure 3.3A, agree well with literature spectra.[30,31] We compared the transient decay curves of HbO_2 and Hb using a single pump beam (P1) at 1040 nm and five different probe wavelengths: 700 nm, 750 nm, 800 nm, 850 nm, and 900 nm. Hemoglobin first undergoes one-photon absorption with the pump beam as indicated by the linearity between signal intensity and pump power in Figure 3.4. Next, the excited state hemoglobin is excited by the probe beam. Figures 3.3B-3.3F show the spectra of HbO_2 and Hb probed at each of the tested

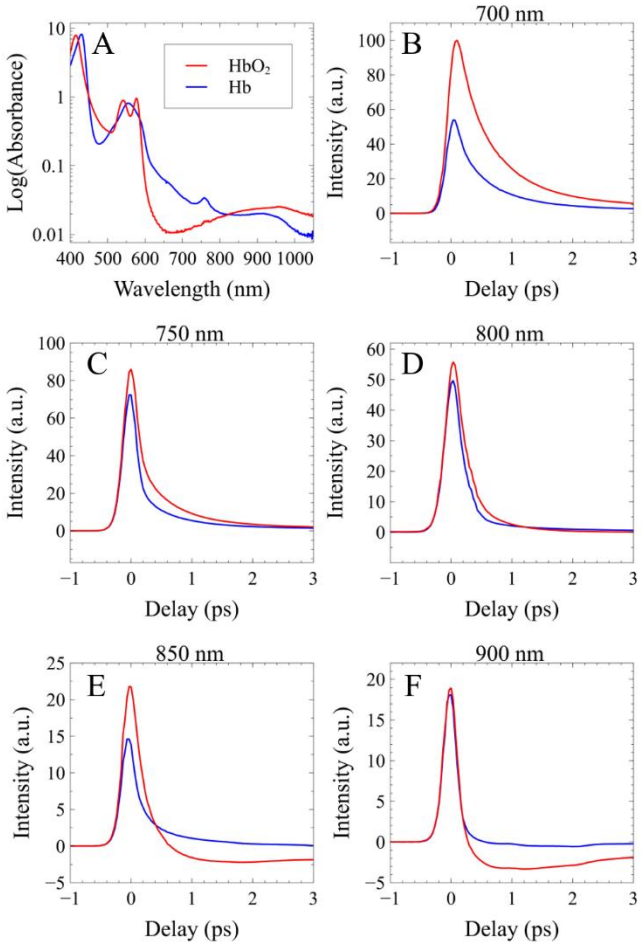

Figure 3.3. Wavelength-dependent transient lifetime kinetics. A) UV/Vis spectra of oxygenated bovine hemoglobin (HbO_2, red) and deoxygenated bovine hemoglobin (Hb, blue). B-F) Transient absorption curves of HbO_2 and Hb at probe wavelengths of 700 nm, 750 nm, 800 nm, 850 nm, and 900 nm.

wavelengths. All scans were collected with 30 mW of pump power and 8 mW of probe power at the focus and normalized to the intensity of HbO_2 probed at 700 nm allowing for side-by-side comparison of signal intensities. Upon inspection, 700 nm probe offers a large difference between the two species and the highest signal of all probe wavelengths tested (Figure 3.3B). Here, the two most prevalent processes are TPA and ESA. TPA is the simultaneous absorption of two photons, resulting in a strong, narrow peak centered near $\tau = 0$ fs. ESA reflects the absorption of probe photons by photoexcited molecules and is likely the chief contributor to the transient decay from 0 ps to 3 ps.[20,21] The transient decay kinetics of HbO_2 and Hb are very similar when probed with 750 nm (Figure 3.3C) and 800 nm (Figure 3.3D) suggesting that both wavelengths are poor choices to differentiate the two species. The similar decay observed at these probe wavelengths is likely due to strong contribution from stimulated Raman scattering (SRS) of water at 750 nm[32] and the CH bonds present in the hemoglobin molecule at 800 nm.[28,33] Probe wavelengths of 850 nm and 900 nm show negative signal at delays

longer than 500 fs. We believe that this is due to GSB which results in long-lived negative signal as previously reported for hemoglobin TAM.[24] Importantly, GSB is only present in the HbO_2 decay curve. Thus, it could serve well to distinguish between the two species. However, the signal intensity of hemoglobin is substantially lower at a probe wavelength of 900 nm (~5 fold lower compared to 700 nm) making it a less ideal wavelength for our experiments. We chose to use a probe wavelength of 700 nm as it offers the strongest signal of the tested wavelengths as well as relatively large differences between the transient decay kinetics of two species.

Additionally, we observed a subtle power dependence in the transient lifetime kinetics. While the overall shape of the curve (i.e., presence of TPA, ESA, or GSB) did not change substantially at various excitation powers, the quantitative capabilities of the technique would be lessened from power dependent kinetics. To ensure accurate quantification at a probe wavelength of 700 nm, we compared the transient lifetime kinetics of HbO_2 at varying pump/probe powers and determined the powers below which kinetics are power independent (Figure 3.4). The kinetics are largely pump power (λ = 1040 nm) independent. The probe power (λ = 700 nm) had a stronger effect on the kinetics. We observed that probe powers above 3 mW caused a subtle change in transient absorption kinetics that would hinder quantitative measurements. All pump/probe power experiments were performed in triplicate to ensure reproducibility. For all sO_2 quantification, excitation powers were kept at 20 mW pump power and 3 mW probe power.

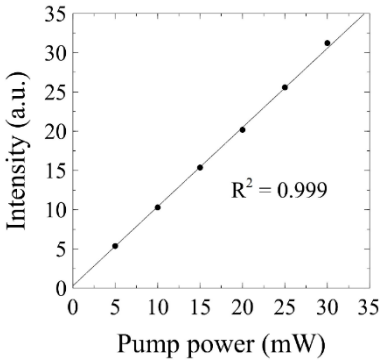

Figure 3.4. Pump power dependence of HbO_2.

Next, we measured the relationship between hemoglobin sO_2 and transient absorption signal at chosen pump probe wavelengths. UV/Vis spectroscopy was used as the gold standard for

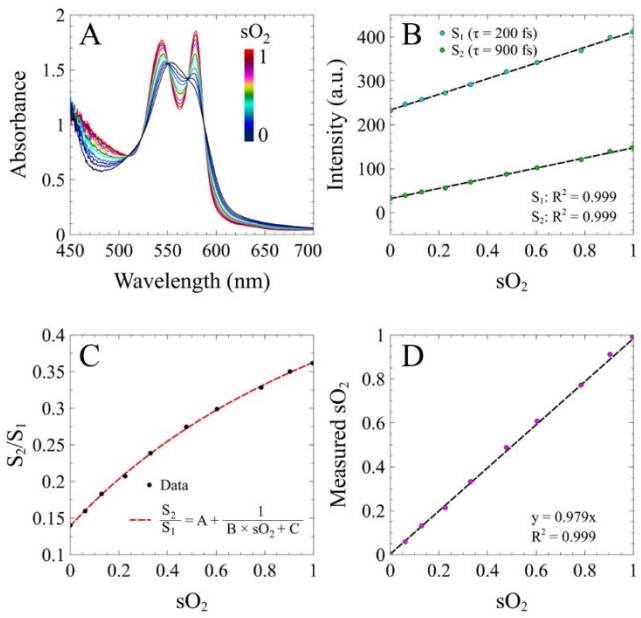

Figure 3.5. Quantifying the relationship between hemoglobin sO_2 and TAM signal intensity. A) UV/Vis spectra of the transition from Hb to HbO_2. B) TAM intensity dependence on sO_2. C) Ratiometric calibration of TAM measurements for sO_2 quantification. D) Accuracy of ratiometric TAM sO_2 quantification against gold standard (UV/Vis).

determining sO_2.[30,31] First, extracted hemoglobin was deoxygenated through exposure to 1.7 mL/min N_2 for ~2 hour. The solution was then slowly re-oxygenated through exposure to ambient air under constant stirring for 10 minutes. Samples were collected every 20 seconds[34] through the oxygenation process and sealed in custom made airtight cuvettes to prevent further oxygenation. Figure 3.5A shows the UV/Vis spectra of hemoglobin at sO_2 levels ranging from 0 - 100% at ~10% increments. As the hemoglobin becomes more oxygenated, the single peak of Hb at 550 nm disappears giving way to two peaks near 540 and 580 nm. After sO_2 quantification via UV/Vis, the transient decay kinetics of the same samples were interrogated at two probe delays, τ = 200 fs and τ = 900 fs, simultaneously. These delays were chosen to mitigate the presence of parasitic signals, such as cross phase modulation and the photothermal effect, that are present near τ = 0 fs.[35]. Figure 3.5B shows the relationship between sO_2 and TAM intensity at each probe delay. As expected, both TAM signals increase linearly (R^2 = 0.999) with sO_2 according to Equations 1 and 2:

$$S_1 = [\mathrm{HbT}] \times sO_2 \times \sigma_{1,\mathrm{HbO_2}} + [\mathrm{HbT}] \times (1\text{-}sO_2) \times \sigma_{1,\mathrm{Hb}}$$

$$S_2 = [\mathrm{HbT}] \times sO_2 \times \sigma_{2,\mathrm{HbO_2}} + [\mathrm{HbT}] \times (1\text{-}sO_2) \times \sigma_{2,\mathrm{Hb}}$$

where S_1 and S_2 are the TAM intensities at each probe delay, τ = 200 fs and τ = 900 fs, respectively, [HbT] is the total hemoglobin concentration, and σ_1 and σ_2 are the signal response of each hemoglobin species at each probe delay. From the ratio of these two equations, sO_2 can be determined. This approach is necessary as it removes the effects of light scattering and variations in hemoglobin concentration from sO_2 quantification. The ratio of the intensities, dependent upon only sO_2, can be expressed as

$$\frac{S_2}{S_1} = A + \frac{1}{B \times sO_2 + C}$$

Here A, B, and C are values determined via least-square fitting. Figure 3.5C plots the ratio of the two intensities and the fit with Equation 3. From this ratio, sO_2 measured with TAM can be calculated and compared against the true sO_2 determined by UV/Vis measurements. Figure 3.5D shows the accuracy (R^2 = 0.999) of TAM measured sO_2 against the true sO_2 and the quality of the fit.

We demonstrate *in vitro* sO_2 hemoglobin quantification of whole bovine blood samples. Whole blood was fully deoxygenated via stirring under 100% N_2 atmosphere for 2 hours as previously reported.[30] Eight samples were collected as the blood was exposed to ambient air and allowed to reoxygenate. One representative field of view (~150 × 150 μm) is shown in Figure 3.6. Two images, Figures 3.6A and 3.6B, were collected simultaneously at probe delays of τ = 200 fs and τ = 900 fs, respectively. Here we observed the characteristic disc shape of the RBCs in both images, along with a ~3-fold difference in intensity between the two probe delays. We threshold the images to remove low intensity pixels that hinder accurate quantification. Images are then segmented to locate individual RBCs (n ~ 750). The intensity ratio (S_2/S_1) of each pixel contained within a RBC is averaged to return a single sO_2 for each RBC, as shown in Figure 3.6C. Interestingly, the transient lifetime kinetics vary between hemoglobin solution and whole blood.

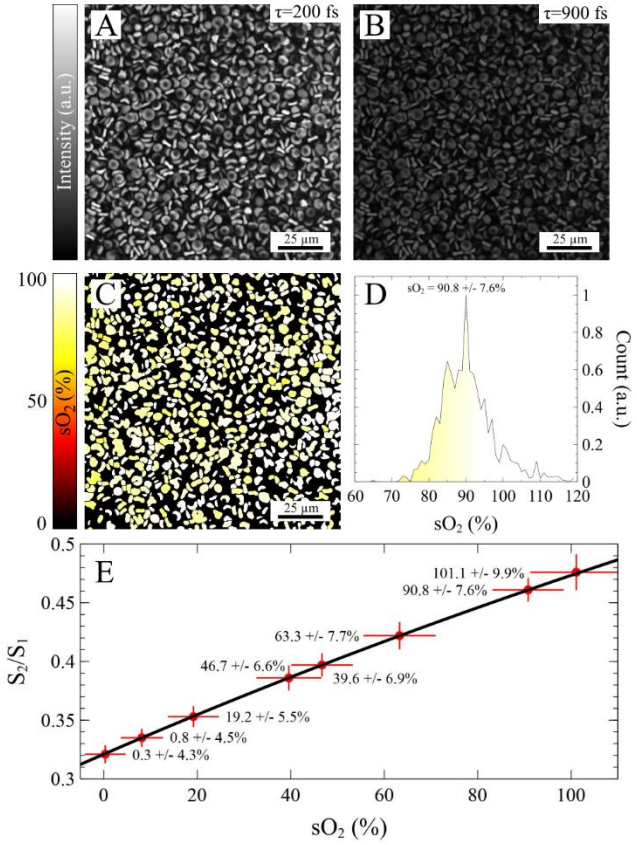

Figure 3.6. *In vitro* ratiometric TAM of whole blood. A,B) Bovine blood images at probe delays of τ=200 fs and τ=900 fs. C) Ratiometric sO_2 mapping. D) sO_2 histogram of C. E) Results of ratiometric sO_2 mapping for all eight samples. Data points shown in red, fit shown in black.

As a result, a hemoglobin solution calibration curve does not accurately quantify the sO_2 of whole blood. We believe that this is due to either the partial denaturation of the protein during extraction or the presence of a cell-specific background signal.[36] Instead, TAM images of fully oxygenated and fully deoxygenated whole blood (sO_2 = 0% and sO_2 = 100%) were used as calibration points for the whole blood experiments. We believe that the linearity of TAM with sO_2 (R^2 = 0.999) justifies the use of just two endpoints for calibration. Using this method, we determined the average sO_2 of all RBCs in Figure 3.6C to be 90.8 ± 7.6%. Figure 3.6D shows the corresponding histogram of the field of view. The calculated sO_2 of all eight blood samples collected are plotted in Figure 3.6E. The average standard deviation of sO_2 is ~7% across all eight samples. This could be due to either cell to cell variation or measurement uncertainty. To determine cell to cell variation, we compared the sO_2 histogram of three RBCs (Figure 3.7). The measured sO_2 of the three RBCs was 78.0 ± 5.5%, 89.9 ± 5.2%, and 1.00 ± 4.3%. The smaller intracellular sO_2 standard deviation observed compared to intercellular sO_2 suggest that the larger variations observed in whole blood are due to intrinsic cell-to-cell variation. This is

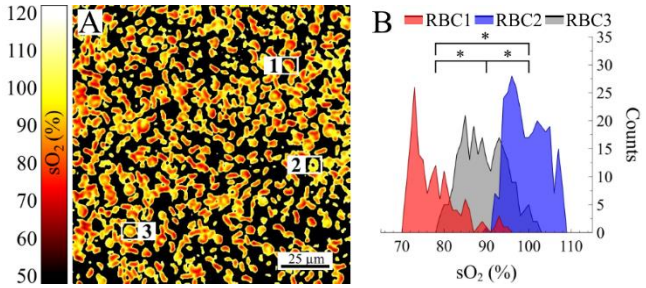

Figure 3.7. Cell to cell sO_2 variation. A) sO_2 map of RBCs. B) Histogram of three RBC sO_2 measurements indicated in (a), *p < 0.001

further verified by comparing the statistical differences of individual RBCs. Figure 3.7B shows three RBCs with statistically significant sO_2 differences ($p < 0.001$), despite the same exposure time to ambient air. The origin of this intrinsic difference warrants further studies. Nonetheless, recent research demonstrated a change in sO_2 of ~10% in response to visual stimuli in murine brains, suggesting our TAM-based method is sensitive enough to detect physiologically relevant changes in blood oxygenation, even at the single RBC level.[7] Lastly, we observed slight changes in transient absorption kinetics after repeat imaging of a field of view (data not shown). This may be due to sample heating or photodamage. To avoid this perturbation, we refrain from imaging a field of view multiple times.

3.4 CONCLUSION

In conclusion, we have demonstrated the first real-time quantification of hemoglobin sO_2 with TAM. This was accomplished through simultaneous detection of two TAM signals at two pump-probe delays. To the best of our knowledge, this is the first demonstration of real-time imaging of sO2 using the intrinsic nonlinear absorption of hemoglobin. Additionally, we surveyed several probe wavelengths at a constant pump wavelength, 1040 nm, and determined that a probe wavelength of 700 nm provided the strongest signal and extensive differences in transient lifetime kinetics between HbO_2 and Hb. We believe that TAM will benefit from additional optimization of excitation wavelengths. More specifically, we have shown that probe wavelengths closer to the pump wavelength have increased contribution of GSB which greatly increases the dynamic

range/sensitivity of ratiometric hemoglobin TAM. Currently the wavelength tuning is limited by the fixed pump laser. With additional optimization of the pump wavelength by using tunable lasers sources such as optical parametric oscillator or supercontinuum generation, the contributions of each TAM process (i.e., TPA, ESA, GSB) can be more precisely tuned to improve sensitivity. Nevertheless, the demonstrated method already offers more than a thousand-fold improvement in measurement speed compared to the current state-of-the-art 2PLM, while providing the same spatial resolution without the use of any exogenous agents. With further improvement in sensitivity, our technique offers a powerful tool for label-free imaging of sO_2 with both *in vitro* (e.g., investigating sO_2 levels in sickle cell disease or malaria models) and *in vivo* (e.g., quantifying sO_2 throughout angiogenesis in tumor models or monitoring sO_2 involvement in neuronal activity) applications.

3.5 REFERENCES

(1) Perutz, M. F.; Rossmann, M. G.; Cullis, A. F.; Muirhead, H.; Will, G.; North, A. C. T. Structure of Hæmoglobin: A Three-Dimensional Fourier Synthesis at 5.5-Å. Resolution, Obtained by X-Ray Analysis. *Nature* **1960**, *185* (4711), 416. https://doi.org/10.1038/185416a0.
(2) Chan, E. D.; Chan, M. M.; Chan, M. M. Pulse Oximetry: Understanding Its Basic Principles Facilitates Appreciation of Its Limitations. *Respiratory Medicine* **2013**, *107* (6), 789–799. https://doi.org/10.1016/j.rmed.2013.02.004.
(3) Logothetis, N. K. The Underpinnings of the BOLD Functional Magnetic Resonance Imaging Signal. *J. Neurosci.* **2003**, *23* (10), 3963–3971.
(4) Gagnon, L.; Sakad i, S.; Lesage, F.; Musacchia, J. J.; Lefebvre, J.; Fang, Q.; Yucel, M. A.; Evans, K. C.; Mandeville, E. T.; Cohen-Adad, J.; Polimeni, J. R.; Yaseen, M. A.; Lo, E. H.; Greve, D. N.; Buxton, R. B.; Dale, A. M.; Devor, A.; Boas, D. A. Quantifying the Microvascular Origin of BOLD-FMRI from First Principles with Two-Photon Microscopy and an Oxygen-Sensitive Nanoprobe. *Journal of Neuroscience* **2015**, *35* (8), 3663–3675. https://doi.org/10.1523/JNEUROSCI.3555-14.2015.
(5) Jennings, D.; Raghunand, N.; Gillies, R. J. Imaging Hemodynamics. *Cancer Metastasis Rev* **2008**, *27* (4), 589–613. https://doi.org/10.1007/s10555-008-9157-4.
(6) Laviña, B. Brain Vascular Imaging Techniques. *Int J Mol Sci* **2016**, *18* (1). https://doi.org/10.3390/ijms18010070.
(7) Wang, L.; Maslov, K.; Wang, L. V. Single-Cell Label-Free Photoacoustic Flowoxigraphy in Vivo. *PNAS* **2013**, *110* (15), 5759–5764. https://doi.org/10.1073/pnas.1215578110.

(8) Parpaleix, A.; Goulam Houssen, Y.; Charpak, S. Imaging Local Neuronal Activity by Monitoring PO_2 Transients in Capillaries. *Nat. Med.* **2013**, *19* (2), 241–246. https://doi.org/10.1038/nm.3059.
(9) Kisler, K.; Lazic, D.; Sweeney, M. D.; Plunkett, S.; El Khatib, M.; Vinogradov, S. A.; Boas, D. A.; Sakadži´, S.; Zlokovic, B. V. *In Vivo* Imaging and Analysis of Cerebrovascular Hemodynamic Responses and Tissue Oxygenation in the Mouse Brain. *Nature Protocols* **2018**, *13* (6), 1377–1402. https://doi.org/10.1038/nprot.2018.034.
(10) Kagemann, L.; Wollstein, G.; Wojtkowski, M.; Ishikawa, H.; Townsend, K. A.; Gabriele, M. L.; Srinivasan, V. J.; Fujimoto, J. G.; Schuman, J. S. Spectral Oximetry Assessed with High-Speed Ultra-High-Resolution Optical Coherence Tomography. *J Biomed Opt* **2007**, *12* (4), 041212. https://doi.org/10.1117/1.2772655.
(11) Hillman, E. M. C. Optical Brain Imaging in Vivo: Techniques and Applications from Animal to Man. *J Biomed Opt* **2007**, *12* (5), 051402. https://doi.org/10.1117/1.2789693.
(12) Pi, S.; Camino, A.; Wei, X.; Simonett, J.; Cepurna, W.; Huang, D.; Morrison, J. C.; Jia, Y. Rodent Retinal Circulation Organization and Oxygen Metabolism Revealed by Visible-Light Optical Coherence Tomography. *Biomed. Opt. Express, BOE* **2018**, *9* (11), 5851–5862. https://doi.org/10.1364/BOE.9.005851.
(13) Zhang, H. F.; Maslov, K.; Stoica, G.; Wang, L. V. Functional Photoacoustic Microscopy for High-Resolution and Noninvasive in Vivo Imaging. *Nat. Biotechnol.* **2006**, *24* (7), 848–851. https://doi.org/10.1038/nbt1220.
(14) Devor, A.; Sakadžić, S.; Yaseen, M. A.; Roussakis, E.; Tian, P.; Slovin, H.; Vanzetta, I.; Teng, I.; Saisan, P. A.; Sinks, L. E.; Dale, A. M.; Vinogradov, S. A.; Boas, D. A. Functional Imaging of Cerebral Oxygenation with Intrinsic Optical Contrast and Phosphorescent Probes. In *Optical Imaging of Neocortical Dynamics*; Weber, B., Helmchen, F., Eds.; Neuromethods; Humana Press: Totowa, NJ, 2014; pp 225–253. https://doi.org/10.1007/978-1-62703-785-3_14.
(15) Sakadžić, S.; Roussakis, E.; Yaseen, M. A.; Mandeville, E. T.; Srinivasan, V. J.; Arai, K.; Ruvinskaya, S.; Devor, A.; Lo, E. H.; Vinogradov, S. A.; Boas, D. A. Two-Photon High-Resolution Measurement of Partial Pressure of Oxygen in Cerebral Vasculature and Tissue. *Nat Methods* **2010**, *7* (9), 755–759. https://doi.org/10.1038/nmeth.1490.
(16) Spencer, J. A.; Ferraro, F.; Roussakis, E.; Klein, A.; Wu, J.; Runnels, J. M.; Zaher, W.; Mortensen, L. J.; Alt, C.; Turcotte, R.; Yusuf, R.; Côté, D.; Vinogradov, S. A.; Scadden, D. T.; Lin, C. P. Direct Measurement of Local Oxygen Concentration in the Bone Marrow of Live Animals. *Nature* **2014**, *508* (7495), 269–273. https://doi.org/10.1038/nature13034.
(17) Lyons, D. G.; Parpaleix, A.; Roche, M.; Charpak, S. Mapping Oxygen Concentration in the Awake Mouse Brain. *eLife* **2016**, *5*, e12024. https://doi.org/10.7554/eLife.12024.
(18) Esipova, T. V.; Barrett, M. J. P.; Erlebach, E.; Masunov, A. E.; Weber, B.; Vinogradov, S. A. Oxyphor 2P: A High-Performance Probe for Deep-Tissue Longitudinal Oxygen Imaging. *Cell Metabolism* **2019**, *29* (3), 736-744.e7. https://doi.org/10.1016/j.cmet.2018.12.022.
(19) Dorshow, R. B.; Bugaj, J. E.; Burleigh, B. D.; Duncan, J. R.; Johnson, M. A.; Jones, W. B. Noninvasive Fluorescence Detection of Hepatic and Renal Function. *J Biomed Opt* **1998**, *3* (3), 340–345. https://doi.org/10.1117/1.429854.
(20) Fu, D.; Ye, T.; Matthews, T. E.; Chen, B. J.; Yurtserver, G.; Warren, W. S. High-Resolution *in Vivo* Imaging of Blood Vessels without Labeling. *Opt. Lett., OL* **2007**, *32* (18), 2641–2643. https://doi.org/10.1364/OL.32.002641.

(21) Fu, D.; Matthews, T. E.; Ye, T.; Piletic, I. R.; Warren, W. S. Label-Free in Vivo Optical Imaging of Microvasculature and Oxygenation Level. *J Biomed Opt* **2008**, *13* (4), 040503. https://doi.org/10.1117/1.2968260.
(22) Fu, D. *Developing Novel Nonlinear Optical Contrast for Biomedical Imaging*; Princeton University, Series Ed.; 2009, 2009.
(23) Chen, T.; Huang, Y. Label-Free Transient Absorption Microscopy for Red Blood Cell Flow Velocity Measurement in Vivo. *Anal. Chem.* **2017**, *89* (19), 10120–10123. https://doi.org/10.1021/acs.analchem.7b01952.
(24) Zhang, L.; Zou, X.; Zhang, B.; Cui, L.; Zhang, J.; Mao, Y.; Chen, L.; Ji, M. Label-Free Imaging of Hemoglobin Degradation and Hemosiderin Formation in Brain Tissues with Femtosecond Pump-Probe Microscopy. *Theranostics* **2018**, *8* (15), 4129–4140. https://doi.org/10.7150/thno.26946.
(25) Chen, A. J.; Yuan, X.; Li, J.; Dong, P.; Hamza, I.; Cheng, J.-X. Label-Free Imaging of Heme Dynamics in Living Organisms by Transient Absorption Microscopy. *Anal. Chem.* **2018**, *90* (5), 3395–3401. https://doi.org/10.1021/acs.analchem.7b05046.
(26) Lai, M.; Lai, S. T.; Swinger, C. Single-Grating Laser Pulse Stretcher and Compressor. *Appl. Opt., AO* **1994**, *33* (30), 6985–6987. https://doi.org/10.1364/AO.33.006985.
(27) He, R.; Xu, Y.; Zhang, L.; Ma, S.; Wang, X.; Ye, D.; Ji, M. Dual-Phase Stimulated Raman Scattering Microscopy for Real-Time Two-Color Imaging. *Optica, OPTICA* **2017**, *4* (1), 44–47. https://doi.org/10.1364/OPTICA.4.000044.
(28) Francis, A.; Berry, K.; Chen, Y.; Figueroa, B.; Fu, D. Label-Free Pathology by Spectrally Sliced Femtosecond Stimulated Raman Scattering (SRS) Microscopy. *PLOS ONE* **2017**, *12* (5), e0178750. https://doi.org/10.1371/journal.pone.0178750.
(29) Malinauskas, R. A. Plasma Hemoglobin Measurement Techniques for the in Vitro Evaluation of Blood Damage Caused by Medical Devices. *Artif Organs* **1997**, *21* (12), 1255–1267.
(30) Liu, P.; Zhu, Z.; Zeng, C.; Nie, G. Specific Absorption Spectra of Hemoglobin at Different PO2 Levels: Potential Noninvasive Method to Detect PO2 in Tissues. *J Biomed Opt* **2012**, *17* (12), 125002. https://doi.org/10.1117/1.JBO.17.12.125002.
(31) Zijlstra, W. G.; Buursma, A. Spectrophotometry of Hemoglobin: Absorption Spectra of Bovine Oxyhemoglobin, Deoxyhemoglobin, Carboxyhemoglobin, and Methemoglobin. *Comparative Biochemistry and Physiology Part B: Biochemistry and Molecular Biology* **1997**, *118* (4), 743–749. https://doi.org/10.1016/S0305-0491(97)00230-7.
(32) Auer, B. M.; Skinner, J. L. IR and Raman Spectra of Liquid Water: Theory and Interpretation. *J. Chem. Phys.* **2008**, *128* (22), 224511. https://doi.org/10.1063/1.2925258.
(33) Ji, M.; Orringer, D. A.; Freudiger, C. W.; Ramkissoon, S.; Liu, X.; Lau, D.; Golby, A. J.; Norton, I.; Hayashi, M.; Agar, N. Y. R.; Young, G. S.; Spino, C.; Santagata, S.; Camelo-Piragua, S.; Ligon, K. L.; Sagher, O.; Xie, X. S. Rapid, Label-Free Detection of Brain Tumors with Stimulated Raman Scattering Microscopy. *Science Translational Medicine* **2013**, *5* (201), 201ra119-201ra119. https://doi.org/10.1126/scitranslmed.3005954.
(34) Rinia, H. A.; Bonn, M.; Vartiainen, E. M.; Schaffer, C. B.; Müller, M. Spectroscopic Analysis of the Oxygenation State of Hemoglobin Using Coherent Anti-Stokes Raman Scattering. *J. Biomed. Opt* **2006**, *11* (5), 050502-050502–050503. https://doi.org/10.1117/1.2355671.

(35) Berto, P.; Andresen, E. R.; Rigneault, H. Background-Free Stimulated Raman Spectroscopy and Microscopy. *Phys. Rev. Lett.* **2014**, *112* (5), 053905. https://doi.org/10.1103/PhysRevLett.112.053905.
(36) Oh, J.-Y.; Hamm, J.; Xu, X.; Genschmer, K.; Zhong, M.; Lebensburger, J.; Marques, M. B.; Kerby, J. D.; Pittet, J.-F.; Gaggar, A.; Patel, R. P. Absorbance and Redox Based Approaches for Measuring Free Heme and Free Hemoglobin in Biological Matrices. *Redox Biology* **2016**, *9*, 167–177. https://doi.org/10.1016/j.redox.2016.08.003.

Chapter 4. LABEL-FREE PATHOLOGY BY SPECTRALLY SLICED FEMTOSECOND STIMULATED RAMAN SCATTERING (SRS) MICROSCOPY

4.1 INTRODUCTION

Since its discovery over a hundred years ago, hematoxylin and eosin staining (H&E staining) has long served as the 'gold standard' of histopathology for achieving strong visual contrast between various cellular features.[1] This contrast is achieved via chemical labelling of specific functional groups present throughout the tissue giving rise to spatial-chemical distribution maps of the tissue. Exploiting key chemical differences between healthy and diseased cells, pathologists can use cellular morphology to not only diagnose the disease but the severity of the condition as well from such staining.[2] While H&E staining is not likely to be replaced by any current technologies, the requirement of tissue excision, sectioning, and staining severely limits its use in an intraoperative setting. Quick and accurate diagnosis is crucial for effective surgical treatment of a variety of cancers including brain, breast, prostate, etc., in which any residual tumor will increase the risk of cancer relapse. Therefore, a real-time assessment of histopathological features of either excised tumor tissue or the surgical cavity may significantly improve the outcome of the patient.[3]

Several competing optical techniques have been developed to address the challenge of intraoperative tissue assessment. One powerful tool is optical coherence tomography (OCT), a low-coherence interferometric technique that images tissue structure at high resolution based on variations in refractive index.[4–6] *In vivo* OCT was initially developed for ophthalmology, but has

been rapidly extended to epidermal, cervical, esophageal, and gastrointestinal tissues.[7] Most recently, it has been used for detection of brain tumor infiltration.[8] OCT has a relatively large penetration depth of 1-3 mm, compared to other optical microscopy techniques. However, it suffers from a lack of chemical specificity and thus is unable to provide detailed cellular morphology.

In order to gain chemical contrast, many groups have worked to use autofluorescence and fluorescent staining coupled with confocal or multiphoton microscopy to visualize cellular structures. Although more chemically specific than OCT, both confocal and multiphoton fluorescence are still limited in contrasts: only a few native *in vivo* species are known to autofluoresce, most notably collagen. For tissues that lack strong autofluorescence, an exogenous agent is added to promote strong fluorescent contrast. The two main staining methods are 5-aminolevulinic acid (5-ALA)-induced protoporphyrin IX and nuclear staining, commonly achieved using acridine orange. With nuclear staining, both confocal and multiphoton microscopies have been demonstrated to provide cellular contrasts similar to H&E that enables rapid *ex vivo* assessment of tumor margins.[9,10] The use of fluorescent dyes does not preclude fluorescence microscopy from *in vivo* imaging, as demonstrated by 5-ALA stained, fluorescence-guided resection surgeries[11–14], but does present additional avenues of intrasample and intersample discrepancies. Dye-based methods suffer from drawbacks including heterogeneous delivery, nonspecific staining, and FDA approval limitations.[15]

Stimulated Raman scattering (SRS) microscopy is an emerging analytical, label-free technique that has demonstrated exceptional *ex vivo*[16–18] and *in vivo*[19,20] tissue imaging capabilities. Compared with fluorescence, it provides specific chemical contrasts without the need for staining. Raman scattering is the inelastic collision between an incident photon and a molecule. The transfer

of energy excites a vibrational mode unique to that molecule, making Raman scattering highly qualified to study inhomogeneous systems such as biological tissues. The advent of coherent Raman scattering microscopy addressed the major limitation of applying Raman scattering to tissue imaging – the data acquisition speed. Coherent Raman scattering, including both coherent anti-Stokes Raman scattering (CARS) and SRS, improves the feeble spontaneous Raman scattering effect by a few orders of magnitude, allowing rapid image acquisition at a speed up to video-rate.[21] Traditionally, SRS is achieved using narrowband, picosecond pulses tuned to a particular Raman transition that has a resonance frequency Ω equal to the frequency difference between the pump and the Stokes laser ω_P - ω_S.[22] The most commonly used laser system is neodymium based oscillator and a synchronously pumped optical parametric oscillator. The spectral resolution of SRS imaging is determined by the bandwidths of the picosecond lasers, which are typically less than 10 cm^{-1}. In order to open SRS up to multi-band excitation, many groups began experimenting with broadband, femtosecond pulses. Multi-band excitation has been reported via frequency tuning[20], multiplexing[23,24], and spectral focusing.[25] These studies paved the way for broadband, femtosecond SRS as an alternative to the traditional narrowband, picosecond SRS.

Recently, the viability of narrowband, picosecond SRS imaging of brain tumor margins with both frozen and fresh tissue as an alternative to H&E staining has been demonstrated.[17,18,26] In the work reported by Ji et al.[17,18], two-color SRS was adopted to acquire additional spectroscopic information, allowing for differentiation of various biochemical and morphological features. For biological samples, the two Raman transitions used are typically near 2845 and 2930 cm^{-1} for lipids and proteins, respectively. In the study conducted by Lu et al.[26], three-color SRS was employed, where the third channel probed corresponds to hemoglobin. While the work reported by Ji et al.

and Lu et al. demonstrates the powerful capabilities of their respective systems, the lasers they used have 7 ps long pulses, which suffer from low peak intensity and require high laser power for imaging. Since SRS signal scales with peak intensity, theory posits that spectrally broader, temporally shorter pulses provide higher signal-to-noise ratio (SNR) at the same optical power than narrowband, picosecond pulses. One notable study, conducted by Freudiger et al., detailed the improvement in SNR using spectrally broader, temporally shorter 2 ps pulses through a fiber-based SRS set up.[27] However, fiber-based set ups are limited by their own shortcomings, including high frequency laser noise and difficulties generating sufficiently high power compared to free-space lasers. Regardless, the work done by Freudiger et al. demonstrated that temporally shortened pulses produce higher SNR. Such a system has been recently used by Orringer for intraoperative histology of unprocessed surgical specimen.[28]

One important question that remains unsolved in two-color SRS based histopathology is what the optimal laser pulses for imaging are. In one study, a near 12-fold increase in SNR of lipids SRS was observed when the traditional narrowband, picosecond pulses were replaced with broadband, femtosecond SRS.[29] However, there is no systematic study of the influence of pulse duration on SNR. More importantly, spectral broadening associated with shorter pulses results in loss of spectral resolution. It is questionable that in two-color SRS imaging whether the same cell morphological contrasts can be obtained with broadened pulses. In this manuscript, we present two-color SRS tissue imaging using spectrally sliced broadband, femtosecond pulses to systematically investigate the influence of excitation laser bandwidth on SNR and image contrast. After spectral unmixing, our SRS images can provide visual protein/lipid contrast comparable to narrowband, picosecond SRS, and thus, analogous to H&E staining. Importantly, we find that a linear increase in SNR is achieved with pulse bandwidth increase up to 40 cm^{-1}, while almost

identical two-color contrasts are retained compared to narrowband pulses. The results agree with our numerical simulations. This finding has wide implications for future development of SRS imaging systems for intraoperative tumor margin assessment and early tumor diagnosis.

4.2 METHODOLOGY

4.2.1 *Experimental SRS Setup*

Our experimental set up used is shown in Figure 4.1. The spectral slicing process begins with a broadband femtosecond dual beam system (Insight DS+ from Spectra Physics) with an 80 MHz repetition rate. The two outputs are: a fixed output of 1040 nm with an average power of 800 mW and bandwidth of 60 cm^{-1} and a variable output from 680-1300 nm with an average power of 1.2 W and bandwidth of 150 cm^{-1}. Immediately following emission from the laser, the Stokes beam is modulated at 10 MHz using an electro-optical modulator (EOM). Next, both pulses, pump and Stokes, are spectrally dispersed by a transmission grating, physically sliced with a slit, and returned through the grating at a lower height than incidence to recollimate. The sliced pulses are then combined at a dichroic mirror and overlapped temporally using a delay line in the pump arm. The resulting beam is sent into a home-built laser scanning microscope. A 40X Nikon water immersion objective (Nikon 40X, NA = 1.25) is used to focus the beams onto to the tissue sample. At the focus, the Stokes beam has an average power of 35 mW and the pump has an average power of 40 mW. With a combined power of ~75 mW at the focus, we are imaging with similar optical power as recently reported for *in vivo* imaging of mouse brain vasculature[30], and 2-3-fold less optical power than other ultrafast *ex vivo* multiphoton imaging studies.[17,18,31] Moreover, Galli et al observed little to no photodamage of *ex vivo* mouse brain tissue under similar excitation parameters.[32] After passing through the condenser, the Stokes beam is filtered out and the pump

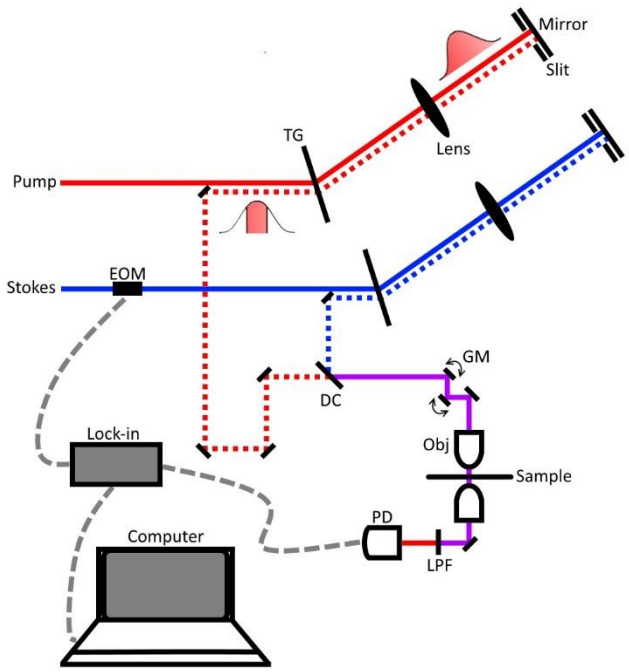

Figure 4.7. Experimental spectral slicing setup. The Stokes laser is modulated by an electro-optical modulator (EOM) at 10 MHz. Pulses are sliced via spectral dispersion through a transmission grating (TG) and a controllable slit placed near the focal point. After slicing, pulses are spatially and temporally synchronized at a dichroic mirror (DC) and directed onto a pair of galvanomirrors (GM). The beams are then sent through the 40x objective, sample, and condenser. Finally, the Stokes beam is filtered out using a low pass filter (LPF) before the beams terminate at the photodiode (PD). Dotted red and blue lines represent an offset in the beam height and the dashed grey lines detail the electrical connections between computer, PD, and lock-in amplifier.

reaches a silicon photodiode. Stimulated Raman loss (SRL) signal is detected with a home-built lock-in amplifier.[21] The layout was inspired by work reported by Zhang et al. using a 4-f system to achieve angle-to-wavelength pulse shaping.[33] Ours differs by adopting a "folded" 4-f system that uses the grating to recollimate the sliced pulses. Both the pump and Stokes pulses are narrowed using moveable slits that allow for control of bandwidth and central wavelength. The center wavelength and bandwidth of each pulse after slicing were verified using a home-built Michelson interferometer-based spectrometer.

4.2.2 *Mouse Tissue Preparation*

Brain, liver, kidney, and skin tissues were harvested from recently sacrificed mouse carcasses, which were provided by UW Animal Use Training Services (AUTS) according to IACUC protocol 3388-03. The mice (laboratory mice, *mus musculus*) were euthanized by isoflurane or CO_2 overdose and

cervical dislocation. The brain was exposed and extracted by removing the scalp and top of the skull. The kidney and liver were collected by making a Y-incision to expose the intestines then clipping the connective tissues. Skin tissues were excised using scissors after hair was removed with Nair. After excision, bulk tissues were placed in phosphate-buffered saline (PBS). Thin sections of tissue were prepared by razor blade sectioning and then placed on a glass slide with additional PBS. To prepare the sample for imaging, a glass coverslip was placed on top to sandwich the tissue specimen between the glass slide and the glass coverslip using double-sided tape as a spacer.

4.3 Results and Discussion

We first examined the results of spectral slicing using the aforementioned spectrometer. Figure 4.2 illustrates the effects of slicing on the Stokes pulse and provides the linear calibration of the slit

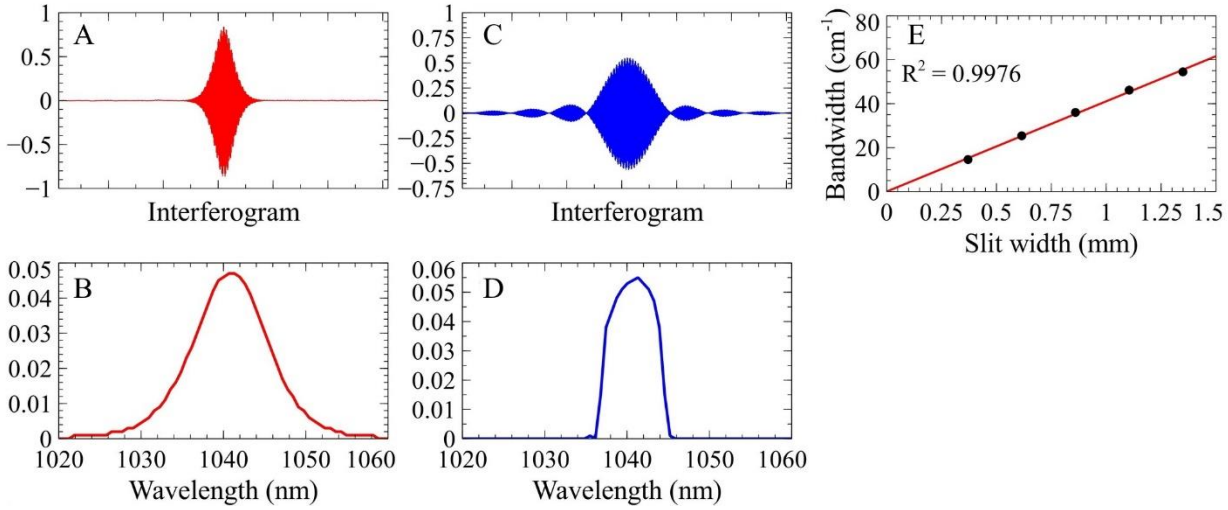

Figure 4.8. Effects of spectral slicing on the Stokes pulse. (a) Unsliced interferogram of Stokes pulse using a Michelson interferometer-based spectrometer. (b) Unsliced Stokes frequency profile via Fourier transform (FT) of unsliced interferogram. (c) Sliced interferogram of Stokes pulse. (d) Sliced Stokes frequency profile via FT of sliced interferogram. (e) Linearity of bandwidth as a function of slit width.

width. The collected interferograms of the unsliced Stokes pulses are collected and the calculated spectra via Fourier transform (FT) are displayed in Figures 4.2A and 4.2B, respectively. As evident by these two figures, the pulses produced by the laser are Gaussian-like in distribution. Spectral slicing induces a convolution of the laser pulse (Gaussian) and the slit (rectangle), shown in Figures 4.2C and 4.2D. After slicing, the interferogram more closely represents a sinc function (sin(x)/x), rather than Gaussian. We define the spectral bandwidth as the full width at half maximum (FWHM) in the frequency domain relative to the central wavelength. Figure 4.2E demonstrates the linearity of sliced spectral bandwidth as a function of slit width.

The Fourier transform relationship between frequency and time dictates that as a pulse narrows spectrally, it broadens temporally. Therefore, the pulse duration of an unsliced pulse is narrower than that of a sliced pulse. However, the cost of stronger peak intensity is reduced SRS spectral resolution of the selected Raman transition. The difference between using excitation bandwidths of 10 cm^{-1} and 60 cm^{-1} is shown in Figure 4.3. Using 10 cm^{-1} pulses, the 2855 cm^{-1} channel is predominately lipid signal and the 2935 cm^{-1} channel is more protein than lipid. When

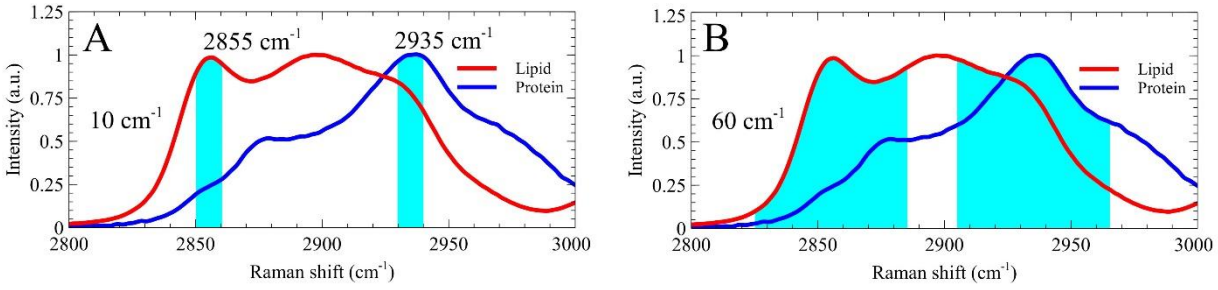

Figure. 4.9. Dependence of signal amplitude and contrast on bandwidth. Normalized spontaneous Raman spectra of bovine serum albumin (BSA) and oleic acid are shown as representative of proteins and lipids, respectively. Shown is the difference in excitation of the protein channel (2935 cm^{-1}) and the lipid channel (2855 cm^{-1}) with (a) 10 cm^{-1} pulses and (b) 60 cm^{-1} pulses.

the bandwidth is increased to 60 cm^{-1} each channel becomes less specific due to higher contributions from the competing chemical (e.g. lipid signal in the 2935 cm^{-1} channel).

To study this phenomenon, we imaged cross-sections of freshly harvested mouse brain at multiple bandwidths. Figure 4.4 demonstrates the increase in SNR associated with broadening the

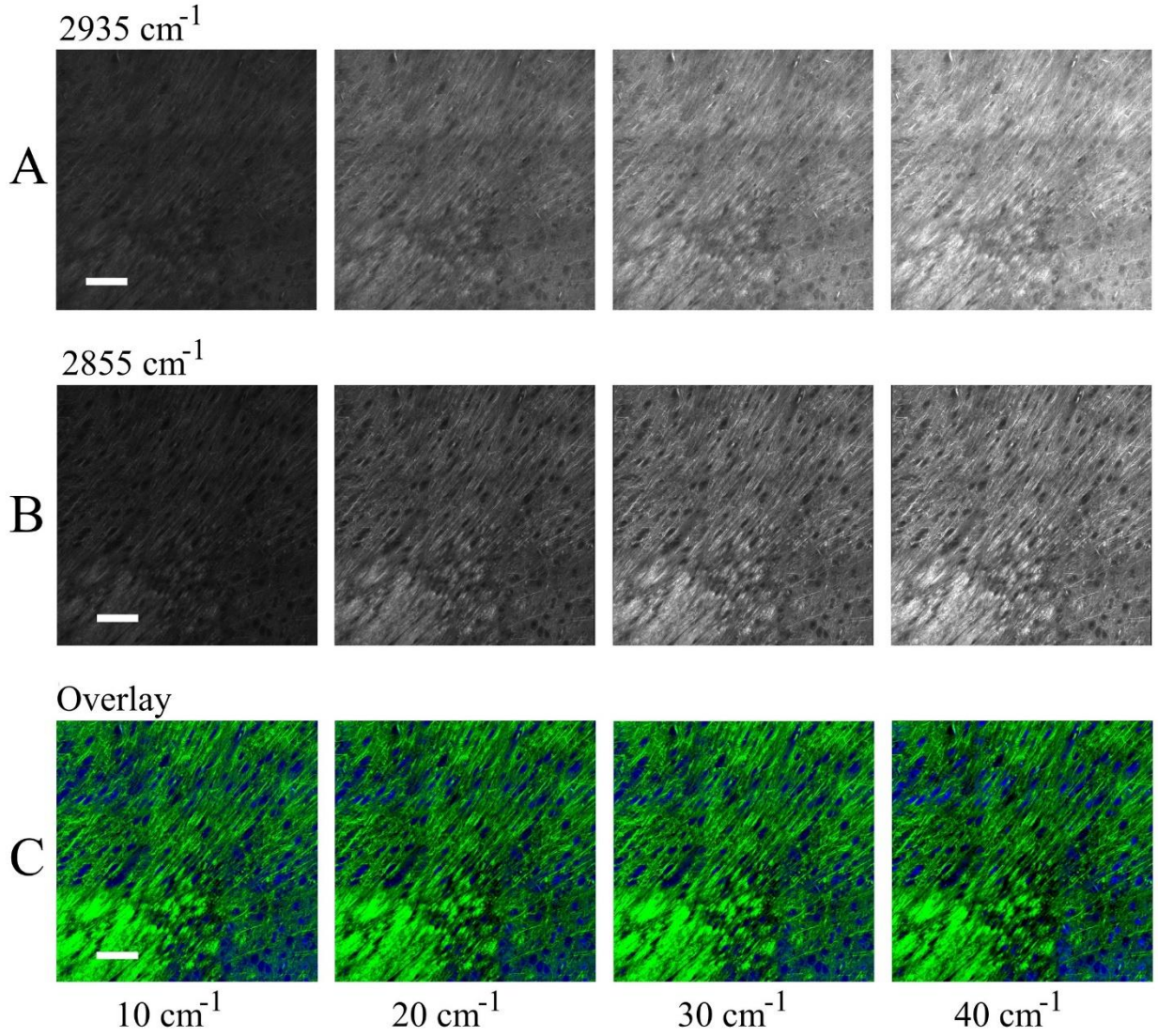

Figure 4.4. SRS imaging of mouse brain tissue. Imaging at (a) 2935 cm^{-1} (proteins) with bandwidths of 10 cm^{-1}, 20 cm^{-1}, 30 cm^{-1}, and 40 cm^{-1} from left to right and (b) 2855 cm^{-1} (lipids) with bandwidths of 10 cm^{-1}, 20 cm^{-1}, 30 cm^{-1}, and 40 cm^{-1} from left to right. Composite tissue images (c) show only slight differences between 10, 20, 30, and 40 cm^{-1} from left to right. Scale bar: 100 μm.

pulses from 10 to 40 cm^{-1} at constant excitation power. The images shown have been field normalized to mitigate the field effects caused by the imaging and stitching process. All of the images shown are on the same brightness and contrast scale allowing for a noticeable increase in signal intensity to be clearly observed. Next, the contribution of protein and lipids are unmixed using the same procedures as published by Ji et al.[18] This process is achieved by removing the lipid contribution from the protein channel via subtraction. To quantify the contribution of lipids in each channel, we measure the response of oleic acid (representative of cellular lipids) at each bandwidth for both channels. Knowing the contribution at a particular bandwidth for each channel allows us to appropriately scale the protein channel (2935 cm^{-1}) and subtract out the lipid channel (2855 cm^{-1}). Figure 4.4 provides the unmixed protein (A) and lipid (B) images and the overlay images (C) of mouse brain tissue; the protein channel is shown in blue and the lipid channel, green. The images have been shown at similar brightness and contrast scales to more easily compare the images between bandwidths. Features rich in protein, such as nuclei, appear blue, while features rich in lipids, such as myelin sheaths, appear green. From Figure 4.4, no apparent changes in contrast are easily observable. To quantify the variation between the images, the contrast between the two channels for several features was calculated and averaged. We define protein/lipid contrast as the ratio between protein rich nuclei and lipid rich cytoplasm. The results of this analysis and features used are shown in Figure 4.5.

In Figure 4.5 three curves are shown demonstrating (B) lipid and protein signal intensity and (C) protein/lipid contrast as a function of bandwidth. Figure 4.5B shows the agreement of experimental findings with our numerical simulation (Matlab 2016, Mathworks) detailing the relationship between SRS signal intensity and bandwidth/pulse duration using a previously derived formula.[34] Our simulation demonstrates that this relationship is dependent upon the bandwidth of

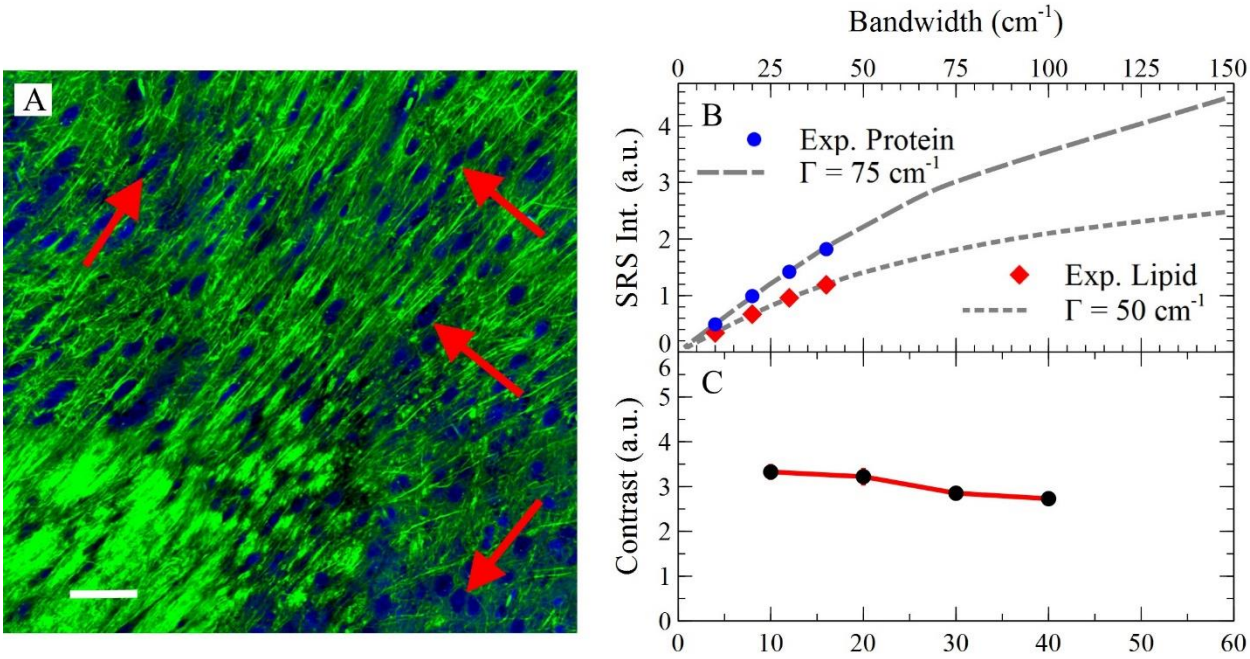

Figure 4.5. Signal and contrast dependence on bandwidth. A) SRS imaging of mouse brain tissue 30 cm^{-1} pulses. Total signal for the B) lipid and protein channels as a function of bandwidth are also shown to illustrate the increase in signal as bandwidth increases. The dashed and dotted gray lines are theoretical curves at 75 and 50 cm^{-1}, respectively. C) Contrast at four areas was averaged and plotted as a function of bandwidth. The image shown represents the four areas used and is the overlay at 30 cm^{-1} from Fig. 3 for reference. Scale bar: 200 μm.

the excitation pulses and the bandwidth of the Raman transition, Γ. More specifically, when excitation pulses are narrower than the Raman transition, the curve is linear; in the opposite case, the curve flattens out and plateaus. For cellular lipids and proteins, Γ is large, which we believe is responsible for the linearity of Figure 4.5B. By approximating the Raman transition of proteins and lipids to be 75 cm^{-1} and 50 cm^{-1}, respectively, we see that the experimental findings correlate well with the theoretical model. The linear regime of both curves is important because it suggests that optimized excitation conditions exist: inside the linear regime, SNR increases linearly with laser bandwidth; outside the linear regime, the risk of photodamage quickly increases with only marginal increase of SRS signal. Figure 4.5C relates the contrast between the channels to the excitation bandwidth. The trend shows a modest decrease in protein/lipid contrast with increasing

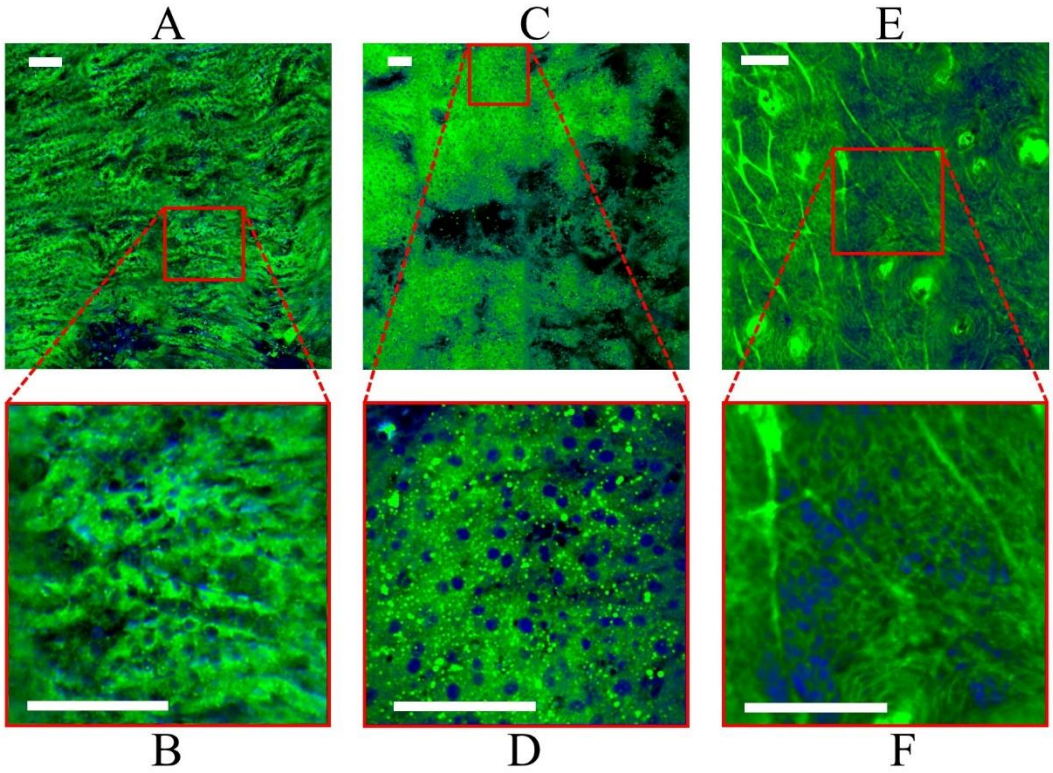

Figure 4.6. Broadband, femtosecond SRS imaging of mouse tissue using 40 cm^{-1} pulses. The tissues shown are (A, B) kidney, (C, D) liver, and (E, F) skin. For each tissue, the above image is a larger field of view (FOV) and the below image is a smaller FOV indicated by the red outline. After unmixing, the images are color coded and merged; the proteins are colored blue and the lipids, green. Scale bars: 100 μm

bandwidths, with the most substantial being the increase from 20 to 30 cm^{-1}. We believe that this is due to other chemical species present in the sample that are not taken into account in spectral unmixing.[16] In this study, we only consider the two most prevalent species, proteins and lipids, and neglect contributions from others, most notably water and nucleic acids. Water has a very broad band from 2900 to 3600 cm^{-1} with maxima around 3200 and 3400 cm^{-1}, and nucleic acids span 2850 to 3100 cm^{-1} with a maximum near 2955 cm^{-1}. Therefore, these species will predominantly contribute to the protein channel at 2935 cm^{-1}, with increasing contribution at larger bandwidth. These contributions confound spectral unmixing and diminish image contrast.

To verify our system's capabilities on a variety of biochemical compositions, we also imaged three other mouse tissues: liver, kidney, and skin. Figure 4.6 provides the post-processing overlay images of kidney (A, B), liver (C, D), and skin (E, F) using 40 cm^{-1} excitation pulses. Figures 4.6 (A, C, and E) all show a large field of view (FOV) and Figures 4.6 (B, D, and F) gives a smaller FOV at the specified location. From these images, it is evident that broadband pulses are equally effective at providing cellular morphological contrast across a wide range of chemical compositions.

Spectral slicing is a robust method of shaping pulses to very controllable bandwidths/pulse durations; however, a notable disadvantage is the loss of power associated with the physical slicing of the laser beams. One alternative method to pulse shaping is spectral focusing, wherein the excitation pulses are chirped through highly dispersive glass rods.[25,35] In spectral focusing, the Raman transition to be probed is chosen by the temporal delay between the pump and Stokes

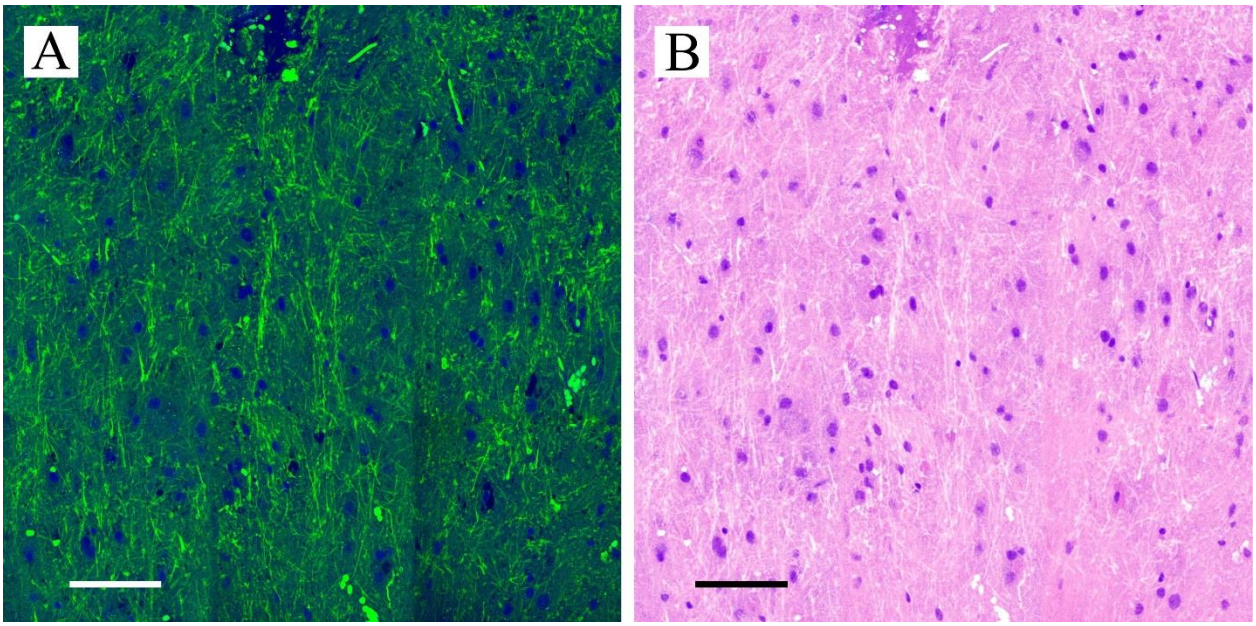

Figure 4.7. Simultaneous two-channel SRS imaging of mouse brain tissue using 30 cm^{-1} pulses. The mouse brain image shown was collected using dual-phase lock-in detection. A) Shows the proteins as blue and the lipids, green, while B) provides a pseudo-H&E color scheme. Scale bars: 100 μm

beams. We used dual-phase lock-in detection that has recently demonstrated by He to perform simultaneous two-color SRS imaging.[35] In our experiment, much shorter pulses were used for imaging. In Fig 4.7, we provide the results of simultaneous two-channel SRS imaging of freshly excised mouse brain tissue using 30 cm^{-1} excitation pulses with a combined power of 80 mW at the focus. The two transitions shown are 2850 cm^{-1} for lipid and 2945 cm^{-1} for protein excitation. These transitions and bandwidth differ from those used above due to technical differences between spectral slicing and two-channel SRS. Figure 4.7A provides the color scheme used above, while Figure 4.7B remaps the color scheme to a pseudo-H&E color scale.[36]

4.4 CONCLUSION

In summary, the use of spectrally sliced broadband, femtosecond SRS provides similar protein/lipid contrast to narrowband, picosecond SRS after channel unmixing. The main benefit of using broader pulses is increased SNR which is crucial for improving imaging speeds and the limit of detection of SRS. To this extent, we have characterized the relationship between protein/lipid contrast and spectral bandwidth and shown that contrast only decrease slightly by going from 10 cm^{-1} to 40 cm^{-1}. Moreover, we have demonstrated the optimization of excitation parameters for proteins and lipids within the linear regime between signal intensity and excitation laser bandwidth. We further demonstrated that simultaneous two-color SRS imaging can be achieved with spectral focusing instead of spectral slicing, which more efficiently uses the laser power. The optimal bandwidth for excitation depends on both contrast and photodamage. In previous demonstration of two-color SRS based histopathology, 2 ps and 7 ps pulses were used for SRS excitation.[17,18,26,28] It was shown that 2 ps pulses provide better SNR than 7 ps pulses given the same laser power. For transform-limited pulses, 2 ps pulses correspond to ~5-10 cm^{-1} laser

bandwidth. Our experiment demonstrates that a further 4-fold increase in SNR can be gained by using even shorter pulses without significant loss of morphological contrasts. Although bandwidths larger than 40 cm^{-1} may still provide contrasts without much degradation, the gain in SNR rapidly decreases due to the limit in Raman transition width of proteins and lipids according to our numerical simulation. Moreover, the photodamage due to high peak power may be of concern at very large laser bandwidth. Our experimental results are promising as a benchmark in two-color SRS based pathology applications. Yet, more work needs to be done regarding broadband, femtosecond SRS. Although we have demonstrated the viability of our system on imaging a wide variety of tissue with varying lipid content, for a more complex tissue environment that contains substantially different biochemical composition or tissue inhomogeneity, our system still needs to be tested. Future work will focus on comparing broadband two-color SRS imaging of human tumor tissues to H&E staining to validate its diagnostic capability.

The benefits demonstrated in this manuscript are essential for the integration of SRS into an intraoperative/guided surgery setting. First, as we, and other groups, have demonstrated, the switch from traditional picosecond excitation lasers to femtosecond lasers is accompanied by significant SNR increase. Theoretically, an order of magnitude increase in SNR is expected for 40 cm^{-1} broadband pulses compared to the most common 7 ps laser system given the same incidence power. With higher SNR, less optical power can be used to achieve the same quality of images and imaging speed which mitigates the risk of potential photodamage. Another benefit of broadband, femtosecond SRS is the choice of laser source. In translating from bench to the bedside, fiber laser is poised to play an essential role in clinical imaging. Due to high nonlinearity associated with femtosecond pulses, it is often simpler to construct femtosecond lasers compared to picosecond lasers. As a result, more femtosecond lasers are available on the market. Finally,

broadband, femtosecond pulses allows simultaneous two-color SRS imaging due to the proximity of the protein and lipid peaks, as demonstrated in this manuscript. Simultaneous two-color SRS offers quicker data acquisition by removing the time required to switch wavelengths, which is necessary for narrowband, picosecond SRS. Furthermore, as demonstrated herein by the results of two-color unmixing, protein/lipid visual contrast is not significantly affected by the bandwidth of the pulses used, within the range of widths detailed. Thus, a carefully optimized broadband, femtosecond system could provide sufficient protein/lipid contrast at significantly higher imaging speed than current narrowband, picosecond two-color SRS.

4.5 REFERENCES

(1) King, D. F.; King, L. A. C. A Brief Historical Note on Staining by Hematoxylin and Eosin. *The American Journal of Dermatopathology* **1986**, *8* (2), 168.
(2) Chan, J. K. C. The Wonderful Colors of the Hematoxylin–Eosin Stain in Diagnostic Surgical Pathology. *Int J Surg Pathol* **2014**, *22* (1), 12–32. https://doi.org/10.1177/1066896913517939.
(3) Schneider, J. P.; Schulz, T.; Schmidt, F.; Dietrich, J.; Lieberenz, S.; Trantakis, C.; Seifert, V.; Kellermann, S.; Schober, R.; Schaffranietz, L.; Laufer, M.; Kahn, T. Gross-Total Surgery of Supratentorial Low-Grade Gliomas under Intraoperative MR Guidance. *American Journal of Neuroradiology* **2001**, *22* (1), 89–98.
(4) Hariri, L. P.; Mino-Kenudson, M.; Mark, E. J.; Suter, M. J. In Vivo Optical Coherence Tomography: The Role of the Pathologist. *Archives of Pathology & Laboratory Medicine* **2012**, *136* (12), 1492–1501. https://doi.org/10.5858/arpa.2012-0252-SA.
(5) Tearney, G. J.; Brezinski, M. E.; Bouma, B. E.; Boppart, S. A.; Pitris, C.; Southern, J. F.; Fujimoto, J. G. In Vivo Endoscopic Optical Biopsy with Optical Coherence Tomography. *Science* **1997**, *276* (5321), 2037–2039. https://doi.org/10.1126/science.276.5321.2037.
(6) Huang, D.; Swanson, E. A.; Lin, C. P.; Schuman, J. S.; Stinson, W. G.; Chang, W.; Hee, M. R.; Flotte, T.; Gregory, K.; Puliafito, C. A.; Et, A. Optical Coherence Tomography. *Science* **1991**, *254* (5035), 1178–1181. https://doi.org/10.1126/science.1957169.
(7) Zysk, A. M.; Nguyen, F. T.; Oldenburg, A. L.; Marks, D. L.; Boppart, S. A. Optical Coherence Tomography: A Review of Clinical Development from Bench to Bedside. *J Biomed Opt* **2007**, *12* (5), 051403. https://doi.org/10.1117/1.2793736.
(8) Kut, C.; Chaichana, K. L.; Xi, J.; Raza, S. M.; Ye, X.; McVeigh, E. R.; Rodriguez, F. J.; Quinones-Hinojosa, A.; Li, X. Detection of Human Brain Cancer Infiltration Ex Vivo and in Vivo Using Quantitative Optical Coherence Tomography. *Sci Transl Med* **2015**, *7* (292), 292ra100. https://doi.org/10.1126/scitranslmed.3010611.

(9) Tao, Y. K.; Shen, D.; Sheikine, Y.; Ahsen, O. O.; Wang, H. H.; Schmolze, D. B.; Johnson, N. B.; Brooker, J. S.; Cable, A. E.; Connolly, J. L.; Fujimoto, J. G. Assessment of Breast Pathologies Using Nonlinear Microscopy. *PNAS* **2014**, *111* (43), 15304–15309. https://doi.org/10.1073/pnas.1416955111.
(10) Sanai, N.; Eschbacher, J.; Hattendorf, G.; Coons, S. W.; Preul, M. C.; Smith, K. A.; Nakaji, P.; Spetzler, R. F. Intraoperative Confocal Microscopy for Brain Tumors: A Feasibility Analysis in Humans. *Operative Neurosurgery* **2011**, *68* (suppl_2), ons282–ons290.
(11) Stummer, W.; Novotny, A.; Stepp, H.; Goetz, C.; Bise, K.; Reulen, H. J. Fluorescence-Guided Resection of Glioblastoma Multiforme Utilizing 5-ALA-Induced Porphyrins: A Prospective Study in 52 Consecutive Patients. *Journal of neurosurgery* **2000**, *93* (6), 1003–1013.
(12) Stummer, W.; Pichlmeier, U.; Meinel, T.; Wiestler, O. D.; Zanella, F.; Reulen, H.-J. Fluorescence-Guided Surgery with 5-Aminolevulinic Acid for Resection of Malignant Glioma: A Randomised Controlled Multicentre Phase III Trial. *The Lancet Oncology* **2006**, *7* (5), 392–401. https://doi.org/10.1016/S1470-2045(06)70665-9.
(13) Sanai, N.; Snyder, L. A.; Honea, N. J.; Coons, S. W.; Eschbacher, J. M.; Smith, K. A.; Spetzler, R. F. Intraoperative Confocal Microscopy in the Visualization of 5-Aminolevulinic Acid Fluorescence in Low-Grade Gliomas: Clinical Article. *Journal of Neurosurgery* **2011**, *115* (4), 740–748. https://doi.org/10.3171/2011.6.JNS11252.
(14) Stummer, W.; Tonn, J.-C.; Goetz, C.; Ullrich, W.; Stepp, H.; Bink, A.; Pietsch, T.; Pichlmeier, U. 5-Aminolevulinic Acid-Derived Tumor FluorescenceThe Diagnostic Accuracy of Visible Fluorescence Qualities as Corroborated by Spectrometry and Histology and Postoperative Imaging. *Neurosurgery* **2014**, *74* (3), 310–320. https://doi.org/10.1227/NEU.0000000000000267.
(15) Moore, G. E. Fluorescein as an Agent in the Differentiation of Normal and Malignant Tissues. *Science* **1947**, *106* (2745), 130–131. https://doi.org/10.1126/science.106.2745.130-a.
(16) Lu, F.-K.; Basu, S.; Igras, V.; Hoang, M. P.; Ji, M.; Fu, D.; Holtom, G. R.; Neel, V. A.; Freudiger, C. W.; Fisher, D. E.; Xie, X. S. Label-Free DNA Imaging in Vivo with Stimulated Raman Scattering Microscopy. *PNAS* **2015**, *112* (37), 11624–11629. https://doi.org/10.1073/pnas.1515121112.
(17) Ji, M.; Orringer, D. A.; Freudiger, C. W.; Ramkissoon, S.; Liu, X.; Lau, D.; Golby, A. J.; Norton, I.; Hayashi, M.; Agar, N. Y. R.; Young, G. S.; Spino, C.; Santagata, S.; Camelo-Piragua, S.; Ligon, K. L.; Sagher, O.; Xie, X. S. Rapid, Label-Free Detection of Brain Tumors with Stimulated Raman Scattering Microscopy. *Science Translational Medicine* **2013**, *5* (201), 201ra119-201ra119. https://doi.org/10.1126/scitranslmed.3005954.
(18) Ji, M.; Lewis, S.; Camelo-Piragua, S.; Ramkissoon, S. H.; Snuderl, M.; Venneti, S.; Fisher-Hubbard, A.; Garrard, M.; Fu, D.; Wang, A. C.; Heth, J. A.; Maher, C. O.; Sanai, N.; Johnson, T. D.; Freudiger, C. W.; Sagher, O.; Xie, X. S.; Orringer, D. A. Detection of Human Brain Tumor Infiltration with Quantitative Stimulated Raman Scattering Microscopy. *Science Translational Medicine* **2015**, *7* (309), 309ra163-309ra163. https://doi.org/10.1126/scitranslmed.aab0195.
(19) Freudiger, C. W.; Min, W.; Saar, B. G.; Lu, S.; Holtom, G. R.; He, C.; Tsai, J. C.; Kang, J. X.; Xie, X. S. Label-Free Biomedical Imaging with High Sensitivity by Stimulated Raman Scattering Microscopy. *Science* **2008**, *322* (5909), 1857–1861. https://doi.org/10.1126/science.1165758.
(20) Ozeki, Y.; Umemura, W.; Otsuka, Y.; Satoh, S.; Hashimoto, H.; Sumimura, K.; Nishizawa, N.; Fukui, K.; Itoh, K. High-Speed Molecular Spectral Imaging of Tissue with

Stimulated Raman Scattering. *Nature Photonics* **2012**, *6* (12), 845–851. https://doi.org/10.1038/nphoton.2012.263.
(21) Saar, B. G.; Freudiger, C. W.; Reichman, J.; Stanley, C. M.; Holtom, G. R.; Xie, X. S. Video-Rate Molecular Imaging in Vivo with Stimulated Raman Scattering. *Science* **2010**, *330* (6009), 1368–1370. https://doi.org/10.1126/science.1197236.
(22) Cheng, J.-X.; Xie, X. S. *Coherent Raman Scattering Microscopy*; CRC Press, 2012.
(23) Fu, D.; Lu, F.-K.; Zhang, X.; Freudiger, C.; Pernik, D. R.; Holtom, G.; Xie, X. S. Quantitative Chemical Imaging with Multiplex Stimulated Raman Scattering Microscopy. *J. Am. Chem. Soc.* **2012**, *134* (8), 3623–3626. https://doi.org/10.1021/ja210081h.
(24) Liao, C.-S.; Wang, P.; Wang, P.; Li, J.; Lee, H. J.; Eakins, G.; Cheng, J.-X. Spectrometer-Free Vibrational Imaging by Retrieving Stimulated Raman Signal from Highly Scattered Photons. *Science Advances* **2015**, *1* (9), e1500738. https://doi.org/10.1126/sciadv.1500738.
(25) Fu, D.; Holtom, G.; Freudiger, C.; Zhang, X.; Xie, X. S. Hyperspectral Imaging with Stimulated Raman Scattering by Chirped Femtosecond Lasers. *J. Phys. Chem. B* **2013**, *117* (16), 4634–4640. https://doi.org/10.1021/jp308938t.
(26) Lu, F.-K.; Calligaris, D.; Olubiyi, O. I.; Norton, I.; Yang, W.; Santagata, S.; Xie, X. S.; Golby, A. J.; Agar, N. Y. R. Label-Free Neurosurgical Pathology with Stimulated Raman Imaging. *Cancer Res* **2016**, *76* (12), 3451–3462. https://doi.org/10.1158/0008-5472.CAN-16-0270.
(27) Freudiger, C. W.; Yang, W.; Holtom, G. R.; Peyghambarian, N.; Xie, X. S.; Kieu, K. Q. Stimulated Raman Scattering Microscopy with a Robust Fibre Laser Source. *Nature Photonics* **2014**, *8* (2), 153–159. https://doi.org/10.1038/nphoton.2013.360.
(28) Orringer, D. A.; Pandian, B.; Niknafs, Y. S.; Hollon, T. C.; Boyle, J.; Lewis, S.; Garrard, M.; Hervey-Jumper, S. L.; Garton, H. J. L.; Maher, C. O.; Heth, J. A.; Sagher, O.; Wilkinson, D. A.; Snuderl, M.; Venneti, S.; Ramkissoon, S. H.; McFadden, K. A.; Fisher-Hubbard, A.; Lieberman, A. P.; Johnson, T. D.; Xie, X. S.; Trautman, J. K.; Freudiger, C. W.; Camelo-Piragua, S. Rapid Intraoperative Histology of Unprocessed Surgical Specimens via Fibre-Laser-Based Stimulated Raman Scattering Microscopy. *Nature Biomedical Engineering* **2017**, *1* (2), 1–13. https://doi.org/10.1038/s41551-016-0027.
(29) Zhang, D.; Slipchenko, M. N.; Cheng, J.-X. Highly Sensitive Vibrational Imaging by Femtosecond Pulse Stimulated Raman Loss. *J. Phys. Chem. Lett.* **2011**, *2* (11), 1248–1253. https://doi.org/10.1021/jz200516n.
(30) Kobat, D.; Durst, M. E.; Nishimura, N.; Wong, A. W.; Schaffer, C. B.; Xu, C. Deep Tissue Multiphoton Microscopy Using Longer Wavelength Excitation. *Opt. Express, OE* **2009**, *17* (16), 13354–13364. https://doi.org/10.1364/OE.17.013354.
(31) Paoli, J.; Smedh, M.; Wennberg, A.-M.; Ericson, M. B. Multiphoton Laser Scanning Microscopy on Non-Melanoma Skin Cancer: Morphologic Features for Future Non-Invasive Diagnostics. *Journal of Investigative Dermatology* **2008**, *128* (5), 1248–1255. https://doi.org/10.1038/sj.jid.5701139.
(32) Galli, R.; Uckermann, O.; Andresen, E. F.; Geiger, K. D.; Koch, E.; Schackert, G.; Steiner, G.; Kirsch, M. Intrinsic Indicator of Photodamage during Label-Free Multiphoton Microscopy of Cells and Tissues. *PLOS ONE* **2014**, *9* (10), e110295. https://doi.org/10.1371/journal.pone.0110295.
(33) Zhang, D.; Slipchenko, M. N.; Leaird, D. E.; Weiner, A. M.; Cheng, J.-X. Spectrally Modulated Stimulated Raman Scattering Imaging with an Angle-to-Wavelength Pulse Shaper. *Opt. Express, OE* **2013**, *21* (11), 13864–13874. https://doi.org/10.1364/OE.21.013864.

(34) Fu, D. *Developing Novel Nonlinear Optical Contrast for Biomedical Imaging*; Princeton University, Series Ed.; 2009, 2009.
(35) He, R.; Xu, Y.; Zhang, L.; Ma, S.; Wang, X.; Ye, D.; Ji, M. Dual-Phase Stimulated Raman Scattering Microscopy for Real-Time Two-Color Imaging. *Optica, OPTICA* **2017**, *4* (1), 44–47. https://doi.org/10.1364/OPTICA.4.000044.
(36) Gareau, D. S. Feasibility of Digitally Stained Multimodal Confocal Mosaics to Simulate Histopathology. *JBO* **2009**, *14* (3), 034050. https://doi.org/10.1117/1.3149853.

Chapter 5. IMPROVED LABEL-FREE PATHOLOGY BY SRS MICROSCOPY

5.1 INTRODUCTION

The overarching purpose of intraoperative consultations for tumor surgeries is to obtain crucial information that informs surgical treatment. The tools currently employed include microscopic assessment of a submitted specimen through cytological preparations or cryosectioning and subsequent staining of the tissue by hematoxylin and eosin (H&E). The challenges of generating a diagnostically adequate H&E slide of cryosectioned tissue are organ-specific. In central nervous system specimens, the main challenge often results from limited sample size and general texture heterogeneity of the submitted tissue. In such cases, texture heterogeneity manifests itself as a freeze artefact - the diffuse or focal splitting of sections or cellular rarefaction resulting in loss of diagnostic information.[1] The presence of these artefacts in microscopic sections can result in misinterpretations and subsequent diagnostic pitfalls.[2]

In addition to the inherent challenges of cryosectioning, the location of the tumor can add complexity to management. One group of tumors that poses many challenges is skull base tumors which include meningiomas, pituitary adenomas, schwannomas, hemangiopericytomas, chordomas, various types of sarcomas, carcinomas, and metastases among other entities.[3] Skull base tumors face unique challenges due to their low occurrence, presence in deep locations, proximity to critical neurovascular structures, and extension beyond anatomic boundaries.[4] Accurate intraoperative tissue diagnosis is essential during skull base tumor surgery to maximize tumor removal, as a non-resected tumor can lead to recurrence, treatment failure, and overall poor outcome.[5] In particular, a rapid diagnosis during the removal of skull base tumors can help the

surgeon to choose how aggressive the resection should be. In addition, in some patients, a rapid diagnosis can help to delineate the margins of tumor resection. Additionally, there is an increasing need to preserve tissue from small pathology specimens for downstream molecular ancillary testing, and an intraoperative technique aimed at preserving tissue would be preferable in these cases.

Many advanced optical imaging techniques have been developed to detect neoplastic cells and to provide diagnostic information with varying degrees of success, including optical coherence tomography[6,7], confocal microscopy[8], two-photon fluorescence combined with second harmonic generation[9–11], Raman spectroscopy[12], and coherent Raman scattering (CRS) microscopy.[13] Among the previous work, CRS stands out amongst other imaging techniques as it provides both morphological and chemical information at a submicron resolution without any staining or chemical labels.[14] Two CRS methods have been established: coherent anti-Stokes Raman scattering (CARS) and stimulated Raman scattering (SRS). Both CARS and SRS use two pulse lasers (pump and Stokes) to excite intrinsic vibrational motions of molecules coherently and have been shown to be able to provide molecular contrasts that can aid cancer diagnosis.[13]

In particular, it was recently demonstrated that SRS microscopy could provide H&E equivalent information for pathologists to determine cancer subtypes, thereby offering the potential for replacing frozen sectioning as an intraoperative diagnostic tool.[15,16] Specifically, it has been shown that a two-color SRS imaging approach targeting the C–H transition of lipid and protein (Raman transition at 2850 cm^{-1} and 2930 cm^{-1}, respectively) allow direct visualization of cell nuclei. The resulting images can be recolored using linear dependence of the signal on lipid and protein content, allowing for a simple and very close simulation of H&E, i.e., stimulated Raman histology (SRH). Orringer *et al.* and Hollon *et al.* have tested the efficacy of SRS

microscopy as a potential intraoperative H&E staining alternative for cases including glial and metastatic neoplasms with 92% accuracy of tumor subtype determination as assessed by neuropathologists.[15,16] Another recent study using the same SRH approach further validated the visual comparison of SRH images to H&E as applied to gastrointestinal tract.[17] Other studies used two-color SRS images for cancer/non-cancer identification in laryngeal squamous cell carcinoma[18] and glioblastoma infiltration in the brain.[19] However, these studies did not provide pathologist evaluation of SRH or SRS two-color images for cancer subtype determination and thus are insufficient to validate SRS as an alternative to histology. Similar to SRS, CARS microscopy has also been explored for cancer diagnosis[20–22] based on chemical contrasts. Compared to SRH, CARS is further complicated by the presence of a non-resonant background[23–26], which prevents direct conversion of CARS images to H&E images. Adding additional chemical contrasts from second harmonic generation and two-photon fluorescence, it has been shown that multicolor images can be generated and provides useful diagnostic information.[27] However, whether pathologists can use these images to provide meaningful cancer diagnosis requires further investigation.

While a few studies have validated SRH in limited settings, it remains unclear whether SRH is generally applicable to a diverse set of tumor types encountered in daily pathology practice. Employing two Raman transitions targeting lipids and proteins to generate an H&E alternative works well for entities with higher cytoplasmic lipid content as can be expected in glial neoplasms. This is because the cytoplasmic lipid signals are a primary source of contrast to visualize cell nuclei. However, skull base tumors are inherently more complex because high protein and low lipid concentrations in the cytoplasm or the stromal matrix are common and can pose a challenge in visualizing nuclei. To explore the utility and limitations of SRH in complex tumors, we have

set out to conduct a more dedicated investigation of SRH application to skull base tumors. Additionally, we take a different approach from previous studies by focusing on the user (i.e., pathologist) in addition to SRH validation. With only a few publications testing the accuracy of diagnosing histological subtypes[15,16], we emphasize assessment of how SRH performs at every step of the typical diagnostic workflow. Moreover, unlike previous studies, instead of training pathologists with SRH images, diagnosis in this study is performed without prior training and thus provides an unbiased assessment of the diagnostic accuracy achievable in an intraoperative setting. We used a simultaneous two-channel SRS imaging method we and others have developed to enable rapid SRH assessment.[28,29] Specifically, we performed simultaneous two-channel acquisition by using two 90° phase shifted Stokes pulses for orthogonal lock-in detection. This approach allows us to acquire protein and lipid SRS images rapidly for large pieces of tissue by eliminating wavelength switching and sequential acquisition. We image fresh resected tumor tissue collected prospectively during intraoperative consultation and validate the diagnostic capability of SRH through modularized review by board-certified neuropathologists. Our results reveal that SRH is effective in most cases with 87% accuracy relative to H&E stained formalin-fixed paraffin-embedded (FFPE) sections. Moreover, we find that in cases with limited lipid signal to provide the necessary contrast for nuclei visualization, rendering diagnosis is challenging when using strictly SRH, and it can be significantly improved with SRS chemical information.

5.2 METHODS

5.2.1 *Tissue Collection and Preparation*

Sixteen subjects undergoing operations for skull base tumors were recruited with the approval of the University of Washington Institutional Review Board over the course of 12 months, and all

research was performed in accordance with relevant guidelines and regulations. Subject eligibility was determined during preoperative evaluation by the neurosurgeon (L.N.S.) participating in this study, and written informed consent was obtained from each subject before surgery. At the time of standard intraoperative frozen section consultation, a fresh tissue sample measuring $0.3 \times 0.2 \times 0.1$ cm on average was allocated for this study. Each piece of fresh and unlabeled tumor sample was placed on a well depression glass slide, moistened with saline and covered with a coverslip in preparation for SRS imaging. Following SRS imaging, each sample was placed in neutrally buffered formalin, processed, and embedded in paraffin for permanent sections. Samples were then sectioned and stained with H&E for standard histopathological analysis. All SRS images with corresponding FFPE sections stained with H&E of skull base tumors were reviewed by a board-certified neuropathologist (G.J-S.), who selected representative portions of SRS images for histological analysis. Slides of frozen sections or cytological preparations performed at the time of intraoperative consultation from all studied cases were also reviewed in this study in order to compare the quality of SRS images with standard intraoperative techniques and to determine the diagnostic utility of SRS microscopy.

5.2.2 *SRS Microscopy*

Figure 5.1A depicts simultaneous two-color SRS that was employed in our study.[28,29] Briefly, the Stokes and pump pulses provided by the fixed (1040 nm center wavelength, <200 fs, >1.5 W) and tunable (798 nm center wavelength, <150 fs, 1.0 W) outputs, respectively, of a dual-output oscillator (Insight DS+, SpectraPhysics) with a repetition rate of 80 MHz. The Stokes pulse was modulated at 20 MHz using an electro-optic modulator (EOM) and split into two separate arms, one of which was then delayed by 12.5 ns (1/80 MHz) relative to the other. The two arms were recombined using a 50:50 beamsplitter and stretched to 2 ps using a grating-based pulse

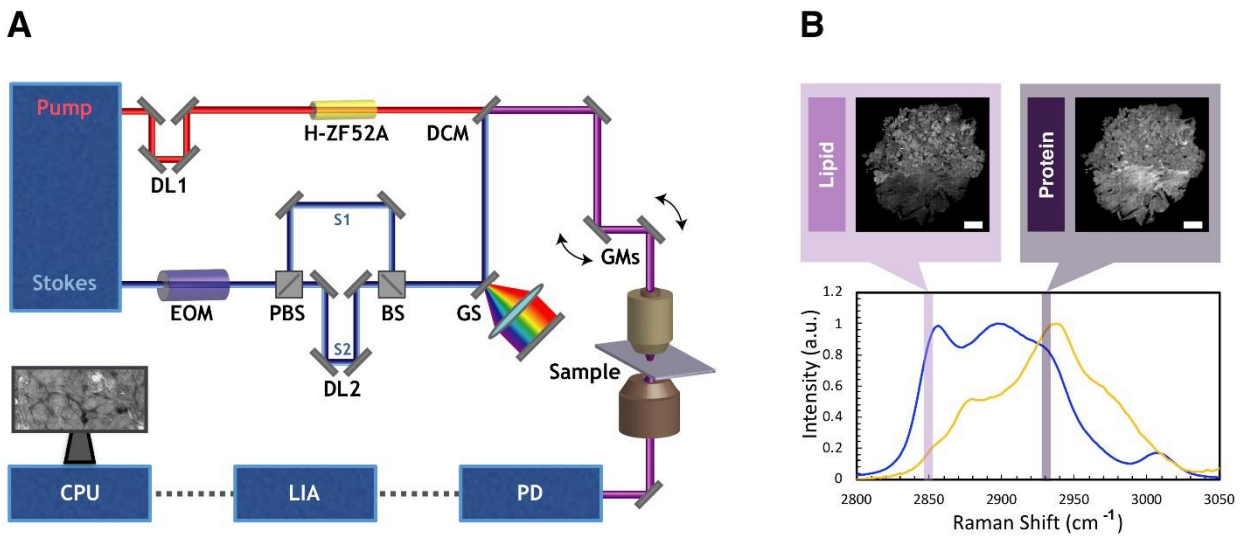

Figure 5.1. Experimental set up for SRS microscope and controls for lipid and protein channels. (A) The Stokes laser is modulated by an electro-optical modulator (EOM) at 20MHz. Tunable laser is spectrally dispersed through glass rods (tunable) and Stokes laser is dispersed through a grating stretcher (GS). They are the spatially and temporally overlapped at a dichroic mirror (DCM) and directed onto a pair of galvanomirrors (GM). The beams are then sent through a laser scanning microscope with a 25x water immersion objective. The pump beam after the condenser is detected by a photodiode (PD). The signal is processed through lock-in amplifier (LIA). Te images are collected using ScanImage on computer processing unit (CPU). (B) SRS spectra for oleic acid and bovine serum albumin (BSA) as controls for lipids and proteins, respectively.

stretcher.[30,31] The tunable source was centered at 798 nm, and the pulses were dispersed using 60 cm of glass rods. The average spectral width is estimated to be 300 cm^{-1}.[31] The pump and Stokes beams were then combined with a dichroic mirror and overlapped temporally using a delay line in the tunable arm. The resulting beam was sent into a home-built laser scanning microscope. A 25X Olympus water immersion objective (NA = 1.05) was used to focus the beams onto the tissue sample. At the focus, the Stokes beams had an average power of 30 mW each, and the pump had an average power of 40 mW. After passing through the condenser, the Stokes beam was filtered out, and the pump reached a silicon photodiode. SRS signal was detected with a lock-in

amplifier. The two orthogonal output of the lock-in amplifier provided the simultaneous two-channel SRS signals for pseudo H&E rendering.[28] Figure 5.1B depicts examples of SRS spectra for oleic acid and bovine serum albumin (BSA) as controls for lipids and proteins respectively.

5.2.3 *Image Processing*

Figure 5.2 details how SRS images were processed into the pseudo-H&E images to be given to neuropathologists for analysis. The acquired lipid (Fig. 5.2A) and protein (Fig. 5.2B) images

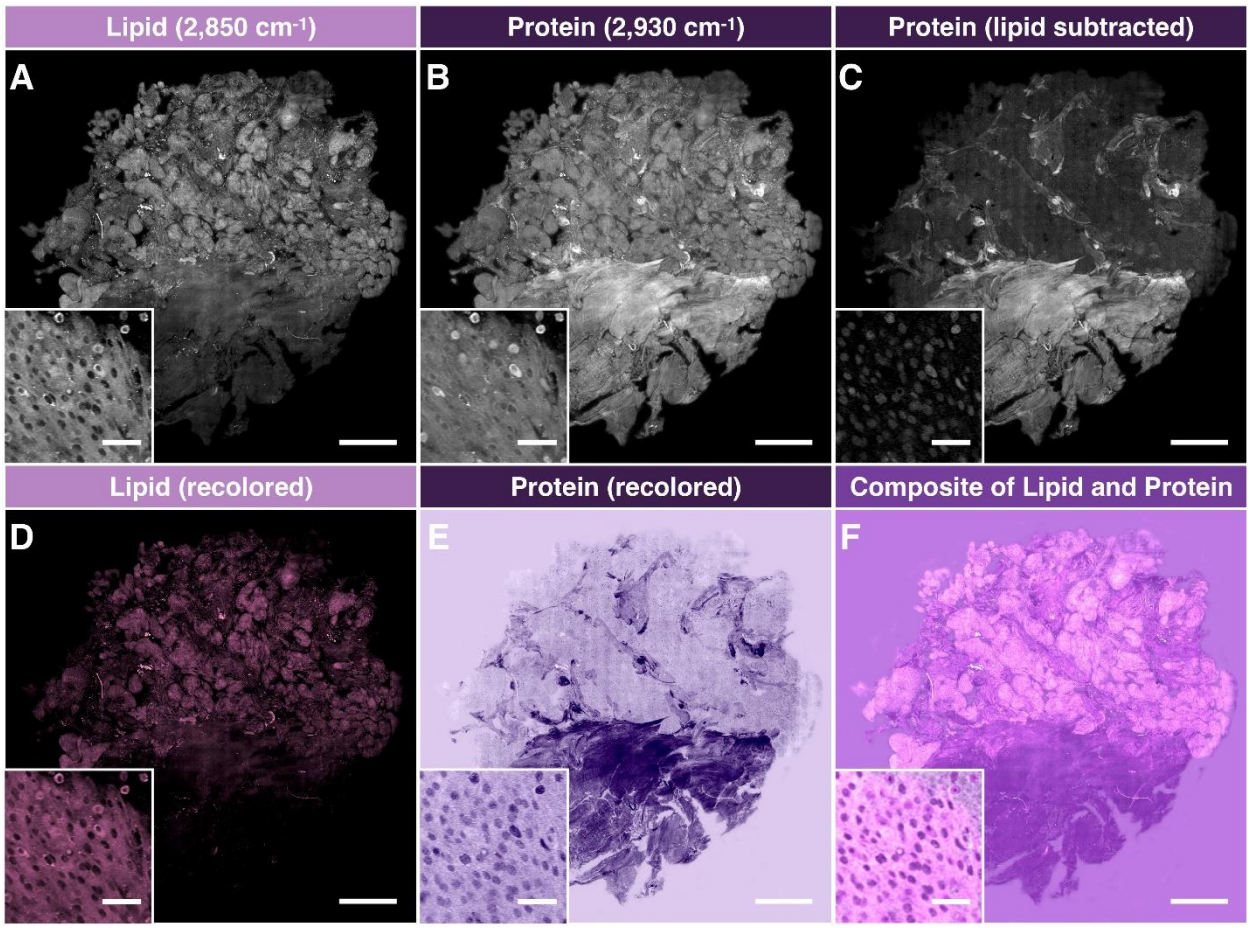

Figure 5.2. Image processing of stitched SRS imaging data (Meningioma, WHO grade I). (A) Stitched field normalized data for lipid channel. (B) Stitched field-normalized data for protein channel. (C) Lipid data subtracted from protein, utilizing lipid and protein images in (A,B). (D) Recoloring result of lipid data. (E) Recoloring result of protein data. (F) Composite image of (D,E). Whole tissue scale bar: 1mm. Inset scale bar: 50 μm.

(285 μm × 285 μm per frame) were field-normalized and stitched to recover a complete tissue image (2–6 mm in size). Subsequently, the lipid channel was subtracted from protein channel, as previously demonstrated, to generate lipid corrected protein image (Fig. 5.2C).[32] Using a custom-generated color scale in Image J, the lipid and lipid-corrected protein channels were recolored to match the conventional H&E (Figs. 5.2D and 5.2E) and combined to form a single image for histological analysis by pathologists (Fig. 5.2F).

5.2.4 *Survey Methodology*

A validation survey was conducted in order to establish the diagnostic utility of SRS simulated H&E images (SRH) compared to standard intraoperative pathology, which typically includes the frozen section and cytological preparation of the specimen routinely stained with H&E. The survey was performed by three neuropathologists (P.J.C., C.S.L., and L.F.G.-C.) who were blind to the diagnosis. They received a short clinical and radiographic summary of each case to mimic the circumstance of an intraoperative consultation but had no knowledge of SRS imaging and no training on SRH images. All sixteen studied cases were enrolled in the survey, which consisted of three phases: 1. Review of SRS generated images (SRH); 2. Review of the H&E-stained FFPE sections of the same specimen, and; 3. Review of the H&E-stained frozen sections or cytological preparations performed at the time of the neoplasm extraction for intraoperative diagnosis. Each phase included a series of multiple-choice questions focused on neoplastic appearance (epitheliod, spindle cell, myxoid, chondroid, or other), architectural pattern (lobular, fascicular, glandular, nested, papillary, sheeting, or other), and nuclear shape (rounded, elongated, and other). After the initial assessment, the evaluators participated in the diagnostic interpretation of each case that included differential diagnosis (a list of neoplasms that fit the neoplasm description, architectural pattern, and nuclear shape they have assigned to the case in combination with a clinical and

radiographic summary provided) and final diagnosis. Finally, each participant was required to quantify their level of confidence in their diagnosis. The results of the survey were compared to the assessment by collaborating pathologist G.J.-S. (histopathological features and differential diagnosis) and the neuropathology report (final diagnosis).

5.2.5 *Statistical Analysis of Survey Data*

For each pathologist, percent agreement and Cohen's kappa (κ_C) were calculated while comparing each modality (SRH, H&E frozen, and H&E permanent) to the assessment by the collaborating pathologist G. J.-S. (histopathological features and differential diagnosis) and the neuropathology report (final diagnosis) for individual case using R software. Additionally, the relative accuracy as a ratio of SRH and H&E FFPE percent agreement was calculated for comparison of SRH to the golden standard of diagnosis. Fleiss' kappa (κ_F) was calculated to assess interpathologist reliability.

5.3 Results and Discussion

5.3.1 *SRH Images Provide Cytoarchitectural Visualization Necessary for Diagnosis*

For a pathologist, architectural and cytological features are necessary for the diagnostic process. We use a studied meningioma case in Fig. 5.3 as an example of cytoarchitectural visualization available with SRH images. The characteristic lobular architectural growth pattern of epithelioid cells is as apparent in SRS images as it would be at a lower magnification of H&E stained frozen or FFPE sections (Figs. 5.3A–5.3C). At high resolution, the SRH image shows clear cytomorphology such as round to oval nuclei with bland chromatin and inconspicuous nucleoli (Figs. 5.3G–I). Moreover, scattered intranuclear pseudoinclusions, common histological features identified in meningiomas, are also visualized on SRH (Fig. 5.3D). Identical histological features are present in concurrent frozen and concomitant FFPE sections (Figs. 5.3H and 5.3I).

Furthermore, sufficient cytomorphological features can be identified to determine other cell types. Figures 5.3D–5.3F show lipid-rich cells identified and marked by a red box as macrophages (confirmed by immunohistochemistry). While in the case of meningioma, these cells are not considered diagnostically essential, in the case of breast cancer, tumor-associated macrophages have been explored as a prognostic marker.[33,34]

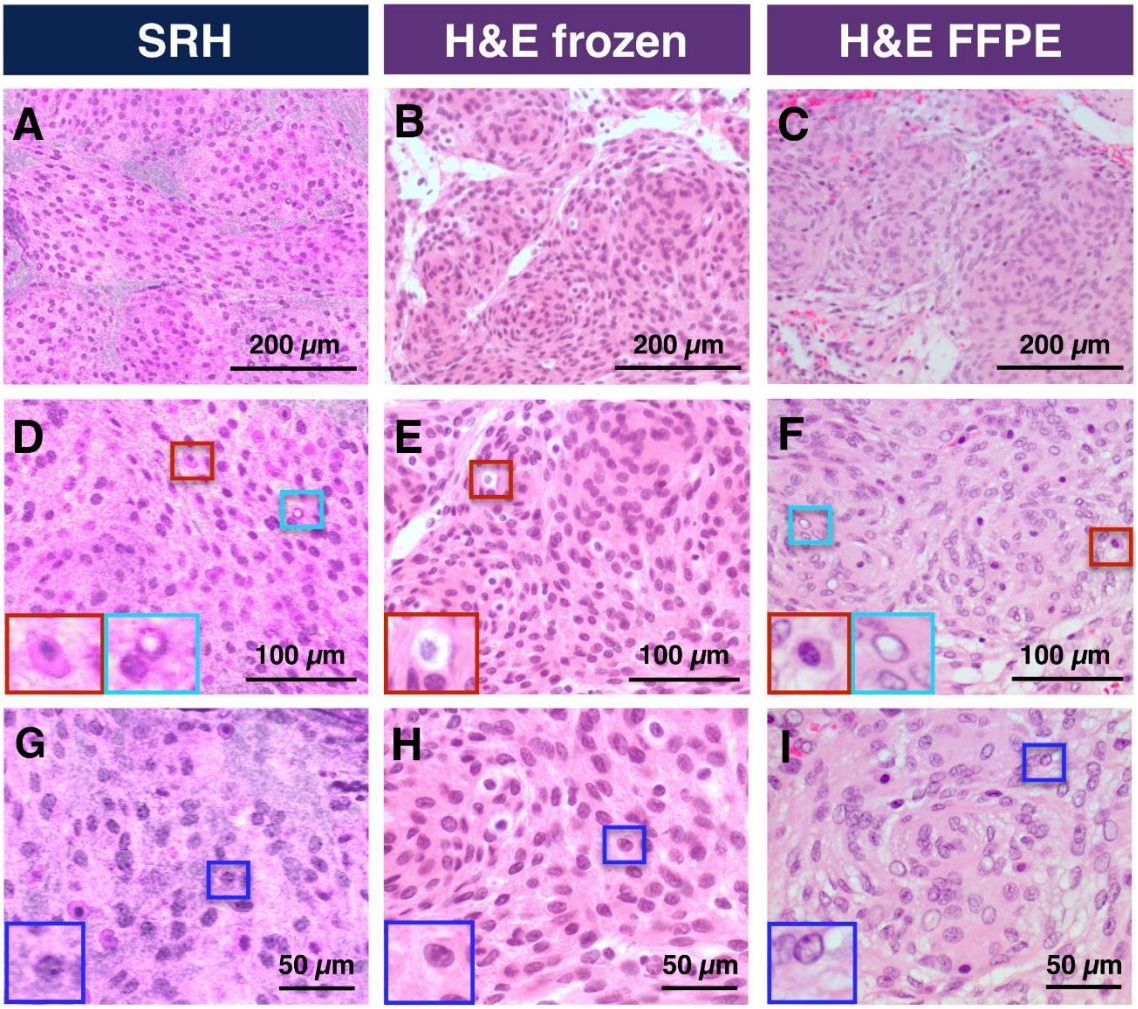

Figure 5.3. Comparison of cellular features available with SRH versus conventional H&E stained slides in representative case of Meningioma WHO grade I. (A–C) Comparison of architecture features. (D–F) Increased magnification highlighting macrophages (red box) verified by immunohistochemistry and intranuclear inclusions (cyan box). (G–I) Nuclear features with easily identifiable nucleolus (blue box).

5.3.2 *SRH Images Reveal Diagnostic Features in a Broad Range of Skull Base Tumors*

An accurate pathologist interpretation of unique histopathological features is essential during a neurosurgical procedure. For SRH to be applicable in an intraoperative setting, SRH must deliver clear and easy to interpret images with sufficient information. To examine the capability of SRH at providing useful histopathological information, we image a broad range of skull base tumors including nine meningiomas, three schwannomas, one chordoma, one chondrosarcoma, one pituitary adenoma, and one papillary craniopharyngioma. Figure 5.4 highlights typical diagnostic features of selected skull base tumors captured by SRH in comparison with H&E stained frozen sections of the same case and H&E stained FFPE sections of the same tissue.

The advantage of SRH is the ability to image the sample without sectioning, which eliminates challenges introduced by freeze artefact from cryosectioning. This issue is exacerbated when tissue samples are challenging to cut due to the heterogeneity of texture. The three cases that serve as an example (meningioma, chordoma, and chondrosarcoma) are shown Fig. 5.4. Figures 5.4A, 5.4G, and 5.4J demonstrate well-preserved diagnostic features in SRH images for meningioma, chordoma, and chondrosarcoma, respectively. In contrast, Figs. 5.4B, 5.4H, and 5.4K show corresponding H&E stained frozen sections distorted by freeze artefact. FFPE sections providing a reference for the typical appearance of histological features are shown in Fig. 5.4C, 5.4I, and 5.4L.

In the case of meningioma, the texture heterogeneity is caused by psammoma bodies (round collection of calcified material). This is a good example of the challenges faced when calcified material is present during cryosectioning. Psammoma bodies are diagnostically helpful when suspecting meningioma, which mitigates poor tissue preservation in this case specifically. On the other hand, conserving features in case of chordoma and chondrosarcoma is important for

accurate identification. Figures 5.4G and 5.4I show chordoma with vague small clusters and individual epithelioid cells with pale vacuolated cytoplasm (physaliphorous cells) and prominent dense extracellular protein-rich myxoid matrix that are missing in frozen section images. Similarly, one studied chondrosarcoma (low-grade per neuropathology report) demonstrated scattered mononucleated neoplastic cells in lacunae found in an abundant cartilaginous protein-rich background (Figs. 5.4J and 5.4L). These three examples highlight SRH advantage over the conventional frozen section in preventing loss of cytoarchitecture due to the extensive freeze artefact and tissue texture heterogeneity. When freeze artefacts are not a significant issue, the diagnosis on frozen section analysis can still be challenging due to ambiguous histomorphology in spindle neoplasms including schwannoma (Figs. 5.4D–5.4F) and meningioma without psammoma bodies (Fig. 5.3). With SRH, the different recoloring scheme can be used to highlight those features as will be discussed later. Additionally, because SRH is non-destructive, any imaged tissue can be saved for downstream histopathological analysis, and it is a significant advantage in cases where there is limited tissue.

In other studied types of tumors, similar morphological features found typically in FFPE sections are sufficiently replicated in SRH. For example, SRH of studied pituitary adenoma reveals sheets of relatively monotonous neuroendocrine cells with a moderate amount of cytoplasm and rounded nuclei with bland and occasionally stippled chromatin, depicted in Fig. 5.4M. These histological features agree well with those observed in a concomitant H&E-stained FFPE section (Fig. 5.4O) as well as concurrent cytological preparation (Fig. 5.4N). Additionally, our study includes a craniopharyngioma, a squamous epithelial neoplasm characterized by cauliflower-like papillary structures and fibrovascular core, which are visible on SRH image (Fig. 5.4P), FFPE (Fig. 5.4R), and corresponding frozen sections stained with H&E (Fig. 5.4Q).

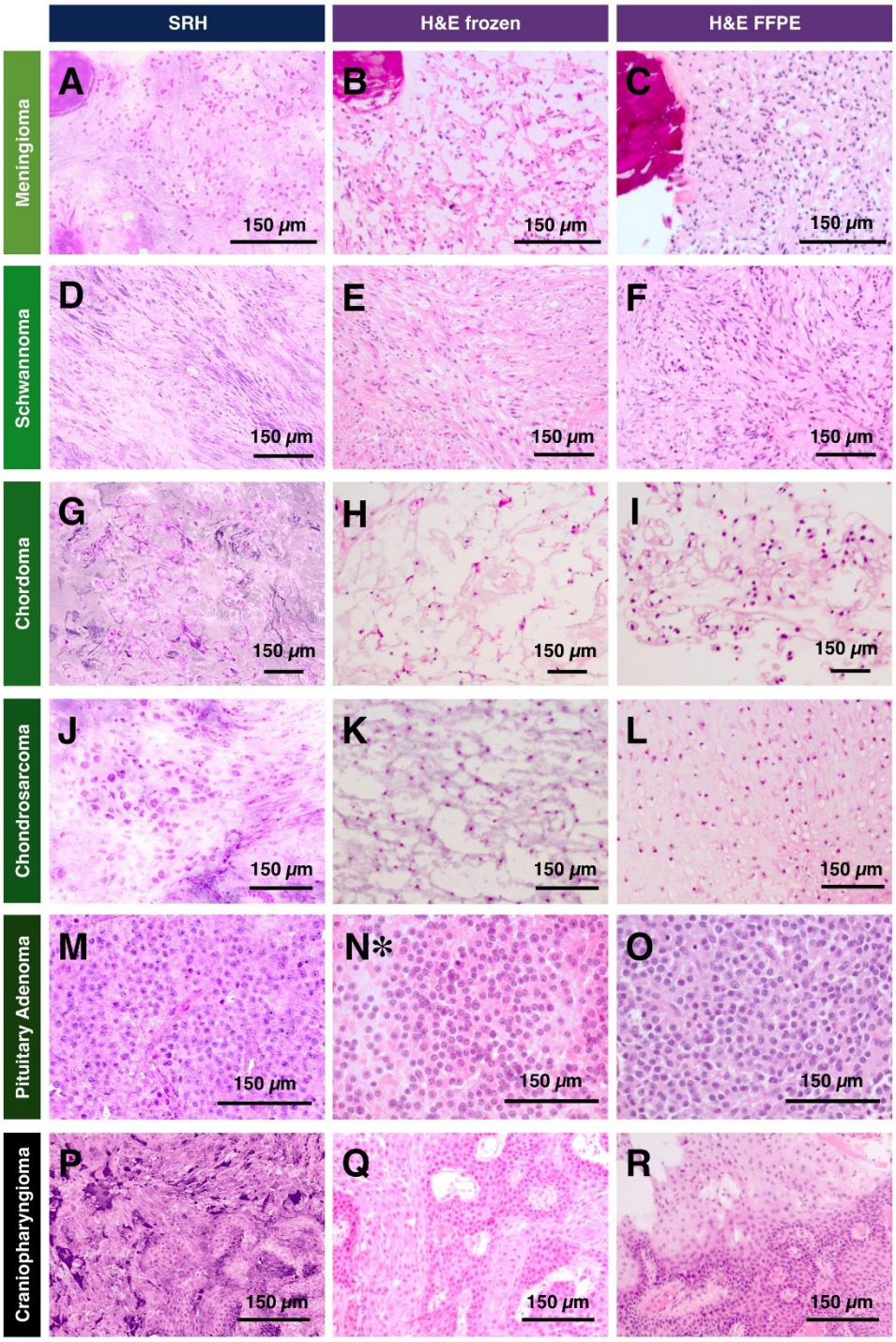

Figure 5.4. Comparison of SRH with conventional histological preparations of skull base tumors. (A–C) Meningioma, WHO grade I. (D–F) Schwannoma, WHO grade I. (G–I) Chordoma. (J–L) Chondrosarcoma, grade 2. (M,N*,O) Sparsely granulated somatotroph adenoma. (P–R) Papillary craniopharyngioma (BRAF-mutant). Case warranted cytological preparations only during intraoperative consultation.

Finally, SRH provides information on chromatin appearance, which can be used as evidence of preoperative treatment such as embolization. Preoperative endovascular embolization, adjunctive treatment of meningioma, was performed in 5 out of 9 studied meningiomas, and in one studied case resulted in noticeable cytomorphological changes captured on SRH (Figure 5.5), including the vague architectural structure and neoplastic cells with pyknotic nuclei (Fig. 5.4A). These histopathological features were also identified on both conventional H&E-stained FFPE sections of the same specimen and corresponding frozen sections (Figs. 5.4B and 5.4C). To contrast, a meningioma case without prior embolization discussed earlier can be referenced (Figs. 5.3 and 5.5).

Qualitative comparison of SRH images to H&E stained frozen sections shows that SRH offers an advantage over frozen section by avoiding diagnostic pitfalls due to freeze artefact. The pseudo-H&E recolored SRS images offer comparable diagnostic features that are available in H&E stained FFPE with the advantage of being non-destructive and preserving tissue for downstream diagnostic tests.

5.3.3 *Diagnostic Accuracy of SRH Images Compared to Conventional H&E Based Techniques*

In order to establish the diagnostic utility of SRH, we administer a survey which assesses the interaction of a given neuropathologist with SRH, H&E stained frozen, and FFPE section slides. Unlike previous studies[15,16], our survey included modularized assessment of the pathologist experience with SRH testing beyond final diagnostic accuracy. Typically, a pathologist uses histopathological features including neoplasm description, architectural pattern, and nuclear shape, among others in combination with clinical history and neoplasm location to progress from differential diagnosis to the final diagnosis. Because the generation of the final diagnosis is

involved, we benefit from understanding what histopathological features were discrepant on SRH. Moreover, we are comparing how H&E stained frozen, and FFPE sections perform in the same situation as SRH to isolate quality drawbacks of SRH from possible pathologist variability inherent to the diagnostic process. Table 1 shows a summary of our survey findings. The percent agreement highlights the absolute proportion of cases that agree with the collaborating pathologist G. J.-S. (histopathological features and differential diagnosis) and the neuropathology report (final diagnosis). Concordance based on Cohen's kappa (κ_C), is also reported. Interpathologist reliability is assessed using Fleiss's kappa (κ_F). To limit the impact of interpathologist variation, we report a relative accuracy defined as a ratio of SRH percent agreement and H&E FFPE to highlight the performance of SRH relative to the gold standard.

Overall, the SRH percent agreement for histopathological features is approximately the same as the percent agreement for FFPE and frozen sections between neuropathologists. However, the interpathologist reliability for SRH is consistently lower within a given histopathological feature. These findings could be explained by the fundamental difference of tissue handling in SRH as measurements are conducted on fresh tissue and the final appearance of cellular features as well as tissue architecture could be slightly different when compared to frozen and FFPE. Additionally, the inherent differences in color scale between SRH and H&E stained sections could affect the assessment of the architectural growth pattern. For example, the myxoid and chondroid architectural growth patterns are not visualized sufficiently, as supported by our survey, on SRH due to the proteinaceous background being recolored darker than what is found typically on H&E. Despite the possible shortcomings of SRH when evaluating individual histopathological features, the differential diagnosis was developed successfully (average of 94%, Table 5.1).

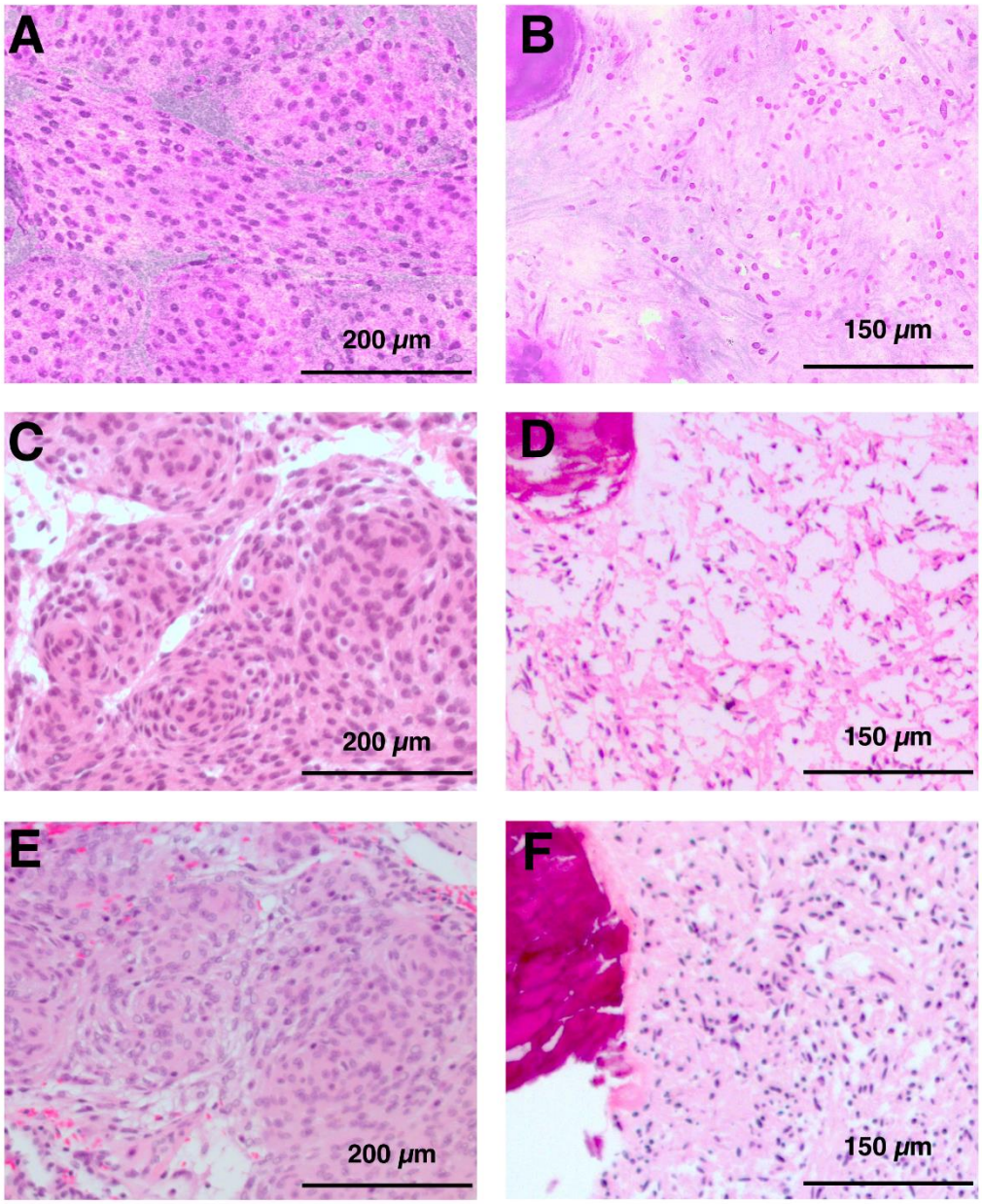

Figure 5.5. Comparison of meningioma with and without preoperative endovascular embolization treatment. A) SRH of meningioma case without preoperative embolization. B) SRH of meningioma case with preoperative embolization. C) H&E stained frozen section of meningioma case without preoperative embolization. D) H&E stained frozen section of meningioma case with preoperative embolization. E) H&E stained FFPE section of meningioma case without preoperative embolization. F) H&E stained FFPE section of meningioma case with preoperative embolization.

Using the histopathological features and clinical history, as mentioned above, the neuropathologist narrowed down the differential diagnosis to the final diagnosis with an average percent agreement of 81% (Table 5.1). Figure 5.6 shows a closer look at the cases used in the assessment and specifically what cases received the discrepant diagnoses. Based on our evaluation, we find two tumor types that are most prone to discrepancies in the final diagnosis when using SRH images: schwannoma and chondrosarcoma (Fig. 5.6D). In the case of chondrosarcoma, only one of the three neuropathologists include the entity on their differential diagnosis. One plausible cause for this is the component composition of this tumor type. Chondroid neoplastic cells produce

Table 5.1. Survey results, comparing SRH versus conventional tissue processing and staining. Relative accuracy is calculated as ratio of SRH percent agreement and H&E FFPE. Confidence score is assigned as follows: 4 - highly confident, 3 - confident, 2 - somewhat confident, 1 - not at all confident.

	Neuropathologist 1			**Neuropathologist 2**			**Neuropathologist 3**			**Interpathologist reliability (κ_F)**		
	SRH	**H&E frozen**	**H&E FFPE**	**SRH**	**H&E frozen**	**H&E FFPE**	**SRH**	**H&E frozen**	**H&E FFPE**	**SRH**	**H&E frozen**	**H&E FFPE**
Neoplasm Description:												
Percent Agreement	88%	88%	88%	75%	88%	81%	75%	75%	75%			
Concordance (κ_c)	0.78	0.80	0.80	0.52	0.78	0.66	0.61	0.56	0.59	0.48	0.78	0.63
Relative Accuracy	**100%**	—	—	**92%**	—	—	**100%**	—	—			
Architectural Pattern:												
Percent Agreement	75%	75%	75%	69%	88%	81%	44%	56%	50%			
Concordance (κ_c)	0.64	0.65	0.65	0.58	0.83	0.74	0.34	0.48	0.43	0.28	0.38	0.41
Relative Accuracy	**100%**	—	—	**85%**	—	—	**88%**	—	—			
Nuclear Shape:												
Percent Agreement	94%	100%	94%	94%	94%	94%	88%	94%	94%			
Concordance (κ_c)	0.87	1.00	0.86	0.86	0.86	0.86	0.73	0.86	0.86	0.64	0.91	0.82
Relative Accuracy	**100%**	—	—	**100%**	—	—	**93%**	—	—			
Differential:												
Percent Agreement	94%	100%	100%	94%	100%	100%	94%	100%	100%			
Concordance (κ_c)	0.90	1.00	1.00	0.90	1.00	1.00	0.90	1.00	1.00	—	—	—
Relative Accuracy	**94%**	—	—	**94%**	—	—	**94%**	—	—			
Final Diagnosis:												
Percent Agreement	88%	94%	100%	75%	94%	81%	81%	100%	94%			
Concordance (κ_c)	0.80	0.90	1.00	0.61	0.90	0.68	0.66	1.00	0.90	0.57	0.87	0.79
Relative Accuracy	**88%**	—	—	**85%**	—	—	**87%**	—	—			
Confidence score	***3.13***	***3.50***	***3.50***	***2.31***	***2.81***	***3.31***	***2.94***	***3.63***	***3.56***			

a cartilaginous matrix low in lipid content with occasional intracytoplasmic hyaline globules in lower grade tumors. Because both the cartilaginous matrix and hyaline globules will have SRS signal in the protein channel with minimal lipid content for additional contrast, chondrosarcoma cases can be challenging to diagnose using SRH (Fig. 5.4J). Such an issue is mainly due to the requirement of having to match the H&E color scheme.

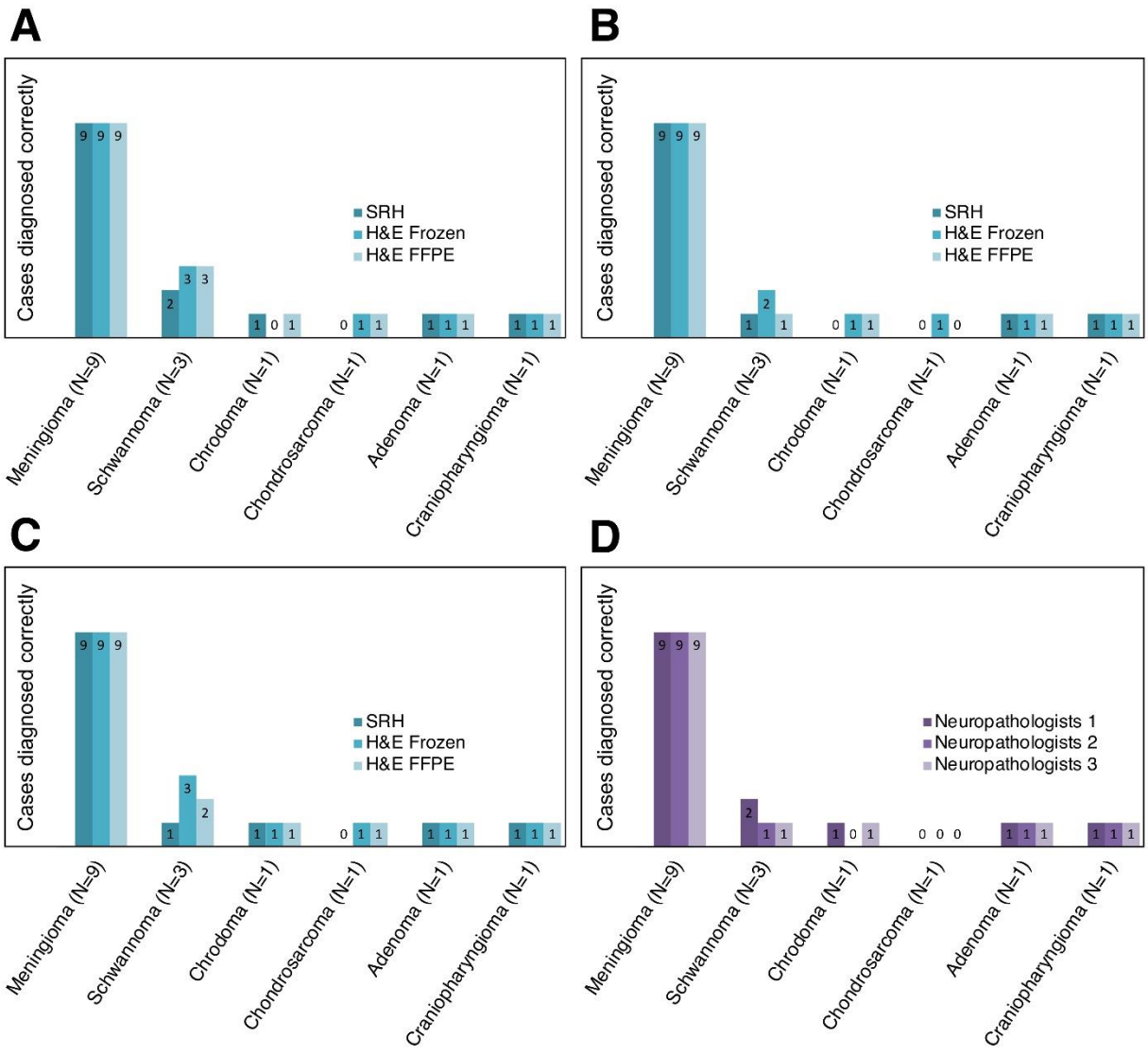

Figure 5.6. Depiction of correctly diagnosed cases for each neuropathologist and modality. (A–C) Neuropathologist 1, 2, and 3, respectively. (D) SRH only comparison for all neuropathologists.

For the case of schwannomas, we have found that neuropathologists frequently qualify their decision when arriving at a final diagnosis for spindle cell tumors such as meningioma and schwannoma. For all neuropathologists, the differential diagnosis for such cases is correct. Pathologists may remain cautious with final diagnoses during intraoperative consultations, explaining that spindle cell neoplasm can be either schwannoma or meningioma, with the understanding that differentiation between those two entities will not have a significant impact on the immediate surgical management. In such cases, the final classification can be deferred to FFPE sections where additional histological examination and ancillary stains performed as needed can provide the necessary information to arrive at a definitive diagnosis.

Finally, SRH provides enough information for a neuropathologist to render the final diagnosis with an average percent agreement of 81% and relative accuracy of 87% (Table 5.1). The neuropathologist rated confidence score correlates with percent agreement. This correlation is expected as the more confident a neuropathologist feels using SRH images, the more accurate their diagnosis is expected to be. Although the objective of our study was to see how SRH performs without the use of training data sets, it is relevant to highlight that slight differences between SRH and conventional H&E staining impacts confidence and, by extension, diagnostic accuracy. This issue could be mitigated with SRH interpretation training that would be necessary for clinical application of SRH.

5.3.4 *Additional Chemical Information Improves Diagnosis of SRH*

After evaluating the types of tumors that are discrepant on SRH images, we identified that low stromal lipid concentration (as in the case of chondrosarcoma) could be challenging for pseudo-H&E recoloring. In conventional H&E staining, hematoxylin preferentially stains nucleic acids dark purple, highlighting nuclear features, whereas eosin stains protein content various shades of

pink and red. Pseudo recoloring used in SRH relies on contrast from lipid and protein to recolor protein signal purple, enabling clear visualization of the nucleus. However, the requirement to pseudo-H&E recolor SRS images in SRH limits how chemical information from SRS is presented, which underutilizes the differences in protein and lipid in stromal or cytoplasmic components. The information on lipids is not available in conventional H&E.

Although this study is focused on evaluating the diagnostic utility of SRH, it is important to emphasize that protein and lipid information from SRS is available to augment the use of SRH in intraoperative consultation. This can be exemplified in two different cases. Firstly, the studied

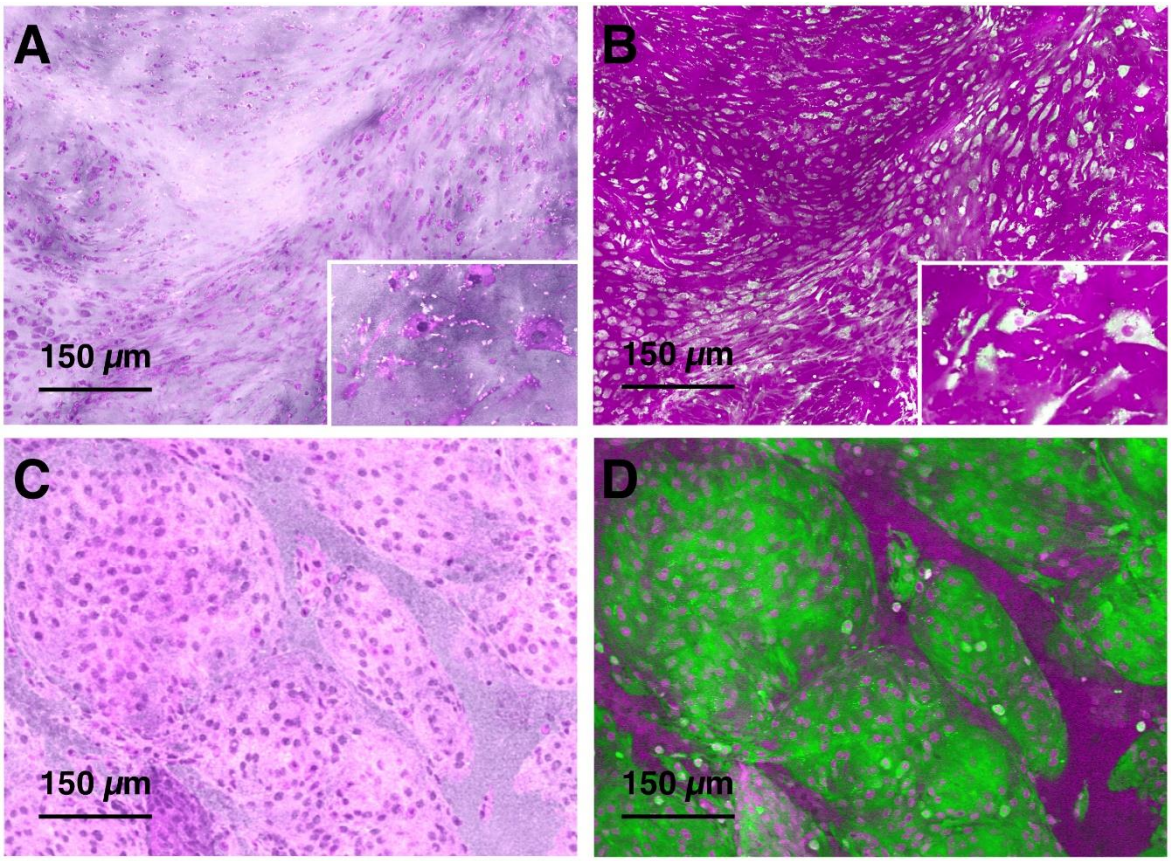

Figure 5.7. Chondrosarcoma versus meningioma. (A) Pseudo-H&E recolored SRH of chondrosarcoma case. (B) Lipid (green) and protein (magenta) SRS of chondrosarcoma case. (C) Pseudo-H&E recolored SRH of meningioma case. (D) Lipid (green) and protein (magenta) SRS of meningioma case.

chondrosarcoma case was misclassified as meningioma due to perceived similarities on SRH (Figs. 5.7A and 5.7C). However, direct analysis of the protein and lipid SRS images of SRS recolored in magenta and green (Fig. 5.7D versus 5.7B) shows a high lipid signal in the case of meningioma, while in chondrosarcoma, the supporting cartilaginous matrix is protein-rich. The SRS-based data matches the general knowledge that chondrosarcoma cells can be found in a matrix that is predominantly cartilage, made almost exclusively of protein. Information provided by SRS can thus facilitate a confident diagnosis of chondrosarcoma.

Secondly, the occasional challenge of differentiating meningioma and schwannoma cases can be overcome with SRS lipid and protein information without having to resort to immunohistochemistry staining. In schwannoma, the collagen fibers often are present between

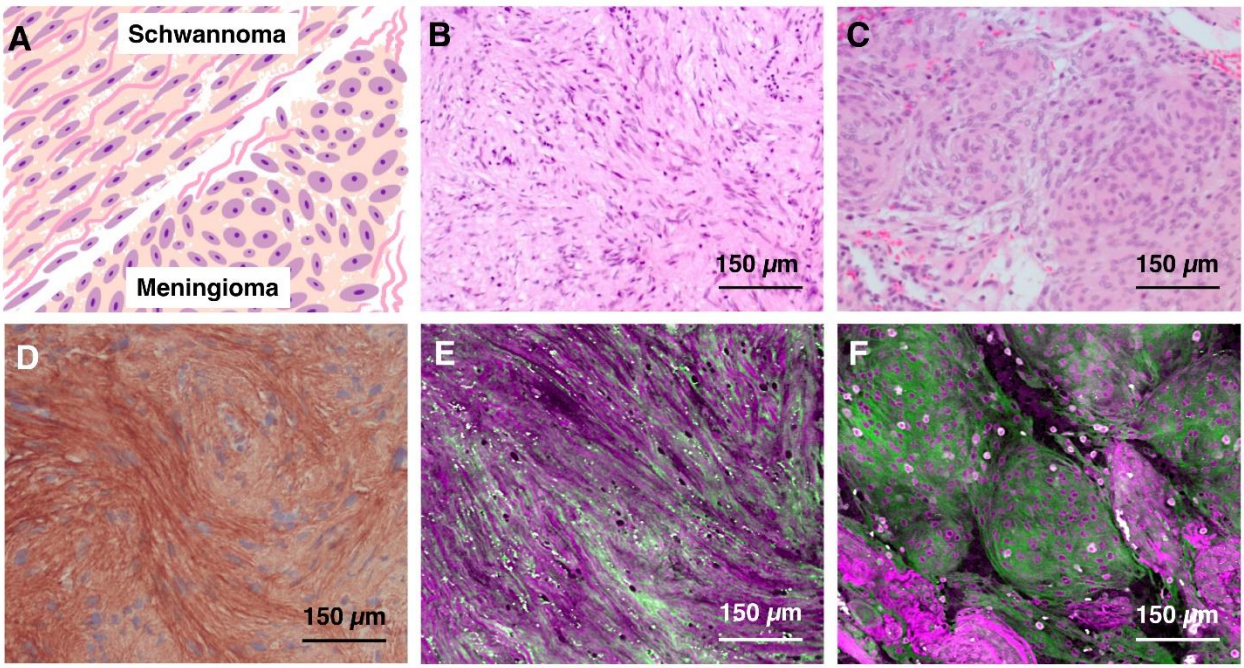

Figure 5.8. SRS images improve the identification of collagen. (A) Depiction of architectural and morphological differences between meningioma and schwannoma with particular focus on collagen fibers. (B) H&E of schwannoma. (C) H&E of meningioma. Protein signal is shown in magenta while lipid signal is shown as green. (D) Sample of collagen type IV antibody stained schwannoma case. (E) SRS based image of schwannoma. (F) SRS based image of meningioma.

neoplastic cells in contrast to meningioma, where the collagen fibers usually surround the group of neoplastic cells that can be found in a lobular pattern (Fig. 5.8A). These histological features are subtle when using H&E-stained FFPE sections (Figs. 5.8B and 5.8C) but can be distinguished with immunohistochemistry (Fig. 5.8D). To assist with the differentiation of meningioma from schwannoma using SRS, we can highlight collagen fibers using magenta (protein) and green (lipid) colors in combination with simple linear remapping that correlates the color intensity to the concentration of the constituent of interest. In addition to simulated H&E, the protein and lipid data contrasted in the new color scheme allows for more efficient highlighting of collagen fibers and determining whether they are present in between neoplastic cells (Fig. 5.8E) or are present around meningioma lobules (Fig. 5.8F), allowing us to separate schwannoma from meningioma.

In summary, we highlight in Figs. 5.7 and 5.8 that using the lipid and protein chemical information, a pathologist could better visualize the collagen fibers in schwannoma cases and discern collagenous matrix of chondrosarcoma from lipid-rich tumors such as meningioma respectively. Furthermore, the SRS ability to detect collagen fibers can be used as a surrogate for immunohistochemistry, which could improve the diagnostic process intraoperatively in addition to saving money on expensive antibody reagents.

5.4 Conclusion and Future Outlook

SRH has shown great promise in intraoperative diagnosis of a limited subset of neoplastic entities, particularly glial tumors. However, the broad utility of SRH and challenges it may face in more diverse tissue remain largely unknown. Furthermore, the evaluation of the diagnostic accuracy conducted in previous studies has only focused on comparing SRH to H&E frozen sections and clinical diagnosis rendered intraoperatively.[15,16] However, the gold standard in surgical pathology is the use of H&E stained FFPE sections in combination with ancillary studies, including

immunohistochemistry, which requires time-consuming tissue processing as well as pathological interpretation. We address the gaps in testing SRH diagnostic capability using the reported original neuropathological diagnosis established for a given case and compare SRH to conventional modalities while accounting for interpathologist variability. In order to thoroughly assess the diagnostic utility of SRH, it is important to modularize the evaluation process to determine precisely the areas where SRH based technology needs improvement. We achieve that by assessing the efficacy at multiple steps on the way to final diagnosis as well as checking the neuropathologist confidence when using the new modality.

Taking our unique evaluation approach, we find that neuropathologists were able to establish a neoplasm description, architectural pattern, and nuclear shape with practically the same percent agreement as conventional modalities. Following the diagnostic process, we find that neuropathologists generate differential diagnosis successfully and final SRH diagnostic capability is very close to conventional modalities. In addition to demonstrating the diagnostic capabilities of SRH on this subset of tumors, we demonstrate supporting findings that SRS chemical information with lipid and protein can further help diagnostic process and possibly reduce the need of immunohistochemistry use in selected cases.

At the same time, one of the main challenges that the SRS technique is likely to face in broader organ applications is the reliance on lipid and protein contrast to visualize nuclear features which are important to render a pathological diagnosis. For many neoplastic entities, protein/lipid-based simulation of H&E works well. However, for situations where lipid is limited in the cytoplasm, or otherwise nearby stroma, a map of local protein concentration provided by SRS might not be sufficient for successful visualization of a nucleus and general cellular morphology. New recoloring schemes can be considered to mediate such a problem. Nuclear segmentation has

been reported in H&E stained slides, fluorescence images, and SRS images.[35–37] With nuclear segmentation, a separate recoloring technique can be employed. However, incorporating separate recoloring techniques must be generalized across different entities to reduce user variability and avoid inconsistent simulation of H&E. Such inconsistencies can prompt the pathologist to misclassify the type of neoplasm with a detrimental consequence to patients. Moreover, when designing new recoloring schemes, it is essential to use a consistent method without *a priori* knowledge of H&E as such knowledge would not be available in an intraoperative setting.

In conclusion, we have studied a diverse set of skull base tumors using fast simultaneous 2-channel SRS imaging and new pseudo-hematoxylin and eosin (H&E) recoloring methodology. Due to label-free non-destructive features of SRS technique, we demonstrated that most challenges with cryosectioning and limited amounts of fragile tissue during intraoperative consultation could quickly be addressed using SRS based approach. Using a diverse set of tumors, we determined the potential drawbacks of pseudo-H&E recoloring in selected cases involving insufficient nucleus visualization. While agreeing with previous work on SRS accuracy in intraoperative setting, we determined that SRS is capable of mostly matching the conventional H&E based technique and more importantly, providing additional diagnostically useful information. By following the diagnostic process that a pathologist uses, we discovered that pseudo-H&E recoloring, lipid/protein chemical information, and additional pathologist training to interpret this new information must be considered in tandem to bring SRS into clinical practice.

5.5 REFERENCES

(1) Powell, S. Z. Intraoperative Consultation, Cytologic Preparations, and Frozen Section in the Central Nervous System. *Archives of Pathology & Laboratory Medicine* **2005**, *129* (12), 1635–1652. https://doi.org/10.1043/1543-2165(2005)129[1635:ICCPAF]2.0.CO;2.
(2) Chatterjee, S. Artefacts in Histopathology. *Journal of Oral and Maxillofacial Pathology* **2014**, *18* (4), 111. https://doi.org/10.4103/0973-029X.141346.

(3) DN, L.; H, O.; OD, W.; WK, C. *WHO Classification of Tumours of the Central Nervous System*.
(4) Mazzoni, A.; Krengli, M. Historical Development of the Treatment of Skull Base Tumours. *Rep Pract Oncol Radiother* **2016**, *21* (4), 319–324. https://doi.org/10.1016/j.rpor.2014.12.001.
(5) Jaju, H. Unfavourable Results in Skull Base Surgery. *Indian J Plast Surg* **2013**, *46* (2), 239–246. https://doi.org/10.4103/0970-0358.118599.
(6) Nguyen, F. T.; Zysk, A. M.; Chaney, E. J.; Kotynek, J. G.; Oliphant, U. J.; Bellafiore, F. J.; Rowland, K. M.; Johnson, P. A.; Boppart, S. A. Intraoperative Evaluation of Breast Tumor Margins with Optical Coherence Tomography. *Cancer Res* **2009**, *69* (22), 8790–8796. https://doi.org/10.1158/0008-5472.CAN-08-4340.
(7) Kut, C.; Chaichana, K. L.; Xi, J.; Raza, S. M.; Ye, X.; McVeigh, E. R.; Rodriguez, F. J.; Quinones-Hinojosa, A.; Li, X. Detection of Human Brain Cancer Infiltration Ex Vivo and in Vivo Using Quantitative Optical Coherence Tomography. *Sci Transl Med* **2015**, *7* (292), 292ra100. https://doi.org/10.1126/scitranslmed.3010611.
(8) Bini, J.; Spain, J.; Nehal, K.; Hazelwood, V.; DiMarzio, C.; Rajadhyaksha, M. Confocal Mosaicing Microscopy of Human Skin Ex Vivo: Spectral Analysis for Digital Staining to Simulate Histology-like Appearance. *J Biomed Opt* **2011**, *16* (7). https://doi.org/10.1117/1.3596742.
(9) Tao, Y. K.; Shen, D.; Sheikine, Y.; Ahsen, O. O.; Wang, H. H.; Schmolze, D. B.; Johnson, N. B.; Brooker, J. S.; Cable, A. E.; Connolly, J. L.; Fujimoto, J. G. Assessment of Breast Pathologies Using Nonlinear Microscopy. *PNAS* **2014**, *111* (43), 15304–15309. https://doi.org/10.1073/pnas.1416955111.
(10) Giacomelli, M. G.; Faulkner-Jones, B. E.; Cahill, L. C.; Yoshitake, T.; Do, D.; Fujimoto, J. G. Comparison of Nonlinear Microscopy and Frozen Section Histology for Imaging of Mohs Surgical Margins. *Biomed. Opt. Express, BOE* **2019**, *10* (8), 4249–4260. https://doi.org/10.1364/BOE.10.004249.
(11) Cahill, L. C.; Giacomelli, M. G.; Yoshitake, T.; Vardeh, H.; Faulkner-Jones, B. E.; Connolly, J. L.; Sun, C.-K.; Fujimoto, J. G. Rapid Virtual H&E Histology of Breast Tissue Specimens Using a Compact Fluorescence Nonlinear Microscope. *Lab Invest* **2018**, *98* (1), 150–160. https://doi.org/10.1038/labinvest.2017.116.
(12) Jermyn, M.; Mok, K.; Mercier, J.; Desroches, J.; Pichette, J.; Saint-Arnaud, K.; Bernstein, L.; Guiot, M.-C.; Petrecca, K.; Leblond, F. Intraoperative Brain Cancer Detection with Raman Spectroscopy in Humans. *Sci Transl Med* **2015**, *7* (274), 274ra19. https://doi.org/10.1126/scitranslmed.aaa2384.
(13) Cicerone, M. T.; Camp, C. H. Histological Coherent Raman Imaging: A Prognostic Review. *Analyst* **2017**, *143* (1), 33–59. https://doi.org/10.1039/C7AN01266G.
(14) Cheng, J.-X.; Xie, X. S. Vibrational Spectroscopic Imaging of Living Systems: An Emerging Platform for Biology and Medicine. *Science* **2015**, *350* (6264). https://doi.org/10.1126/science.aaa8870.
(15) Orringer, D. A.; Pandian, B.; Niknafs, Y. S.; Hollon, T. C.; Boyle, J.; Lewis, S.; Garrard, M.; Hervey-Jumper, S. L.; Garton, H. J. L.; Maher, C. O.; Heth, J. A.; Sagher, O.; Wilkinson, D. A.; Snuderl, M.; Venneti, S.; Ramkissoon, S. H.; McFadden, K. A.; Fisher-Hubbard, A.; Lieberman, A. P.; Johnson, T. D.; Xie, X. S.; Trautman, J. K.; Freudiger, C. W.; Camelo-Piragua, S. Rapid Intraoperative Histology of Unprocessed Surgical Specimens via Fibre-Laser-

Based Stimulated Raman Scattering Microscopy. *Nature Biomedical Engineering* **2017**, *1* (2), 1–13. https://doi.org/10.1038/s41551-016-0027.
(16) Hollon, T. C.; Lewis, S.; Pandian, B.; Niknafs, Y. S.; Garrard, M. R.; Garton, H.; Maher, C. O.; McFadden, K.; Snuderl, M.; Lieberman, A. P.; Muraszko, K.; Camelo-Piragua, S.; Orringer, D. A. Rapid Intraoperative Diagnosis of Pediatric Brain Tumors Using Stimulated Raman Histology. *Cancer Res.* **2018**, *78* (1), 278–289. https://doi.org/10.1158/0008-5472.CAN-17-1974.
(17) Sarri, B.; Poizat, F.; Heuke, S.; Wojak, J.; Franchi, F.; Caillol, F.; Giovannini, M.; Giovannini, M.; Rigneault, H.; Rigneault, H. Stimulated Raman Histology: One to One Comparison with Standard Hematoxylin and Eosin Staining. *Biomed. Opt. Express, BOE* **2019**, *10* (10), 5378–5384. https://doi.org/10.1364/BOE.10.005378.
(18) Zhang, L.; Wu, Y.; Zheng, B.; Su, L.; Chen, Y.; Ma, S.; Hu, Q.; Zou, X.; Yao, L.; Yang, Y.; Chen, L.; Mao, Y.; Chen, Y.; Ji, M. Rapid Histology of Laryngeal Squamous Cell Carcinoma with Deep-Learning Based Stimulated Raman Scattering Microscopy. *Theranostics* **2019**, *9* (9), 2541–2554. https://doi.org/10.7150/thno.32655.
(19) Lu, F.-K.; Calligaris, D.; Olubiyi, O. I.; Norton, I.; Yang, W.; Santagata, S.; Xie, X. S.; Golby, A. J.; Agar, N. Y. R. Label-Free Neurosurgical Pathology with Stimulated Raman Imaging. *Cancer Res* **2016**, *76* (12), 3451–3462. https://doi.org/10.1158/0008-5472.CAN-16-0270.
(20) Evans, C. L.; Xie, X. S. Coherent Anti-Stokes Raman Scattering Microscopy: Chemical Imaging for Biology and Medicine. *Annu Rev Anal Chem (Palo Alto Calif)* **2008**, *1*, 883–909. https://doi.org/10.1146/annurev.anchem.1.031207.112754.
(21) Evans, C. L.; Xu, X.; Kesari, S.; Xie, X. S.; Wong, S. T. C.; Young, G. S. Chemically-Selective Imaging of Brain Structures with CARS Microscopy. *Opt. Express, OE* **2007**, *15* (19), 12076–12087. https://doi.org/10.1364/OE.15.012076.
(22) Meyer, T.; Bergner, N.; Medyukhina, A.; Dietzek, B.; Krafft, C.; Romeike, B. F. M.; Reichart, R.; Kalff, R.; Popp, J. Interpreting CARS Images of Tissue within the C–H-Stretching Region. *Journal of Biophotonics* **2012**, *5* (10), 729–733. https://doi.org/10.1002/jbio.201200104.
(23) Min, W.; Freudiger, C. W.; Lu, S.; Xie, X. S. Coherent Nonlinear Optical Imaging: Beyond Fluorescence Microscopy. *Annu Rev Phys Chem* **2011**, *62*, 507–530. https://doi.org/10.1146/annurev.physchem.012809.103512.
(24) Duboisset, J.; Berto, P.; Gasecka, P.; Bioud, F.-Z.; Ferrand, P.; Rigneault, H.; Brasselet, S. Molecular Orientational Order Probed by Coherent Anti-Stokes Raman Scattering (CARS) and Stimulated Raman Scattering (SRS) Microscopy: A Spectral Comparative Study. *J. Phys. Chem. B* **2015**, *119* (7), 3242–3249. https://doi.org/10.1021/jp5113813.
(25) Yu, Y.; Ramachandran, P. V.; Wang, M. C. Shedding New Light on Lipid Functions with CARS and SRS Microscopy. *Biochim. Biophys. Acta* **2014**, *1841* (8), 1120–1129. https://doi.org/10.1016/j.bbalip.2014.02.003.
(26) Bocklitz, T.; Meyer, T.; Schmitt, M.; Rimke, I.; Hoffmann, F.; von Eggeling, F.; Ernst, G.; Guntinas-Lichius, O.; Popp, J. Invited Article: Comparison of Hyperspectral Coherent Raman Scattering Microscopies for Biomedical Applications. *APL Photonics* **2018**, *3* (9), 092404. https://doi.org/10.1063/1.5030159.
(27) Bocklitz, T. W.; Salah, F. S.; Vogler, N.; Heuke, S.; Chernavskaia, O.; Schmidt, C.; Waldner, M. J.; Greten, F. R.; Bräuer, R.; Schmitt, M.; Stallmach, A.; Petersen, I.; Popp, J. Pseudo-HE Images Derived from CARS/TPEF/SHG Multimodal Imaging in Combination with

Raman-Spectroscopy as a Pathological Screening Tool. *BMC Cancer* **2016**, *16* (1), 534. https://doi.org/10.1186/s12885-016-2520-x.
(28) He, R.; Xu, Y.; Zhang, L.; Ma, S.; Wang, X.; Ye, D.; Ji, M. Dual-Phase Stimulated Raman Scattering Microscopy for Real-Time Two-Color Imaging. *Optica, OPTICA* **2017**, *4* (1), 44–47. https://doi.org/10.1364/OPTICA.4.000044.
(29) Francis, A.; Berry, K.; Chen, Y.; Figueroa, B.; Fu, D. Label-Free Pathology by Spectrally Sliced Femtosecond Stimulated Raman Scattering (SRS) Microscopy. *PLOS ONE* **2017**, *12* (5), e0178750. https://doi.org/10.1371/journal.pone.0178750.
(30) Lai, M.; Lai, S. T.; Swinger, C. Single-Grating Laser Pulse Stretcher and Compressor. *Appl. Opt., AO* **1994**, *33* (30), 6985–6987. https://doi.org/10.1364/AO.33.006985.
(31) Figueroa, B.; Fu, W.; Nguyen, T.; Shin, K.; Manifold, B.; Wise, F.; Fu, D. Broadband Hyperspectral Stimulated Raman Scattering Microscopy with a Parabolic Fiber Amplifier Source. *Biomed. Opt. Express, BOE* **2018**, *9* (12), 6116–6131. https://doi.org/10.1364/BOE.9.006116.
(32) Ji, M.; Orringer, D. A.; Freudiger, C. W.; Ramkissoon, S.; Liu, X.; Lau, D.; Golby, A. J.; Norton, I.; Hayashi, M.; Agar, N. Y. R.; Young, G. S.; Spino, C.; Santagata, S.; Camelo-Piragua, S.; Ligon, K. L.; Sagher, O.; Xie, X. S. Rapid, Label-Free Detection of Brain Tumors with Stimulated Raman Scattering Microscopy. *Science Translational Medicine* **2013**, *5* (201), 201ra119-201ra119. https://doi.org/10.1126/scitranslmed.3005954.
(33) Medrek, C.; Pontén, F.; Jirström, K.; Leandersson, K. The Presence of Tumor Associated Macrophages in Tumor Stroma as a Prognostic Marker for Breast Cancer Patients. *BMC Cancer* **2012**, *12*, 306. https://doi.org/10.1186/1471-2407-12-306.
(34) Aras, S.; Zaidi, M. R. TAMeless Traitors: Macrophages in Cancer Progression and Metastasis. *Br. J. Cancer* **2017**, *117* (11), 1583–1591. https://doi.org/10.1038/bjc.2017.356.
(35) Salvi, M.; Molinari, F. Multi-Tissue and Multi-Scale Approach for Nuclei Segmentation in H&E Stained Images. *BioMedical Engineering OnLine* **2018**, *17* (1), 89. https://doi.org/10.1186/s12938-018-0518-0.
(36) Caicedo, J. C.; Roth, J.; Goodman, A.; Becker, T.; Karhohs, K. W.; Broisin, M.; Molnar, C.; McQuin, C.; Singh, S.; Theis, F. J.; Carpenter, A. E. Evaluation of Deep Learning Strategies for Nucleus Segmentation in Fluorescence Images. *Cytometry Part A* **2019**, *95* (9), 952–965. https://doi.org/10.1002/cyto.a.23863.
(37) Ji, M.; Lewis, S.; Camelo-Piragua, S.; Ramkissoon, S. H.; Snuderl, M.; Venneti, S.; Fisher-Hubbard, A.; Garrard, M.; Fu, D.; Wang, A. C.; Heth, J. A.; Maher, C. O.; Sanai, N.; Johnson, T. D.; Freudiger, C. W.; Sagher, O.; Xie, X. S.; Orringer, D. A. Detection of Human Brain Tumor Infiltration with Quantitative Stimulated Raman Scattering Microscopy. *Science Translational Medicine* **2015**, *7* (309), 309ra163-309ra163. https://doi.org/10.1126/scitranslmed.aab0195.

Chapter 6. IN VIVO SIMULTANEOUS NONLINEAR ABSORPTION RAMAN AND FLUORESCENCE (SNARF) IMAGING OF MOUSE BRAIN CORTICAL STRUCTURES

6.1 INTRODUCTION

Two-photon excited fluorescence (2PEF) has revolutionized neurophotonics through the development of a palette of targeted dyes and transgenic models. Using highly specific stains, current methods allow researchers to investigate a wide array of cells and structures including, but not limited to, neurons[1,2], astrocytes[3,4], pericytes[5], endothelial cells[6], and vasculature[7,8]. Compared to single photon fluorescence, or linear fluorescence, 2PEF makes use of longer, less scattering wavelengths which enables deep penetration into tissues. As with all multiphoton microscopy (MPM) techniques, intrinsic optical sectioning affords 2PEF high spatial and axial resolution. All combined, 2PEF provides researchers with a powerful and straightforward platform that has been invaluable in elucidating cellular mechanisms[9–11], cortical circuitry[12], and numerous pathologies in the brain[13]. However, 2PEF emission spectra are typically broad and featureless which limits the number of separable fluorescent contrasts. Label-free MPM techniques offer an attractive route to increase the number of achievable contrasts in a single-shot experiment. Specifically, stimulated Raman scattering (SRS) microscopy and transient absorption microscopy (TAM) are two label-free MPM techniques that could provide more holistic characterization of cortical structures in the brain.

As a multiphoton analog to spontaneous Raman scattering, SRS provides quantitative differentiation between chemical species based on characteristic vibrational signatures. In SRS

microscopy, the energy difference between two lasers is used to coherently excite a vibrational transition of interest. Recently, we demonstrated optimization of SRS microscopy for achieving label-free pathology of mouse and human brain tissues *ex vivo* with strong agreement to traditional pathological preparation and staining.[14,15] Recently, Ji et al demonstrated *in vivo* pathological differentiation between tumor and nonneoplastic tissue in a xenografted mouse model. However, due to poor penetration depth, SRS microscopy was limited to ~100 μm imaging depth.[16] To address this issue, our group and others have worked to increase penetration depth via pulse optimization[14], tissue clearing[17,18], and deep learning[19,20], among others.

Currently, the leading method of visualizing vasculature in the brain relies on intravenous injection of a dye conjugated with a high molecular weight molecule, such as dextran. While this method has enabled unparalleled imaging depth in the brain, it requires repeated injections for longitudinal studies and offers no potential for quantification of the blood compartment (i.e., hematocrit, oxygen saturation, etc.). TAM offers a direct and label-free measurement of hemoglobin and hemodynamics.[21–26] TAM encompasses numerous photophysical processes that constitute the transient lifetime of a molecule. Importantly, differences in transient lifetime can be used to distinguish and quantify species of hemoglobin, such as oxyhemoglobin, deoxyhemoglobin, and glycated hemoglobin. With careful selection of excitation wavelengths, hemoglobin transient lifetime can extend up to a couple picoseconds due to a strong contribution of excited state absorption (ESA). As such, TAM has found tremendous utility *in vitro* and *in vivo*. However, the application of TAM for quantitative *in vivo* brain imaging has remained elusive.

We believe that coupling together MPM techniques will allow for more holistic optical characterization of cortical structures in vivo. In this study, we construct a multimodal microscope capable of simultaneously conducting 2PEF, SRS, and TAM measurements of the same optical

volume in a live mouse brain. With this system, we compare the cortical structure differences observed between three groups of mice: young (P30-P50), middle-aged (P200-P250), and old (P630-P635). Notably, we demonstrate label-free in vivo quantification of axon myelination and deformities with age, visualization of vasculature and cell density, and cell density and identification up to 200 µm into the cortex. We perform fluorescence labelling of astrocytes and pericytes via topical application of sulforhodamine 101 and Neurotrace, respectively, to distinguish cell nuclei visualized with SRS and classify cellular subtypes.

6.2 METHODS

6.2.1 *Multiphoton Imaging System*

The multiphoton system used for imaging, shown in Figure 6.1A, was adapted from the system described in Section 2.2.1. The laser system starts with a broadband femtosecond dual beam laser (Spectra-Physics, Insight DS+) outputting two beams with an 80 MHz (f_0) repetition rate. The two outputs are: a fixed beam at 1040 nm, used as the pump, and a tunable beam ranging from 680 to 1300 nm, used as the probe. The pump beam (fixed at 1040 nm) was amplitude modulated at 20 MHz ($f_0/4$) by an electro-optical modulator (EOM1, θ_1) and a polarizing beam splitter (PBS). The amplitude modulated pulse train was followed by another polarization modulation at 20 MHz with a second EOM (EOM2, θ_2). The second EOM is operated 90 degrees phase shifted from the first EOM (i.e., $\theta_2 - \theta_1 = 90°$), resulting in two orthogonal phase pulse trains (s and p polarization). The resulting pulse trains are illustrated in Figures 2.1A and 2.1B. From here, the beam was passed through a 20 mm of birefringent quartz crystal (BRC) (Union Optic, BIF-Quartz). Next, the beam was sent through a half waveplate (HWP) and PBS to combine both beams into a single polarization.

The precise pulse durations of the pump pulses were controlled using a grating-based pulse compressor (GC).[21] The tunable probe beam (800 nm) was sent through 24 cm of highly dispersive glass rod (HZF52A) and a delay arm (DL) to temporally overlap with the orthogonal phase pump beams before all beams were spatially overlapped using a dichroic mirror (DCM) and directed through a scanning microscope and 40X objective (N40XLWD-NIR). Fluorescence signal was collected using a DCM and photomultiplier tube (PMT). SRS signal was collected in epi-mode using a PBS and photodiode (PD). The two signals were detected by a dual-phase lock-in amplifier (Zurich Instrument) with orthogonal outputs after filtering out the two pump beams using a short pass filter (SPF). Two images were acquired simultaneously at a frame rate of 1 frame/sec for an image size of 512×512 pixels.

6.2.2 *In Vivo Mouse Brain Imaging*

All experimental animal procedures were approved by the Institute of Animal Care and Use Committee (IACUC) of the University of Washington (protocol # 4395-01). Cranial window surgery was performed on female C57Bl6 mice ranging from P37 to P632 purchased from Jackson Laboratory. Briefly, mice were anesthetized using 4% isoflurane (1 L/min O_2) and a ~3 mm craniotomy was performed using a high-speed surgical hand drill. Next, fluorescent dyes – Neurotrace 500/525 and sulforhodamine 101 (SR101) – were topically applied to the exposed brain and a 5 mm coverslip was placed over the craniotomy. Neurotrace 500/525 and SR101 were applied for 5 and 10 min, respectively, as described previously.[28,5] Before sealing the window with dental cement (Parkell), the window was filled with modified artificial cerebrospinal fluid to mitigate tissue movement during imaging.[29]

6.3 RESULTS

SRS microscopy has been widely used to image lipids and proteins in a variety of systems ranging from cells to tissue. Spectral contrast between these species is achieved by probing two transitions, 2850 cm^{-1} (lipids) and 2930 cm^{-1} (lipids and proteins), in the CH stretching region. Figures 6.1C and 6.1D provide representative images (~140×140 μm) from a P246 mouse collected 20 μm below the pial surface at these two transitions that demonstrate clear structural differences between the two species. Notably, Figure 6.1C shows the absence of lipid-poor cell nuclei and the presence of thin lipid-rich myelin sheath. SRS has been used previously to visualize and quantify myelination in the sciatic nerve of rodents with ALS based on the high concentration of lipids.[30]

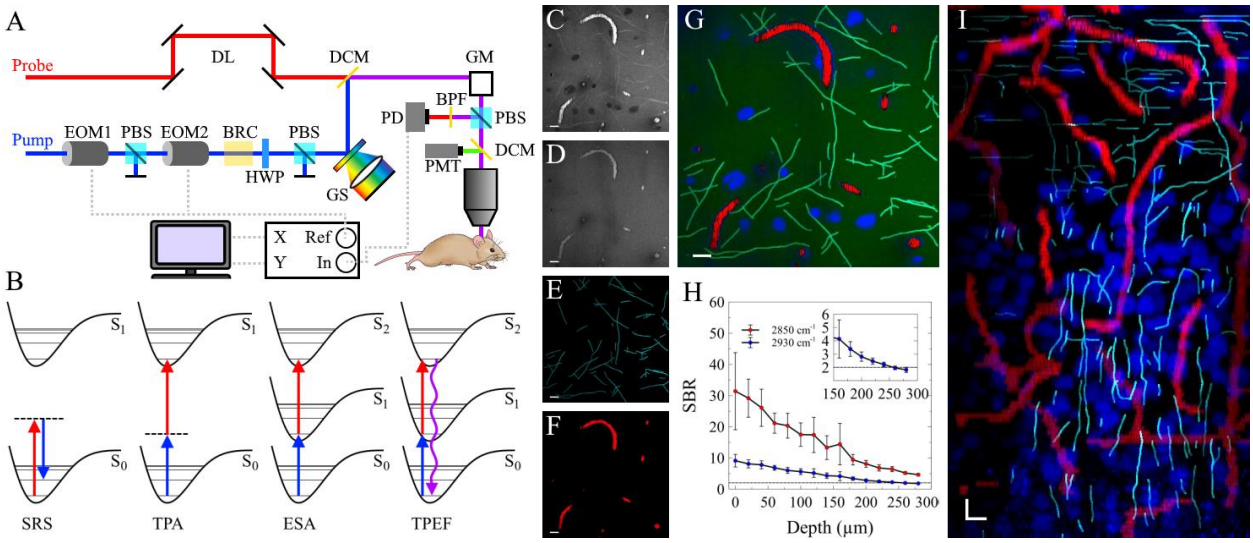

Figure 6.1. Construction of a multimodal multiphoton microscope. A) Experimental set up. DL: delay line, DCM: dichroic mirror, GM: galvanomirrors, EOM: electro-optic modulator, PBS: polarizing beam splitter, BRC: birefringent crystal, HWP: half-wave plate, GS: grating-based pulse stretcher, PD: photodiode, PMT: photomultiplier tube. B) Energy level diagrams of the multiphoton techniques employed. C) and D) SRS imaging at 2850 cm^{-1} and 2930 cm^{-1}, respectively. E) Extracted myelin signal. F) Extracted blood vessels. G) Composite image of lipids (green), proteins (blue), myelin (cyan), and blood vessels (red) after signal extraction and spectral unmixing. H) Signal-to-background ratio (SBR) of each wavenumber as a function of depth. I) Simulated B-slice. Scale bars: 10 μm.

To quantify myelination in our measurements, we employed a simple tracing program to allow us to separate and measure myelin segments directly.[31] Figure 6.1E shows the resulting image of traced myelin segments. In addition to SRS, the images provided in Figures 6.1C and 6.1D capture TAM signals as well. These signals can be separated based on three characteristics: signal intensity, wavenumber independence, and morphology. TAM signals are typically stronger than SRS signal due to the strong absorption of near-IR wavelengths by hemoglobin. Additionally, in contrast to SRS, TAM signals are relatively independent of targeted wavenumber. Thus, TAM signals have similar intensities in both Figures 6.1C and 6.1D. Lastly, tissue structure is static throughout imaging whereas blood vessels can be identified due to flowing blood cells. These differences allow us to separate blood vessels in Figure 6.1F. Lastly, we perform denoising of Figure 6.1C and 6.1D using a previously described technique[19,20] followed by spectral unmixing to regain a pure protein image.[14] All combined in Figure 6.1G, these label-free contrasts provide an instantaneous snapshot of three cortical structures: cell density, myelination, and vasculature.

Cortical structures are highly dependent on location and depth. As such, the utility of any microscopy technique is related to its imaging depth. While Figures 6.1C-6.1G demonstrate the high-quality imaging capabilities of SRS microscopy and TAM at superficial depths, in vivo SRS microscopy studies have reported limited imaging depths of ~100 μm in highly scattering tissues.[16] Given the powerful capabilities of SRS microscopy, significant effort has been put forth to improve imaging depths. Recently, we characterized signal-to-background ratios (SBR) for SRS microscopy, demonstrated a deep learning algorithm to increase SBR, and reported an improved imaging depth of 210 μm in ex vivo mouse brain tissue.[20] In this study, we provide the first quantification of SBR, as previously defined, for in vivo SRS microscopy at 2850 cm^{-1} and 2930 cm^{-1} shown in Figure 6.1H. Setting an SBR requirement of >2, we observed imaging depths of

>300 µm and ~250 µm for 2850 cm^{-1} and 2930 cm^{-1}, respectively. With a depth limit of 250 µm, we provide an XZ max intensity projection in Figure 6.1I after separating both myelin signal and hemoglobin TAM signal. From Figure 2G, the transition from layer 1 to layers 2/3 can be clearly observed by the increase in cell nuclei density. Additionally, the transition from predominantly horizontal axons near the pial surface to vertical axons deeper into the cortical tissue.

To further investigate myelination and myelin structure, we performed 3D imaging of three groups of mice: young (P37, P38, P48), middle-aged (P202, P209, P244, P246), and old (P630, P631, P631). Figure 6.2A provides the 3D rendering of myelin structure from a P246 mouse. The model illustrates the ascension and arborization of axons from deeper layers of the cortex into the surface layers. This structure is further demonstrated in the maximum intensity projections shown in Figure 6.2B. The cortical surface is rich in myelin with a web-like structure of overlapping and intersecting axons. Deeper into the cortex, the axons turn to penetrate deeper resulting in predominantly cross-sectional views of myelin sheaths. As previously described with other microscopy techniques, myelination is closely related to animal age.[32–37] Figures 6.2C-6.2E provide a representative comparison in myelin density of the first 20 µm of cortex between young (P38), middle-aged (P246), and old (P631) mice. We quantified the average myelin length over the top 60 µm of cortex between the three groups and provide the resulting plot in Figure 6.2F. In agreement with previous reports, we observe a significant increase in myelination between the age groups.

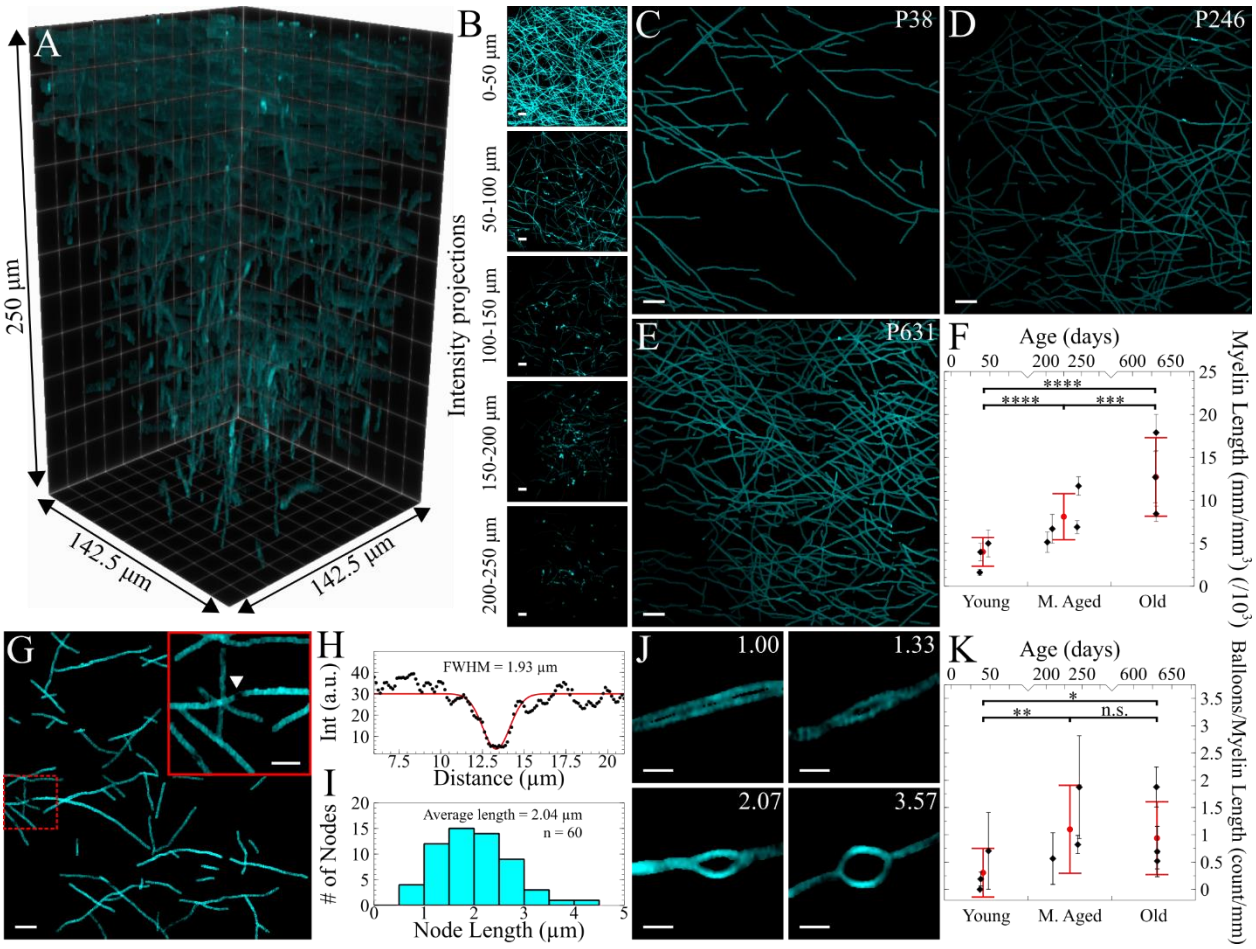

Figure 6.2. Label-free *in vivo* imaging of myelin with SRS microscopy. A) 3D rendering of myelin. B) Intensity projections of the 3D volume shown in A) projected every 50 µm. C-E) Intensity projection of the top 20 µm of myelination of a P38, P246, and P631 mouse. F) Quantitative comparison of myelination between different aged mice. G) Suspected Node of Ranvier. H) Line profile and fitting across suspected Node of Ranvier shown in G). I) Average length of suspected Node of Ranvier. J) Quantification of myelin ballooning from not ballooning (1.00) to severe ballooning (3.57). K) Number of balloons observed per length of myelin as a function of age. Scale bars: 10 µm, J) and inset G) scale bar: 2 µm.

In addition to quantifying myelin length, we observed two distinct myelin structure: nodes of Ranvier and myelin ballooning. Figure 6.2G provides a representative image of a suspected node of Ranvier. The inset image provides an enlarged image and arrowhead indicating the suspected node. In Figure 6.2H, we fit the intensity profile of the myelin segment to determine a

full width, half maximum of 1.93 μm. We repeated this procedure for 60 suspected nodes across several fields of view of a P246 mouse to produce the histogram shown in Figure 6.2I with an average node length of 2.04 ± 0.76 μm. This is longer than the true length of ~1 μm, suggesting that our measurements are including paranodal length as well. Figure 6.2J illustrates the observed myelin ballooning structures from a P246 mouse. We identify myelin balloons by the width ratio of the ballooned segment and the nonballooned segment as >1.3. The ratio is reported with each area shown in Figure 6.2J. The most severe ballooning increased the myelin segment over 3.5 times in width. Some reports have suggested that myelin ballooning is related to normal aging. To determine the effects of aging on balloon density, we compared the ratio of balloons to myelin length between age groups and provide the results in Figure 6.2K. We found a significant increase in balloon density between the young mouse group and the two older groups, but no significant difference between middle aged mice and old mice.

Next, we present label-free *in vivo* imaging of microvasculature. Typical *in vivo* brain vasculature 2PEF imaging requires an exogenous agent to stain the blood compartment. In contrast, we directly image red blood cells via the strong intrinsic absorption of hemoglobin. Figure 6.3A provides a 3D rendering of the label-free TAM imaging of a ~140×140×250 μm volume of mouse brain microvasculature. Figure 6.3B provides the intensity projection of the volume shown in Figure 6.3A. Recently, the phenomenon of stalled vessels and their impact on cerebral blood flow was reported in WT and Alzheimer's model mice.[13] Here, the vessels shown in white represented stalled vessels. We identify stalled vessels by imaging the same tissue volume 15 minutes apart, see Figure 6.3C and 6.3D. The green arrows in Figures 6.3C and 6.3D indicate the vessels that were only transiently stalled between the two timepoints (i.e., stalled in only one of the time points). The purple arrow indicates a vessel stalled at both time points. To further

investigate this phenomenon, we compared the prevalence of stalled vessels between age groups. Figure 6.3E provides the percentage of stalled vessel volume to total vessel volume as a function of age. Interestingly, we found no statistical difference between the prevalence of stalled vessels with age. Previously, it was reported that stalled vessels were narrower in width than flowing vessels. We measured the width of 68 stalled vessel segments and 464 flowing vessel segments to

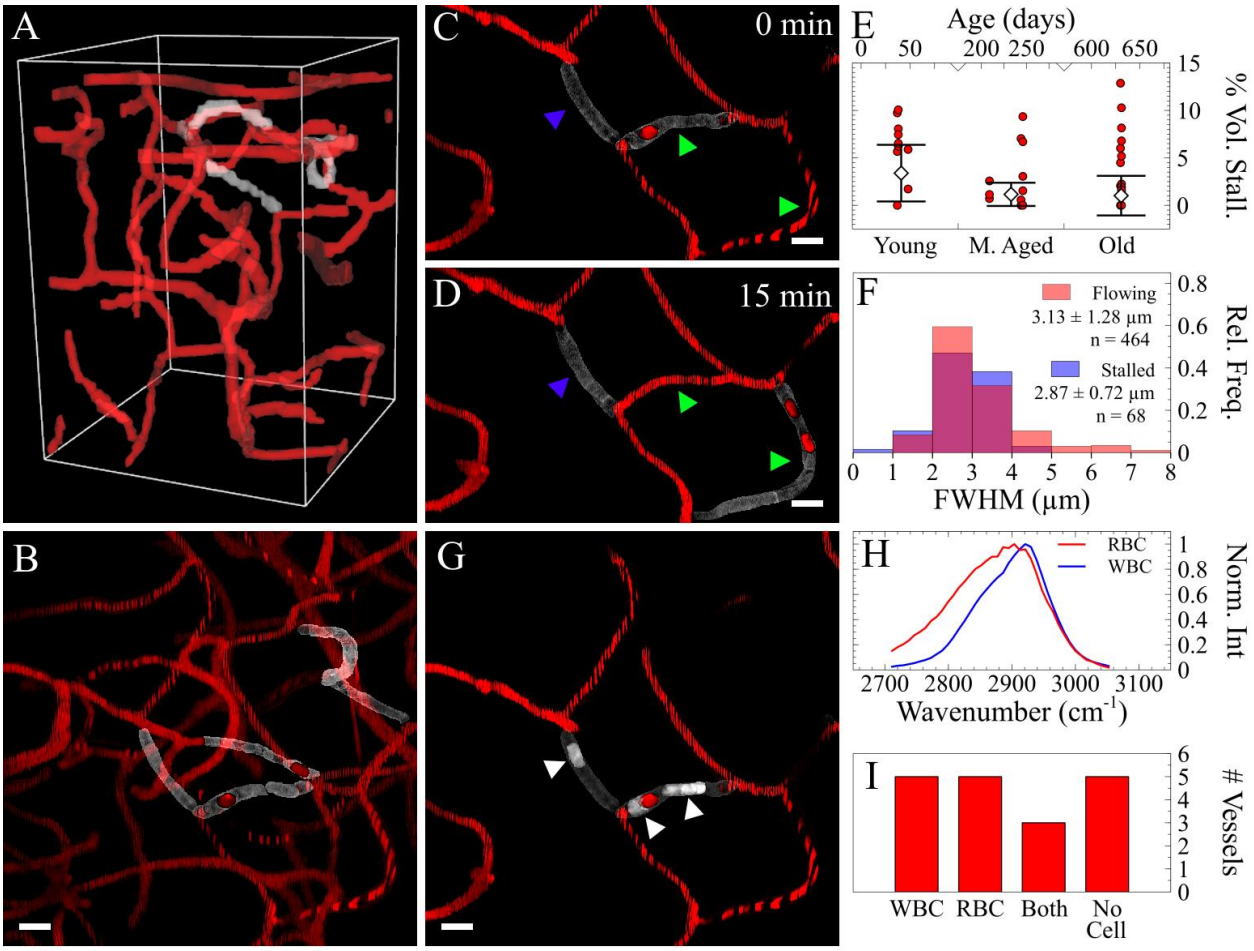

Figure 6.3. Label-free *in vivo* imaging of mouse brain vasculature with TAM. A) 3D rendering of mouse brain vasculature. B) Intensity projection of flowing and stalled vessels from A). C and D) Repeated imaging of vasculature to identify stalled vessels. E) Comparison of stalled vessel volume to total vessel volume between age groups. F) Average vessel width between flowing and stalled vessels. G) SRS imaging of WBCs stalled within vasculature, indicated by white arrowheads. H) Spectral differences between RBCs and WBCs. I) Frequency of WBC, RBC, both, or no cell observed in vessels stalled for 15 min. Scale bars: 10 µm.

find that only a slight difference in vessel width (stalled vessel width = 2.87 ± 0.87 μm; flowing vessel width = 3.13 ± 1.28 μm). Figure 6.3F provides the relative frequency histograms of vessel width for stalled and flowing vessels.

Additionally, SRS provides label-free imaging of white blood cells, shown in Figure 6.3G. The WBC nuclei, indicated by the white arrows in Figure 6.3G, can be separated from RBCs based on intrinsic spectral differences, as shown in Figure 6.3H. Next, we investigated the contents of the stalled vessels and found four categories: stalled with 1) WBC(s), 2) RBC(s), 3) both WBC(s) and RBC(s), or 4) no cells. Figure 6.3I provides the frequency of each category over the 18 vessels identified. Importantly, only vessels that were fully contained within the imaging volume were considered.

Finally, we demonstrate the visualization of cell density in the cortex with SRS microscopy. Figure 6.4A provides a 3D rendering of a ~140×140×250 μm volume of mouse brain vasculature with TAM and protein-rich cell nuclei with SRS microscopy. The mouse cortex has six layers that each contain unique and distinct cellular subtypes that enable dynamic brain activity.[38] The outermost layer, layer 1 (L1), contains the lowest cellular density of the cortical layers, constituted mostly of non-neuronal cells, such as astrocytes. Depending on precise cortical region, the thickness of L1 ranges from about 100 μm to 130 μm. The transition from L1 to layer 2 (L2) is marked by a sharp increase in cells, primarily neurons, at the border between the two layers. To demonstrate the label-free capability of SNARF imaging for visualizing cellular density and tissue structure *in vivo*, we provide 2D projections of three depths of cortical tissue: 40-50 μm, 90-100 μm, and 140-150 μm in Figures 6.4B-6.4D. Here, we observe a clear increase in cellular density as a function of depth. Beyond visualization, we quantified the cellular density of a P246 mouse as a function of depth. Near 110 μm, the number of cells doubles indicating the transition

from L1 to L2. This trend was observed in all mice in this study (n = 10) and the transition varied by less than 20 µm. Next, we wanted to determine if SRS could identify cellular subtypes based on morphology and intensity. To do so, we stained the astrocytes in the upper cortex using sulforhodamine 101 (SR101) allowing us to distinguish between the nuclei that belong to astrocytes or non-astrocytes. We observed significant differences ($p<0.0001$) in both sphericity and protein/lipid ratio between astrocyte nuclei and non-astrocyte nuclei indicating that SRS is

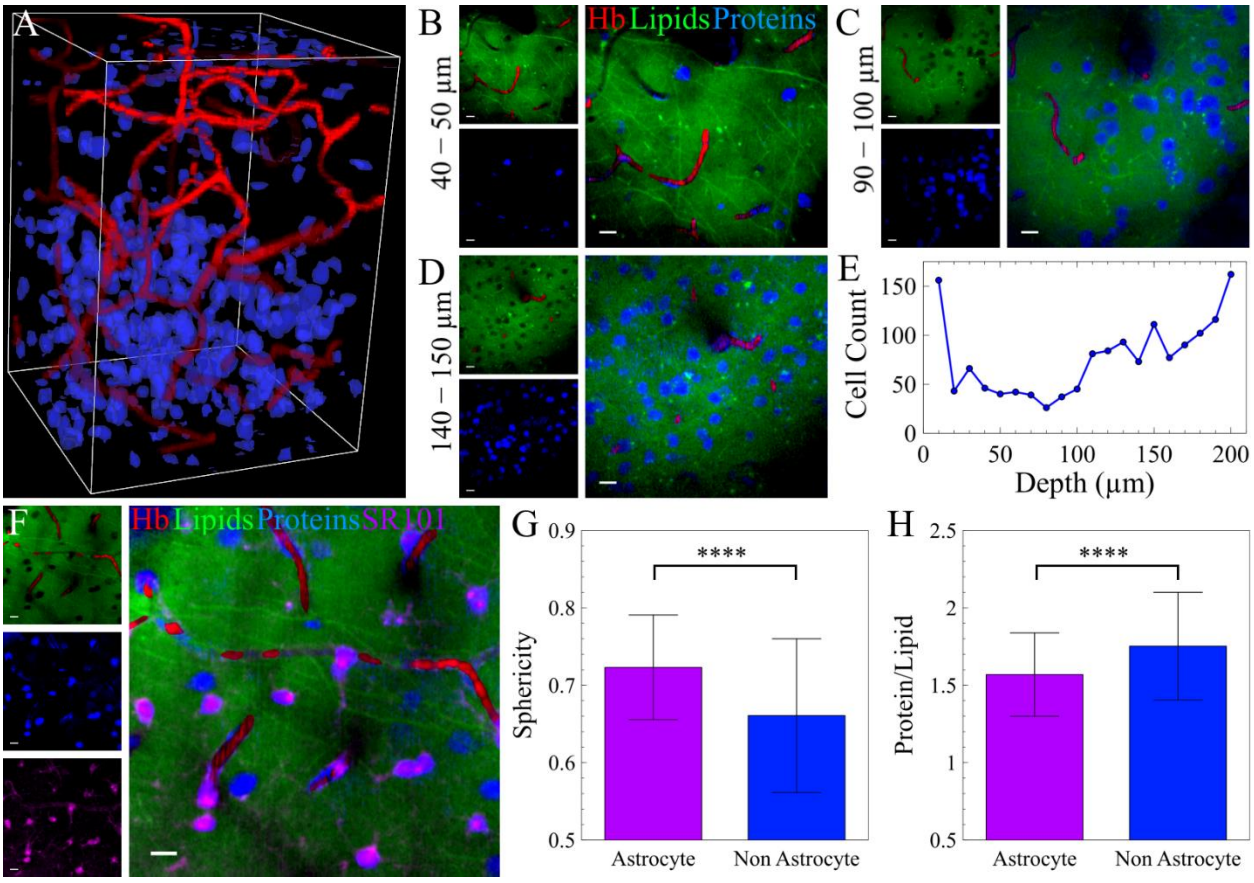

Figure 6.4. Imaging cellular density and morphology in upper cortex *in vivo*. A) 3D rendering of mouse brain vasculature (red) and cell nuclei (blue). B-D) Depth projections of 40-50 µm, 90-100 µm, 140-150 µm. E) Cell count as a function of depth. Cells were summed over 10 µm. F) Correlating cell nuclei with SR101-stained cells. G) Sphericity of astrocyte nuclei (n = 266) and non-astrocyte nuclei (n = 924). H) Ratio of proteins to lipids of astrocyte nuclei (n = 266) and non-astrocyte nuclei (n = 924). Scale bars: 10 µm. ****: $p<0.0001$.

capable of distinguishing between the two populations based on intrinsic nuclear differences. However, the two populations of nuclei still contain substantial overlap in sphericity and protein/lipid ratio. This is likely to confound the identification of cell type based on these metrics alone. Importantly, the large standard deviation of the non-astrocyte population is observed due to the heterogeneity in sphericity and intensity ratio that exists amongst the various non-astrocyte cell types within the upper cortical layers. To improve identification and separate between the non-astrocyte cell types, we will consider the proximity of the cell to neighboring vasculature. We believe that this will allow us a label-free method of distinguishing between cell types and thus, differences in morphology.

6.4 Discussion and Conclusion

Fluorescent labels and transgenic models have facilitated invaluable contributions to neurophotonics. The ubiquity of 2PEF in neurophotonics is largely due to its low technical barrier and straightforward data analysis. These factors have enabled a broader scope of researchers to employ 2PEF. Thus, while recent advancements have enabled multiplexing of several fluorescent contrasts simultaneously[39], these techniques are technically challenging and restrictive in the selection of excitable dyes. We demonstrate label-free methods to visualize myelination, hemodynamics, and cell identification based on well-established complimentary multiphoton techniques, SRS microscopy and TAM. We believe that these techniques offer an alleviation on the technical burden of achieving multiple contrasts in a single-shot experiment.

With SRS microscopy, we present holistic *in vivo* imaging of the spatial distributions of lipids (2850 cm^{-1}) and proteins (2930 cm^{-1}) in the upper cortical layers of mouse brain. Based on the intrinsic lipid density of myelin, we quantified myelination between three age groups of mice: young (P38-P48), middle aged (P202-P246), and old (P630-P632). With our method, we report an

increase in myelination with age. These results agree well with the trend observed using spectral confocal reflectance (SCoRe) microscopy.[40,41] Additionally, we report observation of myelin balloons, a myelin formation previously characterized in monkeys by electron microscopy.[42,43] Our demonstration represents the first observation of such features in a live mouse brain.

With TAM, we present *in vivo* imaging of hemoglobin and vasculature in the brain. Previously, longitudinal studies into the development and restructuring of mouse brain vasculature required repeated injections of fluorescent dyes to visualization. TAM provides a label-free method of achieving similar contrast. Additionally, by coupling SRS microscopy with TAM, the cellular contents of both stalled and flowing vessels can be readily observed.

Importantly, SRS microscopy and TAM can be applied to any mouse, alleviating the financial burden of purchasing and maintaining a transgenic mouse colony. And in the case of topical dye application to an exposed cortex, a sealed cranial window does not allow for additional dye application. Moreover, label-free methods benefit from being less invasive than dye application. For instance, it has been reported that overexposure of the cortex to SR101 can induce seizure-like activity in mice.[28] In the case of stalled vessel flow, Cruz Hernandez et al reported that application of the fluorescently labeled antibody used to stain the WBC within the stalled vessel lead to the clearing of stalled vessels 10 min after application.[13] Both of these reports solidify the need for less invasive, label-free imaging methods to better preserve the animal's physiology.

6.5 Future Directions

We are currently working on a protocol to identify cell types in the top layers the mouse brain cortex. We achieve this by classifying SRS images of cell nuclei as either an astrocyte or pericyte as stained by SR101 and Neurotrace, respectively. Figure 6.4 provides our current results with cell identification.

6.6 REFERENCES

(1) Stosiek, C.; Garaschuk, O.; Holthoff, K.; Konnerth, A. In Vivo Two-Photon Calcium Imaging of Neuronal Networks. *PNAS* **2003**, *100* (12), 7319–7324. https://doi.org/10.1073/pnas.1232232100.
(2) Dana, H.; Sun, Y.; Mohar, B.; Hulse, B. K.; Kerlin, A. M.; Hasseman, J. P.; Tsegaye, G.; Tsang, A.; Wong, A.; Patel, R.; Macklin, J. J.; Chen, Y.; Konnerth, A.; Jayaraman, V.; Looger, L. L.; Schreiter, E. R.; Svoboda, K.; Kim, D. S. High-Performance Calcium Sensors for Imaging Activity in Neuronal Populations and Microcompartments. *Nature Methods* **2019**, *16* (7), 649–657. https://doi.org/10.1038/s41592-019-0435-6.
(3) Nimmerjahn, A.; Helmchen, F. In Vivo Labeling of Cortical Astrocytes with Sulforhodamine 101 (SR101). *Cold Spring Harb Protoc* **2012**, *2012* (3), pdb.prot068155. https://doi.org/10.1101/pdb.prot068155.
(4) Appaix, F.; Girod, S.; Boisseau, S.; Römer, J.; Vial, J.-C.; Albrieux, M.; Maurin, M.; Depaulis, A.; Guillemain, I.; Sanden, B. van der. Specific In Vivo Staining of Astrocytes in the Whole Brain after Intravenous Injection of Sulforhodamine Dyes. *PLOS ONE* **2012**, *7* (4), e35169. https://doi.org/10.1371/journal.pone.0035169.
(5) Damisah, E. C.; Hill, R. A.; Tong, L.; Murray, K. N.; Grutzendler, J. A FluoroNissl Dye Identifies Pericytes as Distinct Vascular Mural Cells during in Vivo Brain Imaging. *Nat Neurosci* **2017**, *20* (7), 1023–1032. https://doi.org/10.1038/nn.4564.
(6) Hartmann, D. A.; Underly, R. G.; Watson, A. N.; Shih, A. Y. A Murine Toolbox for Imaging the Neurovascular Unit. *Microcirculation* **2015**, *22* (3), 168–182. https://doi.org/10.1111/micc.12176.
(7) Blinder, P.; Tsai, P. S.; Kaufhold, J. P.; Knutsen, P. M.; Suhl, H.; Kleinfeld, D. The Cortical Angiome: An Interconnected Vascular Network with Noncolumnar Patterns of Blood Flow. *Nat. Neurosci.* **2013**, *16* (7), 889–897. https://doi.org/10.1038/nn.3426.
(8) Perillo, E. P.; Jarrett, J. W.; Liu, Y.-L.; Hassan, A.; Fernée, D. C.; Goldak, J. R.; Bonteanu, A.; Spence, D. J.; Yeh, H.-C.; Dunn, A. K. Two-Color Multiphoton *in Vivo* Imaging with a Femtosecond Diamond Raman Laser. *Light: Science & Applications* **2017**, *6* (11), e17095. https://doi.org/10.1038/lsa.2017.95.
(9) Nitsch, R.; Pohl, E. E.; Smorodchenko, A.; Infante-Duarte, C.; Aktas, O.; Zipp, F. Direct Impact of T Cells on Neurons Revealed by Two-Photon Microscopy in Living Brain Tissue. *J. Neurosci.* **2004**, *24* (10), 2458–2464. https://doi.org/10.1523/JNEUROSCI.4703-03.2004.
(10) Shih, A. Y.; Driscoll, J. D.; Drew, P. J.; Nishimura, N.; Schaffer, C. B.; Kleinfeld, D. Two-Photon Microscopy as a Tool to Study Blood Flow and Neurovascular Coupling in the Rodent Brain. *J. Cereb. Blood Flow Metab.* **2012**, *32* (7), 1277–1309. https://doi.org/10.1038/jcbfm.2011.196.
(11) Tran, C. H. T.; Gordon, G. R. Acute Two-Photon Imaging of the Neurovascular Unit in the Cortex of Active Mice. *Front Cell Neurosci* **2015**, *9*. https://doi.org/10.3389/fncel.2015.00011.
(12) Yang, W.; Carrillo-Reid, L.; Bando, Y.; Peterka, D. S.; Yuste, R. Simultaneous Two-Photon Imaging and Two-Photon Optogenetics of Cortical Circuits in Three Dimensions. *eLife* **2018**, *7*, e32671. https://doi.org/10.7554/eLife.32671.
(13) Cruz Hernández, J. C.; Bracko, O.; Kersbergen, C. J.; Muse, V.; Haft-Javaherian, M.; Berg, M.; Park, L.; Vinarcsik, L. K.; Ivasyk, I.; Rivera, D. A.; Kang, Y.; Cortes-Canteli, M.;

Peyrounette, M.; Doyeux, V.; Smith, A.; Zhou, J.; Otte, G.; Beverly, J. D.; Davenport, E.; Davit, Y.; Lin, C. P.; Strickland, S.; Iadecola, C.; Lorthois, S.; Nishimura, N.; Schaffer, C. B. Neutrophil Adhesion in Brain Capillaries Reduces Cortical Blood Flow and Impairs Memory Function in Alzheimer's Disease Mouse Models. *Nature Neuroscience* **2019**, *22* (3), 413–420. https://doi.org/10.1038/s41593-018-0329-4.
(14) Francis, A.; Berry, K.; Chen, Y.; Figueroa, B.; Fu, D. Label-Free Pathology by Spectrally Sliced Femtosecond Stimulated Raman Scattering (SRS) Microscopy. *PLOS ONE* **2017**, *12* (5), e0178750. https://doi.org/10.1371/journal.pone.0178750.
(15) Shin, K. S.; Francis, A. T.; Hill, A. H.; Laohajaratsang, M.; Cimino, P. J.; Latimer, C. S.; Gonzalez-Cuyar, L. F.; Sekhar, L. N.; Juric-Sekhar, G.; Fu, D. Intraoperative Assessment of Skull Base Tumors Using Stimulated Raman Scattering Microscopy. *Sci Rep* **2019**, *9* (1), 20392. https://doi.org/10.1038/s41598-019-56932-8.
(16) Ji, M.; Orringer, D. A.; Freudiger, C. W.; Ramkissoon, S.; Liu, X.; Lau, D.; Golby, A. J.; Norton, I.; Hayashi, M.; Agar, N. Y. R.; Young, G. S.; Spino, C.; Santagata, S.; Camelo-Piragua, S.; Ligon, K. L.; Sagher, O.; Xie, X. S. Rapid, Label-Free Detection of Brain Tumors with Stimulated Raman Scattering Microscopy. *Science Translational Medicine* **2013**, *5* (201), 201ra119-201ra119. https://doi.org/10.1126/scitranslmed.3005954.
(17) Wei, M.; Shi, L.; Shen, Y.; Zhao, Z.; Guzman, A.; Kaufman, L. J.; Wei, L.; Min, W. Volumetric Chemical Imaging by Clearing-Enhanced Stimulated Raman Scattering Microscopy. *PNAS* **2019**, *116* (14), 6608–6617. https://doi.org/10.1073/pnas.1813044116.
(18) Chen, Y.; Liu, S.; Liu, H.; Tong, S.; Tang, H.; Zhang, C.; Yan, S.; Li, H.; Yang, G.; Zhu, D.; Wang, K.; Wang, P. Coherent Raman Scattering Unravelling Mechanisms Underlying Skull Optical Clearing for Through-Skull Brain Imaging. *Anal. Chem.* **2019**, *91* (15), 9371–9375. https://doi.org/10.1021/acs.analchem.9b02624.
(19) Manifold, B.; Thomas, E.; Francis, A. T.; Hill, A. H.; Fu, D. Denoising of Stimulated Raman Scattering Microscopy Images via Deep Learning. *Biomed. Opt. Express, BOE* **2019**, *10* (8), 3860–3874. https://doi.org/10.1364/BOE.10.003860.
(20) Hill, A. H.; Hill, A. H.; Manifold, B.; Manifold, B.; Fu, D. Tissue Imaging Depth Limit of Stimulated Raman Scattering Microscopy. *Biomed. Opt. Express, BOE* **2020**, *11* (2), 762–774. https://doi.org/10.1364/BOE.382396.
(21) Fu, D.; Ye, T.; Matthews, T. E.; Chen, B. J.; Yurtserver, G.; Warren, W. S. High-Resolution *in Vivo* Imaging of Blood Vessels without Labeling. *Opt. Lett., OL* **2007**, *32* (18), 2641–2643. https://doi.org/10.1364/OL.32.002641.
(22) Fu, D.; Matthews, T. E.; Ye, T.; Piletic, I. R.; Warren, W. S. Label-Free in Vivo Optical Imaging of Microvasculature and Oxygenation Level. *J Biomed Opt* **2008**, *13* (4), 040503. https://doi.org/10.1117/1.2968260.
(23) Chen, T.; Huang, Y. Label-Free Transient Absorption Microscopy for Red Blood Cell Flow Velocity Measurement in Vivo. *Anal. Chem.* **2017**, *89* (19), 10120–10123. https://doi.org/10.1021/acs.analchem.7b01952.
(24) Zhang, L.; Zou, X.; Zhang, B.; Cui, L.; Zhang, J.; Mao, Y.; Chen, L.; Ji, M. Label-Free Imaging of Hemoglobin Degradation and Hemosiderin Formation in Brain Tissues with Femtosecond Pump-Probe Microscopy. *Theranostics* **2018**, *8* (15), 4129–4140. https://doi.org/10.7150/thno.26946.
(25) Dong, P.-T.; Lin, H.; Huang, K.-C.; Cheng, J.-X. Label-Free Quantitation of Glycated Hemoglobin in Single Red Blood Cells by Transient Absorption Microscopy and Phasor Analysis. *Science Advances* **2019**, *5* (5), eaav0561. https://doi.org/10.1126/sciadv.aav0561.

(26) Francis, A. T.; Berry, K.; Thomas, E. C.; Hill, A. H.; Fu, D. In Vitro Quantification of Single Red Blood Cell Oxygen Saturation by Femtosecond Transient Absorption Microscopy. *J. Phys. Chem. Lett.* **2019**, 3312–3317. https://doi.org/10.1021/acs.jpclett.9b01116.
(27) Pologruto, T. A.; Sabatini, B. L.; Svoboda, K. ScanImage: Flexible Software for Operating Laser Scanning Microscopes. *Biomed Eng Online* **2003**, *2*, 13. https://doi.org/10.1186/1475-925X-2-13.
(28) Rasmussen, R.; Nedergaard, M.; Petersen, N. C. Sulforhodamine 101, a Widely Used Astrocyte Marker, Can Induce Cortical Seizure-like Activity at Concentrations Commonly Used. *Scientific Reports* **2016**, *6* (1), 30433. https://doi.org/10.1038/srep30433.
(29) Shih, A. Y.; Driscoll, J. D.; Drew, P. J.; Nishimura, N.; Schaffer, C. B.; Kleinfeld, D. Two-Photon Microscopy as a Tool to Study Blood Flow and Neurovascular Coupling in the Rodent Brain. *J. Cereb. Blood Flow Metab.* **2012**, *32* (7), 1277–1309. https://doi.org/10.1038/jcbfm.2011.196.
(30) Tian, F.; Yang, W.; Mordes, D. A.; Wang, J.-Y.; Salameh, J. S.; Mok, J.; Chew, J.; Sharma, A.; Leno-Duran, E.; Suzuki-Uematsu, S.; Suzuki, N.; Han, S. S.; Lu, F.-K.; Ji, M.; Zhang, R.; Liu, Y.; Strominger, J.; Shneider, N. A.; Petrucelli, L.; Xie, X. S.; Eggan, K. Monitoring Peripheral Nerve Degeneration in ALS by Label-Free Stimulated Raman Scattering Imaging. *Nat Commun* **2016**, *7* (1), 13283. https://doi.org/10.1038/ncomms13283.
(31) Meijering, E.; Jacob, M.; Sarria, J.-C. F.; Steiner, P.; Hirling, H.; Unser, M. Design and Validation of a Tool for Neurite Tracing and Analysis in Fluorescence Microscopy Images. *Cytometry Part A* **2004**, *58A* (2), 167–176. https://doi.org/10.1002/cyto.a.20022.
(32) Schain, A. J.; Hill, R. A.; Grutzendler, J. Label-Free in Vivo Imaging of Myelinated Axons in Health and Disease with Spectral Confocal Reflectance Microscopy. *Nat Med* **2014**, *20* (4), 443–449. https://doi.org/10.1038/nm.3495.
(33) Hill, R. A.; Li, A. M.; Grutzendler, J. Lifelong Cortical Myelin Plasticity and Age-Related Degeneration in the Live Mammalian Brain. *Nature Neuroscience* **2018**, *21* (5), 683–695. https://doi.org/10.1038/s41593-018-0120-6.
(34) Williamson, J. M.; Lyons, D. A. Myelin Dynamics Throughout Life: An Ever-Changing Landscape? *Front. Cell. Neurosci.* **2018**, *12*. https://doi.org/10.3389/fncel.2018.00424.
(35) Gonsalvez, D. G.; Yoo, S.; Fletcher, J. L.; Wood, R. J.; Craig, G. A.; Murray, S. S.; Xiao, J. Imaging and Quantification of Myelin Integrity After Injury With Spectral Confocal Reflectance Microscopy. *Front. Mol. Neurosci.* **2019**, *12*. https://doi.org/10.3389/fnmol.2019.00275.
(36) Monsma, P. C.; Brown, A. FluoroMyelin™ Red Is a Bright, Photostable and Non-Toxic Fluorescent Stain for Live Imaging of Myelin. *J Neurosci Methods* **2012**, *209* (2), 344–350. https://doi.org/10.1016/j.jneumeth.2012.06.015.
(37) Stahon, K. E.; Bastian, C.; Griffith, S.; Kidd, G. J.; Brunet, S.; Baltan, S. Age-Related Changes in Axonal and Mitochondrial Ultrastructure and Function in White Matter. *J Neurosci* **2016**, *36* (39), 9990–10001. https://doi.org/10.1523/JNEUROSCI.1316-16.2016.
(38) Douglas, R. J.; Martin, K. A. C. Neuronal Circuits of the Neocortex. *Annual Review of Neuroscience* **2004**, *27* (1), 419–451. https://doi.org/10.1146/annurev.neuro.27.070203.144152.
(39) Rakhymzhan, A.; Leben, R.; Zimmermann, H.; Günther, R.; Mex, P.; Reismann, D.; Ulbricht, C.; Acs, A.; Brandt, A. U.; Lindquist, R. L.; Winkler, T. H.; Hauser, A. E.; Niesner, R. A. Synergistic Strategy for Multicolor Two-Photon Microscopy: Application to the Analysis of Germinal Center Reactions In Vivo. *Scientific Reports* **2017**, *7* (1), 7101. https://doi.org/10.1038/s41598-017-07165-0.

(40) Hill, R. A.; Li, A. M.; Grutzendler, J. Lifelong Cortical Myelin Plasticity and Age-Related Degeneration in the Live Mammalian Brain. *Nat Neurosci* **2018**, *21* (5), 683–695. https://doi.org/10.1038/s41593-018-0120-6.
(41) Williamson, J. M.; Lyons, D. A. Myelin Dynamics Throughout Life: An Ever-Changing Landscape? *Front. Cell. Neurosci.* **2018**, *12*. https://doi.org/10.3389/fncel.2018.00424.
(42) Sugiyama, I.; Tanaka, K.; Akita, M.; Yoshida, K.; Kawase, T.; Asou, H. Ultrastructural analysis of the paranodal junction of myelinated fibers in 31-month-old-rats. *Journal of Neuroscience Research* **2002**, *70* (3), 309–317. https://doi.org/10.1002/jnr.10386.
(43) Peters, A. The Effects of Normal Aging on Myelinated Nerve Fibers in Monkey Central Nervous System. *Front. Neuroanat.* **2009**, *3*. https://doi.org/10.3389/neuro.05.011.2009.

Chapter 7. CONCLUSIONS AND FUTURE DIRECTIONS

Analytical spectroscopy and microscopy provide invaluable insight for clinical and fundamental biomedical research. The diverse range of linear and nonlinear techniques has resulted in the development of numerous techniques for countless samples and systems. In many systems, multiple approaches and techniques compete to solve the same question. Ideally, there would be a superior technique that outperforms the others. In reality, every technique has its advantages and drawbacks that must be carefully taken into consideration. The advancements detailed in Chapters 2 and 3 demonstrate pivotal steps required to develop *in vivo* quantification of hemodynamics with TAM. The two key advantages of employing TAM are the 1) label-free quantification based on the intrinsic absorption of hemoglobin and 2) straightforward coupling with complementary nonlinear microscopy techniques (e.g., 2PEF or SRS).

In Chapter 2, water was used an internal standard for the quantification of hemoglobin. Here, the main assumption was that under normal physiological conditions, hemoglobin is predominantly in the oxygen-carrying form (~95-100%), oxyhemoglobin (HbO_2). Moving towards *in vivo* quantification, the technique would break down under hypoxic conditions wherein the blood is no longer primarily HbO_2. One potential solution to strengthen this technique is determine pump/probe excitation wavelengths in which deoxyhemoglobin (Hb) and HbO_2 have similar or the same spectra. If this cannot be achieved, another potential solution would be to collect blood oximetry from the animal and correct the calibration curve accordingly due to the known TAM spectra of Hb and HbO_2 at the employed wavelengths.

In Chapter 3, TAM was employed to quantitatively measure oxygen saturation (sO_2) *in vitro* as red blood cells (RBCs) were artificially oxygenated and deoxygenated under a controlled environment. Unfortunately attempts to extend this work towards *in vivo* TAM oximetry have

resulted in less than desirable results. There are significant differences between the *in vivo* and *ex vivo* transient lifetime of hemoglobin. Thus, an external calibration of TAM with known sO_2 solutions fails to describe *in vivo* sO_2. One factor that adds to this break down is the limited dynamic range of the calibration. Although pump/probe wavelengths of 1040 nm/700 nm provided the best excitation pair for *in vitro* TAM, the sensitivity of the technique can be improved. As shown in Chapters 2 and 3, TAM is wavelength dependent. One main constraint of the work described in Chapter 3 is the fixed pump wavelength of 1040 nm. In order to fully optimize TAM oximetry, a variable ultrafast pump source would be required. This tunability can be achieved with the use of a homebuilt optical parametric oscillator (OPO).[1] With tunable pump and probe wavelengths, a more complete characterization of wavelengths can be achieved. Another key step in translating TAM oximetry into an *in vivo* technique will be rigorous validation of the analytical capabilities. This can be achieved by comparing *in vivo* TAM oximetry from either mouse brain or ear to standard pulse oximetry. For an animal under constant vaporized anesthesia, the oxygen concentration in the carrier gas can be varied to change the system sO_2 of the animal. The *in vivo* TAM should demonstrate the same relative changes in sO_2 as the standard pulse oximetry. Towards absolute quantification, TAM oximetry can be validated in comparison to previously demonstrated 2PLM. TAM benefits from straightforward multiplexing with other multiphoton techniques as seen in Chapter 6.

In Chapters 4 and 5 improvements to stimulated Raman histology (SRH) for use in an intraoperative setting were demonstrated. Optimized excitation pulses and a novel recoloring scheme provided an 87% diagnostic accuracy of SRH compared to traditional pathological staining. The translation of SRS microscopy from laboratory to clinic is underway and pivotal steps to ensure diagnostic utility are reported frequently. Most notably, Orringer et al has already

demonstrated the diagnostic capabilities of SRH in the surgical suite.[2] On the technical side, research groups are working to simplify and miniaturize the SRS setup to remove the physical constraints of a typical SRS experiment. Fiber based laser systems offer cheaper, more compact excitation sources for multiphoton experiments. Recently, JiXin et al presented a handheld fiber-based SRS scanning device capable of achieving ~15 cm^{-1} spectral resolution[3], sufficient to perform stimulated Raman histology (SRH). On the diagnostic side, research groups have employed machine learning has to interpret SRH images and provide a diagnosis.[4,5] In a recent study performed by Zhang et al, a convolutional neural network (CNN) achieved 100% diagnostic accuracy over 33 surgical specimens.[4]

In Chapter 6, TAM, SRS, and 2PEF are combined to study mouse brain cortical structures (i.e., vasculature density, myelination, and cell populations) *in vivo*. Specifically, TAM was employed to visualize hemodynamics. While TAM has been used to study hemodynamics *in vivo* in a zebrafish model, Chapter 6 demonstrates the first *in vivo* mouse brain imaging with TAM. Beyond label-free visualization of brain vasculature, the development of TAM oximetry will present an invaluable label-free method of measuring blood oxygenation in the brain. Importantly, 2PEF faces from a so-called 'color barrier' which refers to the technical challenges of simultaneously exciting and detecting multiple fluorescence contrasts.[6] Thus, by employing a label-free technique for hemodynamics or oximetry, fluorescence contrasts can be used to target other features such as calcium dynamics in neuronal activity (e.g., GECI model mice). SRS was employed to quantify axon myelination and cell population density. The two predominant methods of quantifying myelination are spectral confocal reflectance (SCoRe) microscopy[7–9] and fluoromyelin staining (2PEF). The former is based on linear elastic scattering from multiple excitation wavelengths and the later is a topically applied lipid stain that makes use of the high

lipid content in myelin. Of the two techniques, fluoromyelin staining is the more commonly used method for visualizing myelination. CRS has been shown as a label-free method to imaging lipids in cells and tissue.[10–12] Moreover, researchers have leveraged this capability to study *in vivo* myelination in the sciatic nerve using CARS microscopy.[13–15] These studies demonstrated the label-free quantitative capabilities of studying demyelination and remyelination in various pathologies and injury models. The results in Chapter 6 illustrate the capability of SRS for *in vivo* quantification of myelination. However, application of SRS microscopy to quantify myelination in the brain has not yet been published.

In addition to myelination, Chapter 6 discusses the employment of SRS image cell populations *in vivo* in the top two cortical layers of mouse brain. Again, fluorescence labeling of multiple cell populations in the brain is possible, but such methods quickly reach a maximum number of detectable and separable fluorescence contrasts. Here, SRS provides label-free characterization of tissue architecture, similar to the approach used in label-free pathology. More specifically, SRS provides chemical mapping of lipid-rich and protein-rich features. This results in a protein-rich images that predominantly illustrates cell nuclei. In order to identify specific cell types, SRS was compared to two fluorescent dyes: NeuroTrace (pericytes) and sulforhodamine 101 (SR101; astroctyes). The morphology of a cell type's nuclei was then used to distinguish between each cell type from the remaining cells (e.g., morphology of astrocyte nuclei compared against morphologies of pericyte nuclei and unstained nuclei).

Machine learning offers a potential route to identify cells more accurately from SRS imaging. Here, a CNN could be trained to detect subtle morphological or spectral differences between cell types. This would require comparison of fluorescently identified cell types with SRS imaging for the predominant cell types in the brain. Ideally, this process would only require a

single two-channel image to provide sufficient information for the CNN to accurately identify cells. However, if two spectral points is insufficient, spectral scans can be performed to establish a richer spectral component of the CNN algorithm.

In closing, nonlinear analytical spectroscopy and microscopy offer powerful capabilities to both fundamental and clinic biomedical research. Demonstrations of these capabilities are numerous, and the future to come is sure to be filled with countless more.

7.1 REFERENCES

(1) Brustlein, S.; Ferrand, P.; Walther, N.; Brasselet, S.; Rigneault, H.; Billaudeau, C.; Marguet, D. D. Optical Parametric Oscillator-Based Light Source for Coherent Raman Scattering Microscopy: Practical Overview. *JBO* **2011**, *16* (2), 021106. https://doi.org/10.1117/1.3533311.
(2) Orringer, D. A.; Pandian, B.; Niknafs, Y. S.; Hollon, T. C.; Boyle, J.; Lewis, S.; Garrard, M.; Hervey-Jumper, S. L.; Garton, H. J. L.; Maher, C. O.; Heth, J. A.; Sagher, O.; Wilkinson, D. A.; Snuderl, M.; Venneti, S.; Ramkissoon, S. H.; McFadden, K. A.; Fisher-Hubbard, A.; Lieberman, A. P.; Johnson, T. D.; Xie, X. S.; Trautman, J. K.; Freudiger, C. W.; Camelo-Piragua, S. Rapid Intraoperative Histology of Unprocessed Surgical Specimens via Fibre-Laser-Based Stimulated Raman Scattering Microscopy. *Nature Biomedical Engineering* **2017**, *1* (2), 1–13. https://doi.org/10.1038/s41551-016-0027.
(3) Liao, C.-S.; Wang, P.; Huang, C. Y.; Lin, P.; Eakins, G.; Bentley, R. T.; Liang, R.; Cheng, J.-X. In Vivo and in Situ Spectroscopic Imaging by a Handheld Stimulated Raman Scattering Microscope. *ACS Photonics* **2018**, *5* (3), 947–954. https://doi.org/10.1021/acsphotonics.7b01214.
(4) Zhang, L.; Wu, Y.; Zheng, B.; Su, L.; Chen, Y.; Ma, S.; Hu, Q.; Zou, X.; Yao, L.; Yang, Y.; Chen, L.; Mao, Y.; Chen, Y.; Ji, M. Rapid Histology of Laryngeal Squamous Cell Carcinoma with Deep-Learning Based Stimulated Raman Scattering Microscopy. *Theranostics* **2019**, *9* (9), 2541–2554. https://doi.org/10.7150/thno.32655.
(5) Hollon, T. C.; Pandian, B.; Adapa, A. R.; Urias, E.; Save, A. V.; Khalsa, S. S. S.; Eichberg, D. G.; D'Amico, R. S.; Farooq, Z. U.; Lewis, S.; Petridis, P. D.; Marie, T.; Shah, A. H.; Garton, H. J. L.; Maher, C. O.; Heth, J. A.; McKean, E. L.; Sullivan, S. E.; Hervey-Jumper, S. L.; Patil, P. G.; Thompson, B. G.; Sagher, O.; McKhann, G. M.; Komotar, R. J.; Ivan, M. E.; Snuderl, M.; Otten, M. L.; Johnson, T. D.; Sisti, M. B.; Bruce, J. N.; Muraszko, K. M.; Trautman, J.; Freudiger, C. W.; Canoll, P.; Lee, H.; Camelo-Piragua, S.; Orringer, D. A. Near Real-Time Intraoperative Brain Tumor Diagnosis Using Stimulated Raman Histology and Deep Neural Networks. *Nature Medicine* **2020**, *26* (1), 52–58. https://doi.org/10.1038/s41591-019-0715-9.
(6) Wei, L.; Chen, Z.; Shi, L.; Long, R.; Anzalone, A. V.; Zhang, L.; Hu, F.; Yuste, R.; Cornish, V. W.; Min, W. Super-Multiplex Vibrational Imaging. *Nature* **2017**, *544* (7651), 465–470. https://doi.org/10.1038/nature22051.

(7) Schain, A. J.; Hill, R. A.; Grutzendler, J. Label-Free in Vivo Imaging of Myelinated Axons in Health and Disease with Spectral Confocal Reflectance Microscopy. *Nat Med* **2014**, *20* (4), 443–449. https://doi.org/10.1038/nm.3495.
(8) Hill, R. A.; Li, A. M.; Grutzendler, J. Lifelong Cortical Myelin Plasticity and Age-Related Degeneration in the Live Mammalian Brain. *Nature Neuroscience* **2018**, *21* (5), 683–695. https://doi.org/10.1038/s41593-018-0120-6.
(9) Gonsalvez, D. G.; Yoo, S.; Fletcher, J. L.; Wood, R. J.; Craig, G. A.; Murray, S. S.; Xiao, J. Imaging and Quantification of Myelin Integrity After Injury With Spectral Confocal Reflectance Microscopy. *Front. Mol. Neurosci.* **2019**, *12*. https://doi.org/10.3389/fnmol.2019.00275.
(10) Yu, Y.; Ramachandran, P. V.; Wang, M. C. Shedding New Light on Lipid Functions with CARS and SRS Microscopy. *Biochim Biophys Acta* **2014**, *1841* (8), 1120–1129. https://doi.org/10.1016/j.bbalip.2014.02.003.
(11) Ferrara, M. A.; Filograna, A.; Ranjan, R.; Corda, D.; Valente, C.; Sirleto, L. Three-Dimensional Label-Free Imaging throughout Adipocyte Differentiation by Stimulated Raman Microscopy. *PLoS One* **2019**, *14* (5). https://doi.org/10.1371/journal.pone.0216811.
(12) Li, X.; Li, Y.; Jiang, M.; Wu, W.; He, S.; Chen, C.; Qin, Z.; Tang, B. Z.; Mak, H. Y.; Qu, J. Y. Quantitative Imaging of Lipid Synthesis and Lipolysis Dynamics in Caenorhabditis Elegans by Stimulated Raman Scattering Microscopy. *Anal. Chem.* **2019**, *91* (3), 2279–2287. https://doi.org/10.1021/acs.analchem.8b04875.
(13) Fu, Y.; Wang, H.; Huff, T. B.; Shi, R.; Cheng, J.-X. Coherent Anti-Stokes Raman Scattering Imaging of Myelin Degradation Reveals a Calcium-Dependent Pathway in Lyso-PtdCho-Induced Demyelination. *J Neurosci Res* **2007**, *85* (13), 2870–2881. https://doi.org/10.1002/jnr.21403.
(14) Fu, Y.; Huff, T. B.; Wang, H.-W.; Wang, H.; Cheng, J.-X. Ex Vivo and in Vivo Imaging of Myelin Fibers in Mouse Brain by Coherent Anti-Stokes Raman Scattering Microscopy. *Opt Express* **2008**, *16* (24), 19396–19409.
(15) Bélanger, E.; Henry, F.; Vallée, R.; Randolph, M.; Kochevar, I.; Winograd, J.; Lin, C.; Côté, D. In Vivo Evaluation of Demyelination and Remyelination in a Nerve Crush Injury Model. *Biomedical Optics Express* **2011**, *2*, 2698–2708. https://doi.org/10.1364/BOE.2.002698.

Andrew T. Francis

EDUCATION

University of Washington, Seattle, WA 2015 – Current
Ph.D. in Chemistry Expected Winter 2020
- "Developing Multiphoton Microscopy Techniques to Study Dynamic Biomedical Systems".
- Research Advisor: Assistant Professor Dan Fu.

M.S. in Chemistry 2016

Hamline University, St. Paul, MN 2011 – 2015
B.S. in Chemistry

RESEARCH EXPERIENCE

University of Washington, Seattle, WA
Doctoral Research 2015 – Current
- Improved label-free pathology of mouse tissues and human brain tumors via novel laser design and image processing.
- Developed quantitative imaging methods of oxygen saturation, hemoglobin concentration, and cell volume of single red blood cells.
- Coupled multiphoton imaging techniques to simultaneously image brain cells and hemodynamics in vivo.
- Quantified average particle size and dissolution rate of an active pharmaceutical ingredient to improve pharmacokinetic modeling.

Hamline University, St. Paul, MN
Undergraduate Research 2012 – 2015
- Isolated, reduced, and characterized graphene sheets for use in thin-film applications.
- Constructed and validated research grade spectrophotometer from inexpensive optics.
- Produced and characterized superhydrophobic surfaces on silicon and glass substrates.
- Quantified sulfite concentration in red wine, white wine, and sangria.

TEACHING EXPERIENCE

University of Washington, Seattle, WA
Teaching Assistant 2015 – 2017
- Courses: General Chemistry 1, General Chemistry 2, Quantitative Analysis.
- Average instructor evaluation: 4.5/5.

Hamline University, St. Paul, MN
Teaching Assistant 2014
- Course: Advanced Laboratory Techniques.
- Maintained and troubleshot GC and MS instruments.

AWARDS AND HONORS

University of Washington, Seattle, WA
Alma Mater Travel Award. 2019
Christopher and Karen Pohl Endowed Find in Chemistry. 2018
Mary K. Simeon and Goldie Simeon Read Chemistry Research Endowment. 2016

Hamline University, St. Paul, MN
Summa Cum Laude. 2015
Phi Beta Kappa. 2015
Omicron Delta Kappa. 2014
Carter Scholarship. 2014
Mitsch Chemistry Scholarship. 2013
Presidential Scholarship. 2011

PEER-REVIEWED PUBLICATIONS

1. Figueroa, B.; Chen, Y.; Berry, K.; **Francis, A.**; Fu, D. Label-Free Chemical Imaging of Latent Fingerprints with Stimulated Raman Scattering Microscopy. *Anal. Chem.* **2017**, *89* (8), 4468-4473.
2. **Francis, A.**; Berry, K.; Chen, Y.; Figueroa, B.; Fu, D. Label-Free Pathology by Spectrally Sliced Femtosecond Stimulated Raman Scattering (SRS) Microscopy. *PLoS One* **2017**, *12*, No. e0178750.
3. **Francis, A.T.**; Nguyen, T.T.; Lamm, M.S.; Teller, R.; Forster, S.P.; Xu, W.; Rhodes, T.; Smith, R.L.; Kuiper, J.; Su, Y.; et al. In Situ Stimulated Raman Scattering (SRS) Microscopy Study of the Dissolution of Sustained-Release Implant Formulation. *Mol. Pharm.* **2018**, *15*, 5793–5801.
4. **Francis, A.T.**; Berry, K.; Thomas, E.C.; Hill, A.H.; Fu, D. In Vitro Quantification of Single Red Blood Cell Oxygen Saturation by Femtosecond Transient Absorption Microscopy. *J. Phys. Chem. Lett.* **2019**, *10* (12), 3312– 3317.
5. Hill, A.H.; Munger, E.; **Francis, A.T.**; Manifold, B.; Fu, D. Frequency Modulation Stimulated Raman Scattering Microscopy through Polarization Encoding. *J. Phys. Chem. B* **2019**, *123* (40), 8397-8404
6. Manifold, B.; Thomas, E.; **Francis, A.T.**; Hill, A.H.; Fu, D. Denoising of Stimulated Raman Scattering Microscopy Images via Deep Learning. *Biomed. Opt. Express* **2019**, *10*, 3860-3874.
7. Shin, K.S.; **Francis, A.T.**; Hill, A.H.; Laohajaratsang, M.; Cimino, P.J.; Latimer, C.S.; Gonzalez-Cuyar, L.F.; Sekhar, L.N.; Juric-Sekhar, G.; Fu, D. Intraoperative Assessment of Skull Base Tumors Using Stimulated Raman Scattering Microscopy. *Sci. Rep*. **2019**, *9*, 20392.
8. **Francis, A.T.**; Shears, M.J.; Murphy, S.C.; Fu, D. Direct Quantification of Single Red Blood Cell Hemoglobin Concentration with Multiphoton Microscopy. *Anal. Chem.* **2020**, *In Press.*
9. **Francis, A.T.**; et al. High-Resolution Imaging of Cortical Structure Changes with Multimodal Multiphoton Microscopy. *In Preparation*.

PROFESSIONAL EXPERIENCE

Medtronic, Inc., Fridley, MN 2013 – 2015

Laboratory Assistant with Surface Analysis and Microscopy Team

- Prepared and analyzed delicate biomedical samples.
- Wrote analytical reports detailing results of surface analysis.

LEADERSHIP EXPERIENCE

University of Washington, Seattle, WA

Laboratory Safety Officer 2015 – Current

- Established and implemented safety SOPs.
- Conducted laboratory safety audits.

Optical Society of America (OSA) Student Chapter Vice President 2019 – Current

- Developed lesson plans for community outreach programs.

Chemistry Graduate Student Club Vice President 2018 – 2019

- Managed meetings and planned departmental events.

Graduate and Professional Student Senate (GPSS) Senator 2015 – 2016

- Advocated for chemistry graduate students at all levels of university decision-making.

TECHNICAL SKILLS

Software: ImageJ, LabView, Matlab, Mathematica, MS Office.

Techniques: AFM, EDS, FTIR, SEM, TOF-SIMS, XPS, white light interferometry, spontaneous Raman scattering spectroscopy, stimulated Raman scattering microscopy, multiphoton fluorescence microscopy, transient absorption microscopy, second harmonic generation microscopy, UV-Vis spectroscopy.

Skills: Laser pulse shaping, microscope design/construction, cranial window surgery (mouse, in vivo), retro-orbital injection (mouse, in vivo), cardiac puncture (mouse, ex vivo), and dissection (mouse).

CONFERENCE PRESENTATIONS

Photonics West, San Francisco, CA 2020

- "In Vivo Quantification of Mean Corpuscular Hemoglobin Concentration by Transient Absorption Microscopy and Stimulated Raman Scattering Microscopy" (oral presentation).

- "In Vitro Quantification of Single Red Blood Cell Oxygen Saturation by Femtosecond Transient Absorption Microscopy" (oral presentation).

Photonics West, San Francisco, CA 2019

- "Quantitative Multimodal Imaging of Neurovascular Coupling" (poster presentation).

Pittcon, Orlando, FL 2018

- "Label-Free Pathology by Stimulated Raman Scattering Microscopy" (oral and poster presentation).
- "Quantitative Imaging of Neurovascular Coupling by Simultaneous Two-Photon Absorption of Blood Oxygenation and Two-Photon Excited Fluorescence of Calcium Dynamics" (poster presentation).

Winchell Undergraduate Research Symposium, Winona, MN 2014

- "Coupling LEGO® Building Blocks and a Cell Phone Camera to Construct a Reliable Spectrophotometer" (oral and poster presentation).

SEMINAR PRESENTATIONS

Hamline University, Department of Chemistry, St. Paul, MN 2019

- "Inventing New Optical Microscopy Techniques to Study Dynamic Biomedical Systems In Vivo and In Vitro" (invited).

OUTREACH

University of Washington, Seattle, WA

Discovery Days Instructor 2019

- Led interactive demonstrations about light and optics.

St Catherine Catholic School, Seattle, WA

Volunteer Instructor (7^{th}-8^{th} grade science class) 2018

- Developed lesson plans and conducted experiments with students.

St Paul Catholic School, Seattle, WA

Volunteer Instructor (5^{th}-8^{th} grade science class)/Science Fair Judge 2017

- Guided students through the scientific process.